DISSERTATION

DYNAMIC MODEL FOR SPACE-TIME WEATHER RADAR OBSERVATION AND NOWCASTING

Submitted by

Gang Xu

Department of Electrical and Computer Engineering

In partial fulfillment of the requirements

For the Degree of Doctor of Philosophy

Colorado State University

Fort Collins, Colorado

Spring 2007

COLORADO STATE UNIVERSITY

February 05, 2007

WE HEREBY RECOMMEND THAT THE **DISSERTATION** PREPARED UNDER OUR SUPERVISION BY **GANG XU** ENTITLED **DYNAMIC MODEL FOR SPACE-TIME WEATHER RADAR OBSERVATION AND NOWCASTING** BE ACCEPTED AS FULFILLING IN PART REQUIREMENTS FOR THE DEGREE OF DOCTOR OF PHILOSOPHY.

Committee on Graduate Work

V.N. Bringi

Anura P. Jayasumana

Paul W. Mielke, Jr.
(Statistics)

V. Chandrasekar
Advisor

Department Head/Director

ABSTRACT OF DISSERTATION

DYNAMIC MODEL FOR SPACE-TIME WEATHER RADAR OBSERVATION AND NOWCASTING

A general framework of the dynamic model for space-time radar observations has been developed in the current research. There exist three difficulties in modeling space-time radar observations: 1) high dimensionality due to the high-resolution radar measurements over a large area, 2) non-stationarity due to the storm motion, and 3) non-stationarity due to evolution (growth and decay). These difficulties are addressed in this research. To deal with the storm motion, an efficient radar storm tracking algorithm is developed in the spectral domain. Based on this new technique, the Dynamic and Adaptive Radar Tracking of Storms (DARTS) is developed and evaluated using the synthesized and the observed radar reflectivity. To tackle the high dimensionality and model the spatial variability of radar observations, a general modeling framework is formulated and the singular value decomposition (SVD) is used for dimension reduction. To deal with the dynamic evolution and model the temporal variability of radar observations, the motion-compensated temporal alignment (MCTA) transformation is developed. In this analysis the evolution of radar storm fields is modeled by the linear dynamic system (LDS) in the low-dimensional subspace. The applications of the dynamic model for space-time radar observations are further demonstrated. Spatial and dynamic characteristics are obtained based on the estimated model parameters using three months of radar observations. The characteristic temporal scales are quantified for this

dataset. The correlation between the temporal characterization and the spatial characterization of observed radar fields are explored. The simulation capability of different spatiotemporal radar reflectivity fields is demonstrated. Evaluation of the space time variability is particularly important in the context of adaptive scanning of storm systems. The short-term prediction of radar reflectivity fields based on the space-time dynamic model is evaluated using observed radar data. The simulations of the DARTS for real-time applications are also conducted and evaluated.

Gang Xu
Department of Electrical and Computer Engineering
Colorado State University
Fort Collins, CO 80523
Spring, 2007

ACKNOWLEDGMENTS

I would like to express my sincere acknowledgement to my colleagues, Gwo-Jong Huang, Sanghun Lim, Yanting Wang and Yuxiang Liu, who have offered the cordial help to my work. Acknowledgement goes to Mr. Dilbert Willie, who helped me in accessing the KOUN dataset of year 2003.

My appreciation goes to my advisor, Prof. V. Chandrasekar for his support to my work. The discussions I had with him greatly helped me in completing my dissertation.

The support of committee members Prof. V. N. Bringi, Prof. Anura P. Jayasumana and Prof. Paul W. Mielke, Jr., is sincerely appreciated. Prof. Paul W. Mielke, Jr., is thanked for providing the excellent advice and programs on the permutation test (MRBP procedures).

Last but not least, my earnest appreciation goes to my friend Larry Detweiler, who offered constructive discussions and personal communications during my research.

This research is supported by the NSF ITR program (ATM-0121546) and CASA ERC program (ERC-0313747).

TABLE OF CONTENTS

LIST OF FIGURES

LIST OF TABLES

CHAPTER I. INTRODUCTION

1.1. Background Review

The prediction of thunderstorms has been an active and flourishing modern discipline, especially due to the advancement of the understanding of the dynamics and microphysics of storms as well as the advent of various new observation technologies including the scanning Doppler weather radar. The maximum range of weather radar is usually of the order of several hundred km, while the minimum resolved scale can be of the order of 100 to 200 m. The radar observations can be updated in a few minutes. Therefore the modern weather radar provides high-resolution measurements in both space and time, and covers the area of tens of thousands of square kilometers. Weather radar has become one of the primary tools for monitoring and forecasting the severe storms that may extend tens to hundreds of kilometers, yet whose scale is still relatively small compared to the synoptic scale of the earth. Many high-impact and severe weather phenomena are the meso-scale or the storm-scale systems, having the lifetime from a few tens of minutes to a few hours. So the very short term forecasting of thunderstorms is particularly important to various end users, such as the airport transportation, the highway traffic, the construction industry, the outdoor sporting and entertainment, the public safety management, resource (e.g., agriculture and forest) protection and management. The forecast of such type is termed as the nowcasting, which can be defined as the

forecasting thunderstorms for a very short time periods less than a few hours, i.e., 0 – 6 h (Wilson 2004).

Comprehensive survey of the research of nowcasting thunderstorms, using radar as the primary observational tool, can be found in Wilson et al (1998) and Wilson (2004). During the first several decades (1950's – early 1990's), the short-term prediction of thunderstorms mainly relied on tracking and extrapolating radar echoes. Until the current date, two types of robust tracking techniques have been developed: 1) the distributed "motion-field" based storm tracker (Rinehart and Garvey 1978), and 2) the "centroid" storm cell tracker (Dixon and Wiener 1993). Since the 1990's the prediction of storm's initiation, growth and dissipation beyond the extrapolation has become an active research area, while the forecasting skills of the simple extrapolation decay rapidly during the first 60 min. Several important studies in this area should be mentioned. Tsonis and Austin (1981) studied the prediction of echo intensity and sizes based on their history trends, and found that little improvement was gained by adding the heuristic trends over the simple extrapolation. In these studies they tested several forms of total flux over the area of the cell, including the exponential, the power law, the linear and the second-degree polynomial. Recently MacKeen et al (1999) studied the correlation between radar reflectivity-derived parameters and storm longevity, and found that little useful correlation of such types exists. Building upon some physically and empirically based evidences, Wilson and Mueller (1993) developed the conceptual model for nowcasting thunderstorm's initiation and evolution. In their model the nowcast is primarily based on the identification of boundary-layer convergence lines, radar reflectivity, Doppler velocity structure and visual satellite images.

Several studies have revealed that the characteristics of space-time radar echoes are dependent on the scale of weather systems. Wilson (1966) and Wilson et al (1998) showed that the maximum cross-correlation of echo patterns increases with the scale size, and the echoes of different scales can have significantly different motions. Wolfson et al (1999) also revealed the similar results and employed these results to develop an improved tracking algorithm by removing smaller scale features via the oblong filter. Germann and Zawadzki (2002) studied the integrated cross-correlation coefficient as a function of the scale of continental radar images, and found that the integrated cross-correlation coefficient monotonically increases with the scale. Germann and Zawadzki (2002) performed the scale decomposition by means of the discrete-cosine-transform (DCT) and the low-pass filter. Bellon and Zawadzki (1994) applied the spatial smoothing approach to determine the optimal extrapolation of radar images. Recently Seed (2003) developed a spatial scaling scheme to advection forecasting, where the scale decomposition is conducted by the discrete-Fourier-transform (DFT) and a band-pass filter. The temporal evolution is subsequently modeled in Lagrangian space by auto-regressive (AR) processes of order two.

Kitzmiller (1996) has developed the extrapolative-statistical models for accumulative precipitation nowcast by combining the radar data and the numerical-model generated data. Sokol et al (2004) further studied different regression models for extrapolative-statistical nowcast.

The most recent advances in thunderstorm nowcasting are discussed by Wilson (2004). These advances include radar refractivity measurements for space-time water vapor retrieval (Fabry et al 1997), numerical boundary layer models and prediction, and

explicit storm-scale numerical models initialized and updated using the high-resolution Doppler radar data. Most of these advances involve a great amount of effort to extend the predicting capability of explicit numerical models for convective storm scale systems. However, nowcast validation of numerical models and the comparison with the extrapolation is still incomplete, and it is felt most likely that numerical techniques will not be able to predict storm's characteristics and evolution with sufficient accuracy in the near future (Wilson 2004). As discussed by Wilson (2004), the current progress in forecasting thunderstorms implies that the best approach should be the combination of extrapolation, statistical prediction, numerical weather modeling, conceptual models and heuristic forecast rules of thumb. Based on the same philosophy, the Auto-Nowcast System (Mueller et al 2003) developed at the National Center for Atmospheric Research (NCAR) is such a data fusion system that utilizes the fuzzy logic to combine various predictor fields and produce 0 – 1 h convective storm forecast. Keenan et al (2003) presented an overview and comparison of nine existing nowcasting systems deployed in the forecast demonstration project during the 2000 Olympic Games in Sydney, Australia. In general all existing systems have the limited ability to forecast storm's evolution and the extrapolation technique remains to be the primary tool.

Stroud et al (2001) proposed a statistical dynamic model for non-stationary spatiotemporal observations. The model is cast in a linear state-space framework where the spatial modeling corresponds to an observation equation and the temporal modeling corresponds to a state equation. The theories for filtering, predicting and smoothing in linear dynamic systems were well developed the decades ago (Kalman 1960; Rauch 1963). A recent treatment of these topics under the general Bayesian framework can be

found in West and Harrison (1997). Although the statistical techniques have been somewhat employed to radar storm modeling and nowcasting (Kitzmiller 1996; Sokol et al 2004), yet the dynamic modeling for space-time radar observations is still largely unexplored. An exception is the statistical and spatiotemporal modeling for radar storm nowcast by Batail (2002), in which the observational process is cast by the spatial modeling using the Radial-Basis-Function (RBF) neural network, and the state space variables consist of the RBF-neural-network's centers, widths, weights and the storm's motion vectors. In Batail's work (2002), the full implementation of the probabilistic model incorporates only two components: 1) the storm advection, and 2) the Gaussian stochastic error. The forecasting is computed via the stochastic simulation and the ensemble average.

1.2. Objectives of the Research

a. *Problem statement*

Weather radar observations can be obtained sequentially in time, therefore the storm evolution can be mapped into the time series of radar images. Since the mapping from radar measurements to precipitation amounts by itself is a difficult problem (Bringi and Chandrasekar 2001; Chandrasekar and Bringi 2004), the scope of the current research is limited to predicting subsequent short-term reflectivity images using a short history of the space-time radar observation, e.g., the radar reflectivity. Furthermore the temporal sequence of radar observations can also be used to characterize the complex spatiotemporal variability in different weather systems. There exist two types of major difficulties in above problems, namely:

1) *High Dimensionality*: Each radar image may extend a large area with high resolution and it has a high number of pixels. For example, a relatively small radar image extending an area of 100 km × 100 km with 1 km resolution consists of ~10^4 pixels. It is difficult to represent such a dataset in the model.

2) *Non-stationarity*: The storm process is generally a dynamic and time-varying process. This is mainly due to two mechanisms: firstly, storm systems are constantly moving in the spatial domain, and secondly, the storm's evolution (growth and dissipation) is non-stationary. The identification and the model of storm motion for predicting its near-future location and intensity is called storm tracking and nowcasting.

The objectives of the research consist of: 1) the development of efficient algorithms for storm tracking and extrapolation based on the motion model modified for space-time radar observations; 2) the development of statistical dynamic models for spatiotemporal radar observations and the development of fundamental analysis techniques in order to support adaptive observations such as the CASA systems; and 3) the application of above algorithms and statistical dynamic models to the short-term storm forecasting, setting up adaptive scanning and the characterization of different storm systems.

b. *A new system for radar storm motion tracking and nowcasting*

Storm tracking using a temporal sequence of radar observations is an important step in computer-aided operational nowcasting. This primarily addresses the first non-stationary mechanism, namely, the storm motion in the spatial domain. The traditional approach is to identify non-uniform motions by maximizing the cross-correlation over two local blocks in successive radar images. Limitations and issues have been identified

for the cross-correlation based tracker. Various improved methods have been developed based on the local pattern match. In this research a novel and efficient algorithm for estimating the storm motion from the space-time radar measurements have been developed and evaluated. The algorithm is based on the modified flow-field equation that is solved in the spectral domain. The new algorithm is validated using the synthesized sequences of radar reflectivity images. A simple, yet efficient, numerical algorithm for extrapolating the radar reflectivity field is also tested and validated. The new system for radar storm tracking and extrapolating is then applied to the one-hour nowcast, using two sets of observational reflectivity: one is from the WSR-88D radar at Melbourne, FL and the other one is from the KOUN radar at Norman, OK. The new system is evaluated and validated by comparing its forecasting scores with the "Growth-Decay Storm Tracker" (GDST) based algorithm developed at the MIT Lincoln Laboratory (Wolfson et al 1999). The new system is further evaluated and validated using the reflectivity images collected and merged from the four-radar CASA network (Oklahoma) in the Collaborative Adaptive Sensing of Atmosphere (CASA) IP1 project. The data from the CASA IP1 project has higher spatial and temporal resolutions. The radar images sequence has the temporal interval of thirty seconds.

With regard to operational applications, the simulation will be conducted to evaluate the real-time performance of the spectral tracking and nowcasting system. The efficiency of the new algorithms is studied in these simulations. The robustness of the new system in the consideration of various practical issues is also analyzed.

c. *A general framework for modeling space-time radar observations*

A general state-space framework for modeling spatiotemporal radar observation is developed. The spatial modeling with an optimal subspace projection is cast into the observation equation. The temporal modeling for dynamic evolution is cast into the state equation. The optimal subspace is computed by the singular value decomposition (SVD) and this significantly reduces the dimension of the vector space. In this research state evolutionary equations are restricted to the linear dynamical system (LDS). The storm motion can be represented in the subspace by a linear-flow matrix. The theoretical properties of the linear-flow matrix in continuous-time LDS have been presented. They are verified using the observed reflectivity from the WSR-88D radar at Melbourne, FL. The general characteristics of the liner-map matrix in the discrete-time LDS are accordingly discussed. Within the state-space framework, the linear dynamic model that decomposes the storm motion and the storm evolution is further formulated in a generalized form. To do so the Motion Compensated Temporal Alignment (MCTA) transformation has been introduced. The theoretical results for the sequence in the MCTA-transformed space are discussed.

d. *Application of the space-time model for radar observations*

Two types of applications will be studied using the space-time modeling scheme developed above. The first type of applications is to characterize the spatiotemporal variability of radar measurements and storms. The second type of applications is to predict the short-term sequence of radar reflectivity images. To do so we need to first identify the model structure and its parameters. This is the model estimation problem. Once the model is estimated, we can apply it to simulating the stochastic sequence of

radar observational fields. The stochastic simulation of space-time radar observational fields belongs to the first type of applications.

The spatiotemporal variability will be characterized by the feature vector consisting of the parameters that are estimated in the space-time dynamic model. Specifically, the feature vector consists of the maximal singular value, the ratios of the maximum singular value to all singular values, and the inverts of the eigen-frequencies of linear flow matrix in the MCTA subspace. The spatial variability is characterized by the maximal singular value and its ratios to all singular values, while the temporal or dynamic variability is characterized by the eigen-frequencies of the flow matrix. The spatiotemporal analysis is applied to three months of data collected by the KOUN radar located at Norman, OK (2003). The classification and stochastic simulations are conducted based on the estimated model parameters. The characteristic time scales are quantified for the KOUN radar observations over April, May and June in 2003. The radar reflectivity fields of different spatiotemporal characteristics are simulated. The space-time modeling based on the differential reflectivity (ZDR in dB) is also studied.

For the application of the space-time model to short-term prediction, the storm motion can be modeled in the subspace by a linear-flow matrix. The linear-map matrix including both storm motion and evolution is identified in the Least-Square Vector-Auto-Regressive (LS-VAR) model. The extrapolative LS-VAR model is tested and validated using the observed reflectivity from the WSR-88D radar at Melbourne, FL. A metric distance based interpretation is presented and the distance-function based permutation test is applied to evaluating predicting skills. Results are compared with the spectral tracking algorithm developed above and the GDST based algorithm. It has demonstrated

the significant advantage of the dynamic model based extrapolation over the tracking-only based extrapolation. In the MCTA space the Kalman filter based predictions are also compared with the extrapolative LS-VAR model.

CHAPTER II. A NEW SYSTEM FOR RADAR STORM MOTION TRACKING AND NOWCASTING – A SPECTRAL DOMAIN APPROACH

2.1. Introduction

Storm tracking using a temporal sequence of radar images is an important step in computer-aided operational nowcasting (Browning and Collier 1989; Chornoboy et al, 1994; Wilson et al, 1998). Generally speaking, all existing techniques for storm tracking are based on two fundamental approaches. The first approach is to identify the spatially distributed motion field by maximizing the cross-correlation over two local blocks in two successive radar images (Rinehart and Garvey 1978; Chornoboy et al 1994). The second approach is referred to as the "centroid tracking" (Austin and Bellon 1982), which defines the "storm-cell" using certain characteristic parameters and these cell objects are identified and tracked using various heuristic or optimization algorithms. There exist at least three commonly used procedures for radar storm tracking. These procedures have developed various enhanced features based on two fundamental approaches. Wolfson et al (1999) have recently developed a procedure referred as "growth-decay storm tracker". The "growth-decay storm tracker" employs an elliptically shaped spatial filter such as to enable tracking systematic growth-decay propagations of the larger scale component in storms. Johnson et al (1998) developed the storm cell identification and tracking (SCIT) algorithm that blends both fundamental approaches. The third commonly used procedure is based on the identification of storm's position, size, mergers and splits. It is a "cell-tracking" procedure and was implemented in the TITAN algorithm, referring to

thunderstorm identification, tracking, analysis and nowcasting. TITAN was originally developed by Dixon and Wiener (1993).

All above pattern matching techniques are similar to other template matching methods, such as area correlation and matched filtering in image detection (Jain 1989). The motion estimation in visual perception and computer vision has been an active research topic due to its fundamental importance and wide applications (Adelson and Bergen 1985; Beauchemin and Barron 1995). The comprehensive review of various techniques for optical flow computation in two dimensional images was given by Beauchemin and Barron (1995). Among these techniques they discussed the differential methods that borrow the concepts from the fluid transport theory and the regularization theory. Similar techniques were also developed for estimating cloud motions using the sequence of satellite images (Leese et al 1971; Larsen et al 1998). Wahl and Simpson (1990) studied the influence of other physical processes on the motion estimation using the cross-correlation among sea surface temperature (SST) images.

The primary motivation of storm tracking is to identify the motion field that can serve as a good nowcasting indicator. Therefore a tracking algorithm that is able to mitigate the influence of other dynamic mechanisms on the motion estimation may facilitate improving nowcast skills. However, effectively separating different dynamic mechanisms and accurately identifying the storm motion in complex weather systems stand as a technical challenge. Few of existing tracking techniques have explicitly dealt with the issue of separating different dynamic mechanisms in complex storms. For example, recently Li et al (1995) developed a variational based technique that uses the continuity constraints. This tracking technique allows for identifying the regions of the

growth and the decay in radar echoes. Another important issue in storm tracking is the storm scale. It has been known that the larger scale storms tend to be more persistent and predictable than the smaller scale storms (Wilson 1966; Wilson et al 1998; Germann and Zawadzki 2002). It is commonly found in storms that the larger scale component may move toward the different direction from the smaller scale component (Wilson et al 1998; Wolfson et al 1999). This empirical scaling principle has been applied to the "growth-decay storm tracker" that intends to track the systematic propagation of larger-scale storms. Therefore it is important for a tracking algorithm to be able to explicitly control various scales of the storm.

In current research a novel algorithm is developed in the spectral domain for estimating the distributed motion field of the storm. The algorithm is built upon the general flow equation that is modified for storm motion tracking. It is a linear model that is able to separate the storm motion from local and additive growth-decay mechanisms. The novelty of this algorithm is that it is developed in the spectral domain, such that the various scales of both storm and motion field can be controlled by the choice of Fourier coefficients. When compared with the cross-correlation method, the new algorithm also has several other advantageous features. It is a global algorithm in the sense that it does not employ local block windows in radar images. Therefore the estimated motion field can be globally constructed over the whole spatial region where radar images are rendered. The smoothness of the estimated motion field is controlled by selecting fewer leading Fourier coefficients. The motion-flow equation for radar images is formulated and solved in the Fourier space. The model parameters in the Fourier space are estimated by the linear Least-Square-Estimation (LSE) (Stark and Woods 1994). The Fast Fourier

Transform (FFT) and the linear LSE algorithm are easy to implement and the numerical computation is fast.

A simple yet effective numerical algorithm for computing the advection of radar reflectivity is also developed. This algorithm is based on the *Whittaker-Shannon-Kotelnikov* (W.S.K.) sampling theorem and can be applied to the reflectivity field sampled on regular grids. This method can be viewed as the interpolation in the spatial domain using the *SINC*-kernels (Stenger 1993; Kowalski et al 1995), along with the 1^{st}-order discretization on time, so that the matrix-based computation is formulated and the numerical integration over time is conducted through the iteration in small steps. The general spatial model based on the kernel functional technique will be studied in the next chapter.

The flow-equation model and the tracking algorithm in the spectral domain are developed in next section, where a numerical algorithm (*SINC*-approximation) for computing the extrapolation of radar reflectivity is also described and quantitatively assessed. Relevant literatures for the numerical computation of advection are briefly reviewed. The application of the new nowcasting system is studied in section 3. The performance of the spectral tracking algorithm is evaluated using both the synthesized reflectivity and the observed radar reflectivity. The feasibility of realtime application of the new nowcasting system is studied and evaluated in section 4. In section 5 summary and discussion are presented.

2.2. Algorithm for Radar Storm Tracking and Extrapolating: Dynamic and Adaptive Radar Tracking of Storms (DARTS)

a. *The General model*

The flow equation of motion is extensively applied to modeling atmospheric dynamics (Holton 2004; Schertzer and Lovejoy 1987). The general motion-flow equation for the radar observation field *F(x, y, t)* is written in a modified form as

$$\frac{\partial}{\partial t}F(x,y,t) = -U(x,y)\frac{\partial}{\partial x}F(x,y,t) - V(x,y)\frac{\partial}{\partial y}F(x,y,t) + S(x,y,t) \tag{2.1}$$

In Eq 2.1 *F(x, y, t)* is the scalar field of radar observation that is modeled as a spatiotemporal process. *U(x, y)* is the x-axis motion velocity and *V(x, y)* is the y-axis motion velocity over the spatial domain. *S(x, y, t)* is generally interpreted as other dynamic mechanisms, such as the growth-decay term. *S(x, y, t)* will be called as "S-term" hereafter. The model in Eq 2.1 is expressed in the Euler space, in which the radar observational field *F(x, y, t)* can be conveniently represented.

b. *A new algorithm for radar storm motion estimation*

The discrete version of *F(x, y, t)* is written as *F(i, j, k)*. A solution for equation (2.1) is developed in frequency domain by solving the linear system as follows.

$$\vec{\mathbf{y}} = \mathbf{H}\,\vec{\mathbf{x}} \tag{2.2}$$

where vector $\vec{\mathbf{x}}$ consists of unknown Fourier coefficients to be estimated, vector $\vec{\mathbf{y}}$ consists of the Fourier coefficients computed from the observed radar field *F(i, j, k)*, and $\mathbf{H}$ is the matrix connecting $\vec{\mathbf{x}}$ and $\vec{\mathbf{y}}$ in frequency domain. By choosing fewer leading coefficients among unknown Fourier coefficients, Eq 2.2 may form an over-determined linear system that can be solved by the linear LSE method. In Eq 2.2, various scales of

the storm can be controlled by choosing the desired leading coefficients among the Fourier coefficients computed from the observed radar field $F(i, j, k)$, provided that the resulting equation forms an over-determined linear system. This can generally be achieved when the motion field and the S-term have much fewer leading coefficients than the radar field.

Although Eq 2.1 is a conceptually simple model, it offers several advantages when combined with the spectral solution (Eq 2.2). Firstly, the model given by Eq 2.1 has the ability to separate the growth and decay mechanisms from motion terms. This is achieved via the extra term $S(x, y, t)$. As demonstrated in simulations below, this can alleviate the impact of local and independent growth on motion tracking. The implication of this property of the spectral algorithm is that, by explicitly introducing other linear mechanisms in the model, we may be able to better separate the storm motion from other dynamic mechanisms. Secondly, the scales of the storm can be conveniently controlled in the frequency domain solution. As discussed above, it is important for the tracking algorithm to be able to explicitly control the scales of the storm, while the controllability of scales is merely an inherent functionality in this new spectral algorithm. Thirdly, the motion estimation is formulated and solved in the spectral domain so that the estimated motion field is globally constructed over the whole spatial region where radar images are rendered. This way we not only avoid the issue of block window size versus the accuracy of local-point estimation, but also minimize the "aperture-effect" caused by the local block window (Chornoboy et al 1994). In general, motion fields vary slowly over the spatial domain, so we can indeed select fewer leading Fourier coefficients to estimate and construct a smooth motion field. Fourthly, the cross-correlation technique that is

currently widely used is mainly for its stable performance. However, the high computational cost of the cross-correlation method is also well known. This is due to that the vast searching has to be performed to obtain the best and robust matching. To avoid occasionally unsmoothed estimation, the heuristic hierarchical procedure from coarser scales to finer scales usually has to be conducted. The new spectral algorithm applies the linear inversion algorithm to the reduced set of Fourier coefficients. It has the optimal solution in a closed form and the computation of linear LSE is efficient. As demonstrated below, the new algorithm shows good performance for both synthesized reflectivity sequences and observed radar reflectivity sequences.

c. *Numerical computation of the extrapolation of radar reflectivity*

A large number of computational schemes for the atmospheric advection have been proposed in literatures. These advection schemes were originally developed for atmospheric transport and chemistry models and these studies have started since the early 1960's (Rood 1987). Germann and Zawadzki (2002) have applied a modified version of the semi-lagrangian scheme to the advection of radar reflectivity. A comprehensive review of numerical advection algorithms can be found in Rood (1987). In pursuit of the efficient computational scheme, a new algorithm technique has been developed here. The new algorithm is not only easy to implement, but also fairly accurate. In comparison with various other sophisticated schemes, this new scheme is similar to the spectral and pseudo-spectral schemes using functional expansions (Rood 1987). As indicated by Rood (1987), spectral and pseudo-spectral techniques consistently provide the highest degree of accuracy, at the cost of more computational load and difficulties associated with the Gibbs phenomenon.

Two most common problems in numerical schemes for the advection are "numerical diffusion" and "numerical dispersion". Numerical diffusion refers to the loss of peak power resulting from the redistribution or the interpolation, for example, in the semi-Lagrangian scheme (Germann and Zawadzki 2002). Therefore numerical diffusion is sometimes synonymous to dissipation in the numerical advection. Numerical dispersion refers to the phenomena of oscillations resulting from different phase speeds among different Fourier components in numerical schemes. In general numerical diffusion causes a loss of power at small scales and numerical dispersion leads to the erroneous variance of the advection field. To assess the applicability of the proposed advection algorithm in this research, the diffusion and dispersion effects are studied. As will be shown below, the proposed numerical algorithm exhibits nearly no diffusion effect and insignificant dispersion errors, when compared to the analytic result.

In following paragraphs, firstly the essential idea and the formulation of the advection algorithm for radar reflectivity will be described. Then the quantitative assessment as regards the "numerical dispersion" and the "numerical diffusion" will be presented.

We can generally model the reflectivity field as a continuous function over the spatial domain. In following applications the spatial domain is a bounded two-dimensional region. At a fixed time t, discrete observations on regular grids in the bounded region can be viewed as the discrete samples of the continuous reflectivity function. It is assumed that the continuous reflectivity function is in the band-limit functional space Ω_w with bandwidth $w_i = (2\Delta_i)^{-1}$, where $i = x$ or y and Δ_i is the sampling interval on the x or the y axis. According to the *Whittaker-Shannon-Kotelnikov* (W.S.K.) sampling theorem

(Whittaker, 1915; Shannon, 1949; Higgins, 1996), we write the reflectivity field *F(x, y, t)* in approximation as follows:

$$F(x,y,t) = \sum_{k=1}^{N_x}\sum_{l=1}^{N_y} F_{kl}(t) \times SINC(\frac{x}{\Delta_x} - k) \times SINC(\frac{y}{\Delta_y} - l) \tag{2.3}$$

$$F_{kl}(t) \equiv F(k \cdot \Delta_x, l \cdot \Delta_y, t) \tag{2.4}$$

where the equidistance samples of *F(x, y, t)*, namely, $F_{kl}(t)$, may be interpreted as the coefficients of the 2D product basis that are obtained by appropriate translating and rescaling of the *SINC*-kernel function: $SINC(x) = \sin(\pi x)/(\pi x)$. The approximation in Eq 2.3 results from the finiteness of discrete samples. However, for the function well confined within a bounded region, this gives a fairly accurate approximation since the SINC-kernel function is appropriately localized. Therefore the continuous function in Eq 2.3 can be used to analytically calculate the spatial derivatives in Eq 2.1. This leads to following equations (See Appendix B for the details).

$$\frac{\partial}{\partial t} F_{kl}(t) = -\frac{U_{kl}}{\Delta_x} \cdot \left[\mathbf{A}\, \mathbf{F}(t) \right]_{kl} - \frac{V_{kl}}{\Delta_y} \cdot \left[\mathbf{F}(t)\, \mathbf{Z} \right]_{kl} \tag{2.5}$$

$$F_{kl}(t + \delta_t) = F_{kl}(t) - \left\{ \frac{U_{kl}}{\Delta_x} \cdot \left[\mathbf{A}\, \mathbf{F}(t) \right]_{kl} + \frac{V_{kl}}{\Delta_y} \cdot \left[\mathbf{F}(t)\, \mathbf{Z} \right]_{kl} \right\} \cdot \delta_t \tag{2.6}$$

where matrices **A**, **Z** and **F**(t) are defined by

$$\mathbf{A} \equiv [A_{km}] \equiv [DSINC(k-m)] \tag{2.7}$$

$$\mathbf{Z} \equiv [Z_{nl}] \equiv [DSINC(l-n)] \tag{2.8}$$

$$\mathbf{F}(t) \equiv [F_{ml}(t)] \quad \text{or} \quad \mathbf{F}(t) \equiv [F_{kn}(t)] \tag{2.9}$$

DSINC is the derivative of the *SINC*-function (See Appendix B, Eq C.5). Eq 2.6 is obtained by taking the 1st-order discretization of Eq 2.5. The above equations show that

the numerical advection can be conducted by the matrix-based computation, and the temporal integration is done by the iteration of matrix computations at small steps. In this scheme no heuristic and sophisticated redistribution or interpolation procedures are carried out. This scheme can be viewed as the functional approximation in the spatial domain using *SINC*-kernels. In fact, the *SINC*-functional technique in numerical methods has been extensively studied in the theory of approximation and computation, which has led to rich and broad results in both applied mathematics and numerical computations (See, for example, Stenger 1993, and Kowalski et al 1995). Hereafter we refer to the above advection scheme as the *SINC*-approximation.

To assess the applicability of the *SINC*-approximation for the reflectivity extrapolation, we need study its "numerical dispersion" and "numerical diffusion". In this study we use a two-dimensional observational reflectivity map as the initial data. As assumed above, the discrete reflectivity data are samples of a continuous function ($\in \Omega_w$). To assure a simple analytic solution, we use a constant and uniform motion field over the spatial domain, namely, $U(x,y) = V(x,y) = 0.5$ grid step^{-1}. With total steps of *40*, the discrete samples of the final analytic solution to the advection is a reflectivity map obtained by shifting the initial map by 20×20 grids.

To study the numerical dispersion of the *SINC*-approximation, we compare the analytic result (Fig 1) with the reflectivity map computed using the *SINC*-approximation (Fig 2). For the quantitative comparison of reflectivity maps (Fig 1 *v.s.* Fig 2), the equivalent signal-to-noise-ratio (SNR) (Bringi and Chandrasekar 2001) is *25.5* dB and the maximal absolute error is *3.9* dBZ. The histograms of absolute errors between the analytic result and the *SINC*-approximation for reflectivity maps are presented in Fig 3.

The corresponding empirical cumulative distribution functions (CDF) are shown in Fig 4. Although the maximum absolute error of reflectivity can be as large as *3.9* dBZ, yet we see from its CDF curve (Fig 4) that more than 95% of these absolute errors are less than *0.8* dBZ. Therefore we conclude that the numerical dispersion of *SINC*-approximation for the reflectivity advection causes insignificant false variances in radar reflectivity fields. We simply apply a threshold to the computed reflectivity map, so as to filter out the slight false variance, and have empirically determined the best threshold value to be *10* dBZ.

To study the numerical diffusion of the *SINC*-approximation, we compute and compare the average one-dimensional power spectrum for both analytic reflectivity map and *SINC*-approximation reflectivity map. The average one-dimensional power spectrum is computed along either x-axis or y-axis. Averaged one-dimensional power spectra are shown in Fig 5 and Fig 6, from which we see that the comparison shows nearly the perfect match. No diffusion effect is detected almost down to the smallest available scale (*2* km). The *SINC*-approximation for reflectivity advection exhibits undetectable "numerical diffusion", as the proposed advection algorithm does not introduce any heuristic redistribution procedures and the spatial derivatives are approximated by the analytic function.

In following studies the *SINC*-approximation will be applied to computing the reflectivity advection and extrapolating the reflectivity images. As discussed above the threshold value (*10* dBZ) is applied to the computed reflectivity field.

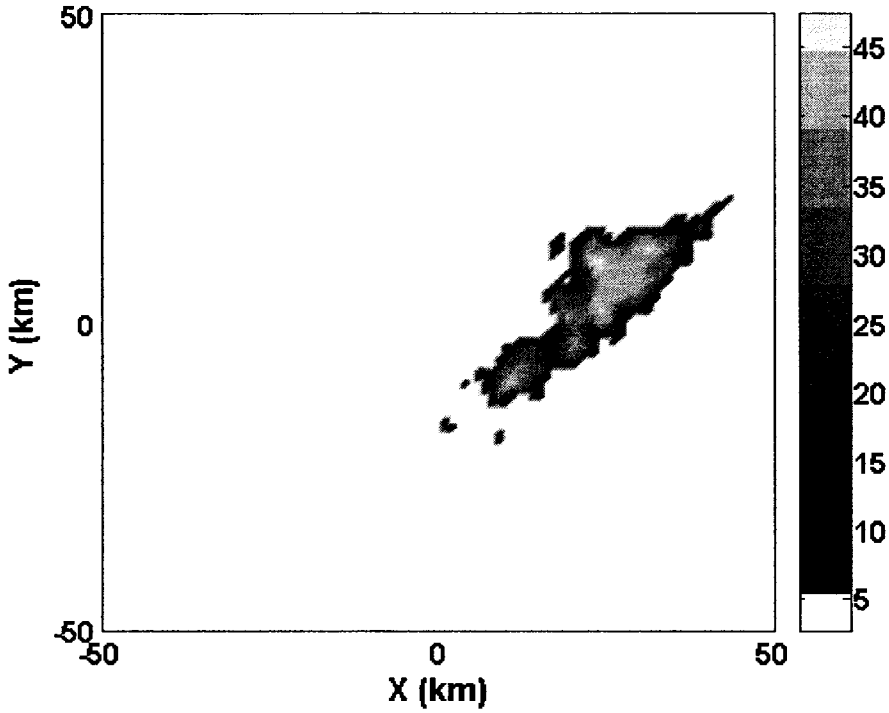

Figure 1. Reflectivity (dBZ) map from the analytic solution.

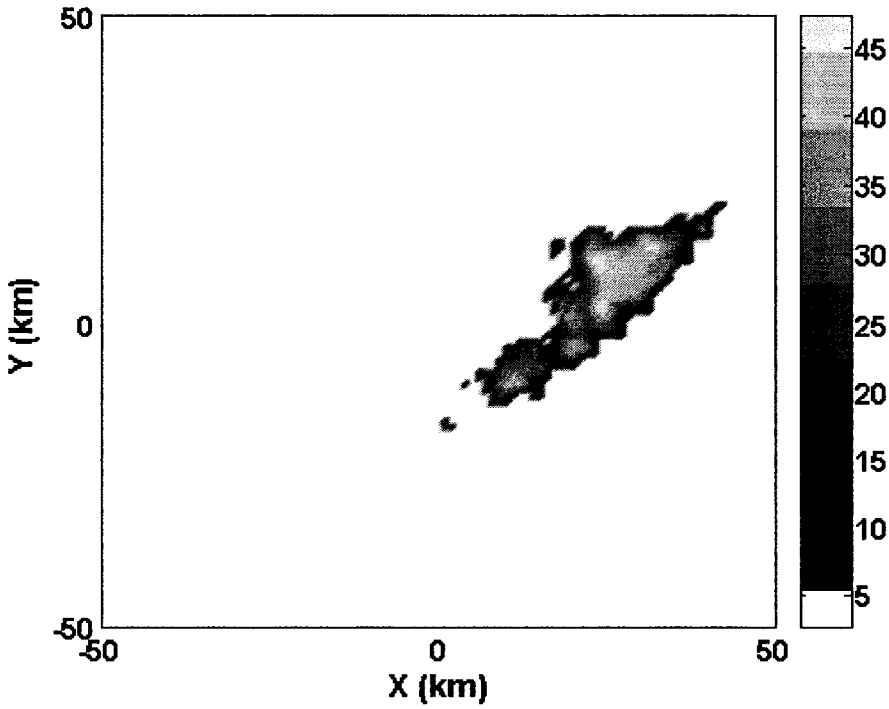

Figure 2. Reflectivity (dBZ) map from the *SINC*-approximation.

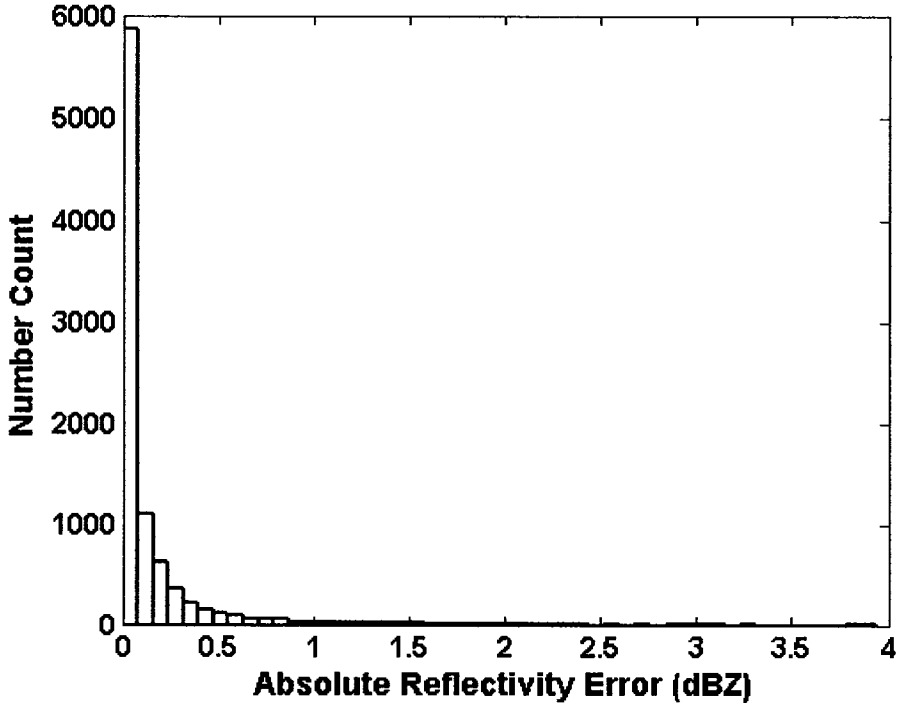

Figure 3. Histogram of absolute error of reflectivity (dBZ) between the analytic solution and the *SINC*-approximation.

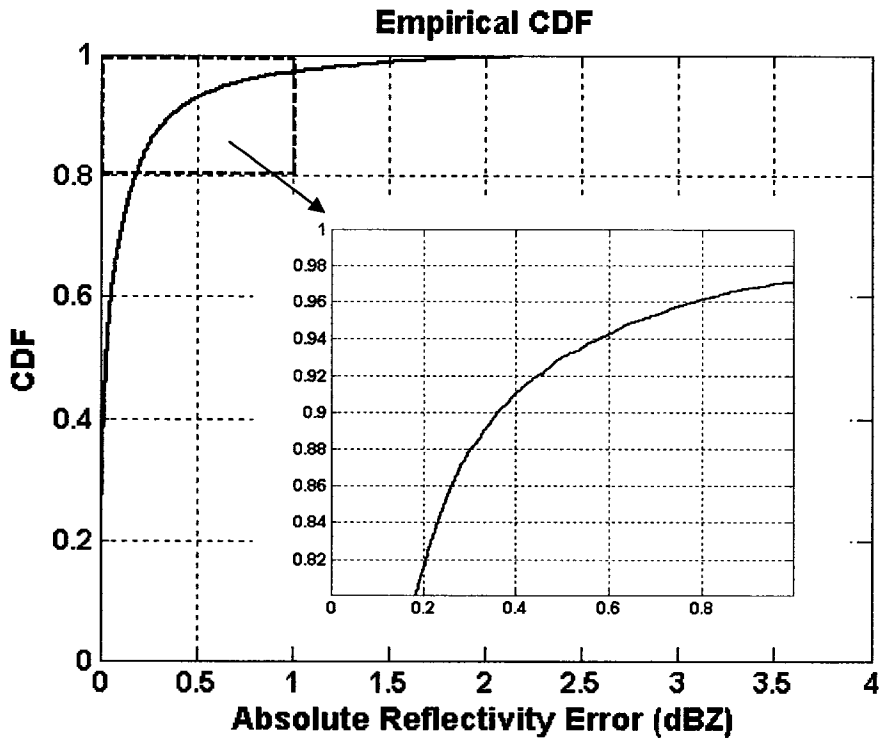

Figure 4. Cumulative distribution function (CDF) of absolute error of reflectivity (dBZ) between the analytic solution and the *SINC*-approximation.

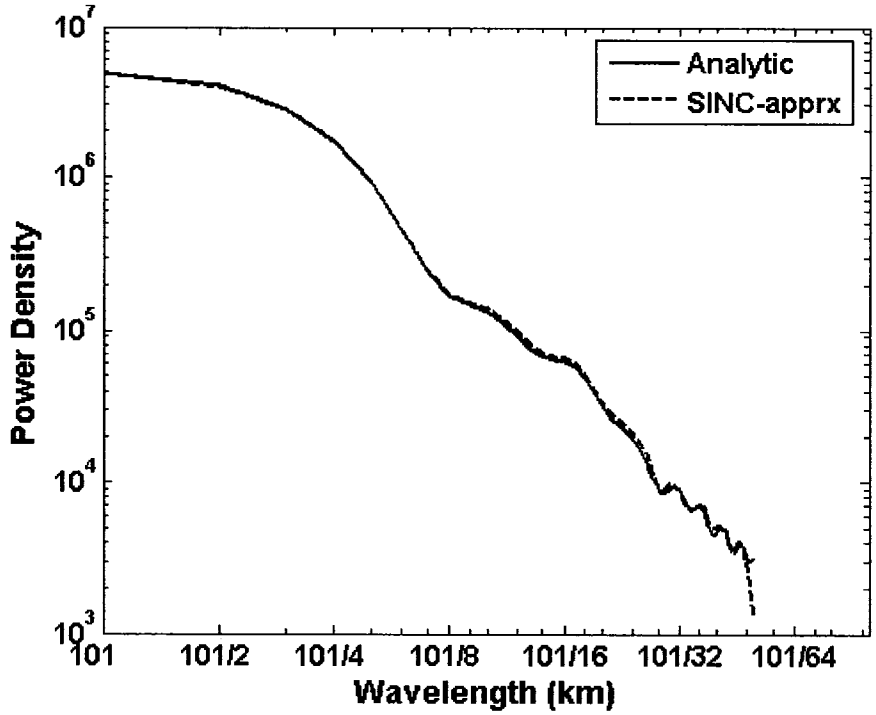

Figure 5. Comparison of average 1-D power spectrum (numerical diffusion along x-axis).

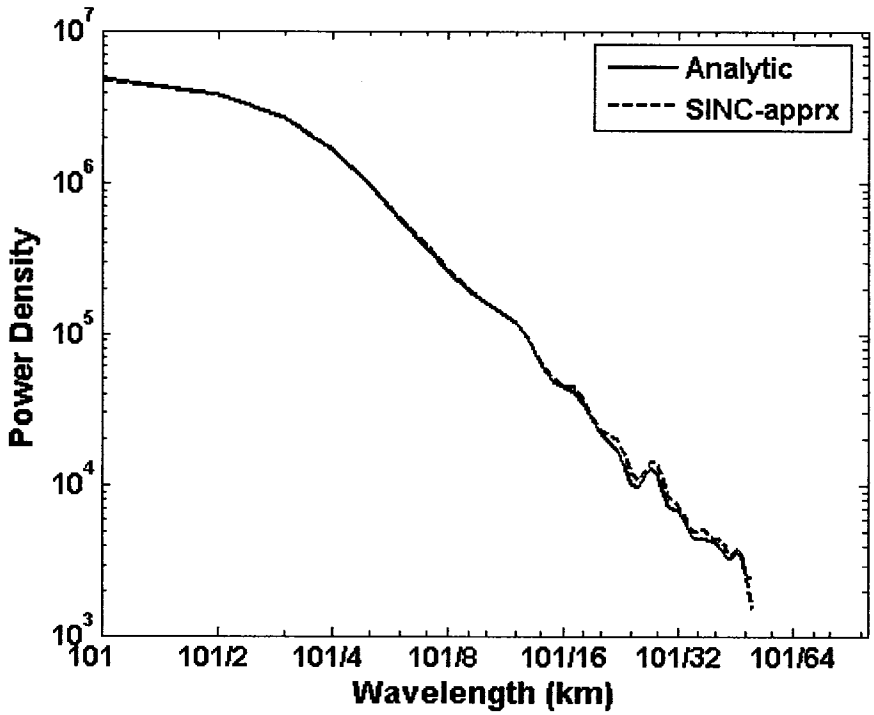

Figure 6. Comparison of average 1-D power spectrum (numerical diffusion along y-axis).

2.3. Performance Evaluation

To validate the spectral tracking algorithm developed in this chapter, we apply it to estimating motion fields for both synthesized reflectivity sequences and the observed radar reflectivity. For synthesized data we generate and hence know the ground truth of motion field, we can directly compare it with the estimated motion field. Quantitative statistics are computed to evaluate the performance of the spectral tracking algorithm. For the observed radar reflectivity, we apply the spectral algorithm to estimating motion fields and extrapolate the radar reflectivity for one hour in advance. We will compare the tracking based nowcast, using the spectral algorithm, with the "growth-decay storm tracker" (GDST) algorithm (Wolfson et al 1999; Theriault et al 2000; and Appendix A). The extrapolation of reflectivity fields is computed by the *SINC* approximation.

a. *Synthesized radar reflectivity sequences*

We have synthesized two reflectivity sequences to test the spectral algorithm for the global motion estimation. For both sequences, we generate a steady motion-flow field over the two-dimensional region: -50 km $\leq x, y \leq$ 50 km. A steady motion field is a time-independent flow field that does not change with time. The sampling interval is 1 km on both x-axis and y-axis. We use an observed reflectivity (dBZ) field as the initial image in both syntheses (Fig 7a).

Synthesis 1: We generate a radar image sequence of *80*-step span. The simple passive advection of reflectivity is simulated for this data set. The initial reflectivity image is evolved by the advection toward the north-east corner of the map using the pre-generated steady motion field (Fig 7). The arrows in Fig 7 display the simulated flow field. Example images of synthesized sequence demonstrate how the reflectivity field evolves

over time. Two rectangular regions are marked in Fig 7. In the non-data region the reflectivity keeps zero value in all synthesized images, so that the motion pattern never presents within this region. In contrast, from Fig 7d- 7h, we see that the precipitation field enters and sweeps over the data region. Applying the spectral algorithm to the synthesized images sequence, we estimate the motion-flow field and compare it with the given flow field (Fig 8). Results show that the estimated motion field agrees fairly well with the true flow field within both data region (Fig 9) and non-data region (Fig 10). The statistics for pixel-by-pixel comparison of flow fields in both x-direction (U-field) and y-direction (V-field) are presented in Table 1.

Synthesis 2: In this synthesis a localized steady source is added along with advection terms. Here the term, $S(x, y, t) \equiv S(x, y)$ in Eq 2.1, is interpreted as the growth mechanism ($S(x, y) \geq 0$) that is time-independent and spatially localized. $S(x, y)$ is a Gaussian-shaped source term that is centered at (10km, 10km), as shown in Fig 12. We have compared two different ways of applying the spectral algorithm to the synthesized reflectivity sequence: 1) S-term is not present in the estimation algorithm and, 2) S-term is present in the estimation algorithm (see Eq 2.1). With the S-term added in the spectral algorithm, we may gain significant improvement for the flow-field estimation near the region where the growth mechanism presents (Fig 11). Quantitative results for the comparison around the growth center ($5 \text{ km} \leq x, y \leq 15 \text{ km}$) are shown in Table 1. The flow-field has the larger V-values than U-values around the growth center ($5 \text{ km} \leq x, y \leq 15 \text{ km}$), so the estimation for V-field has the better performance than that for U-field, as shown in Table 1. For the estimation with S-term added, the spectral algorithm is able to identify the growth term $S(x, y)$ (Fig 13).

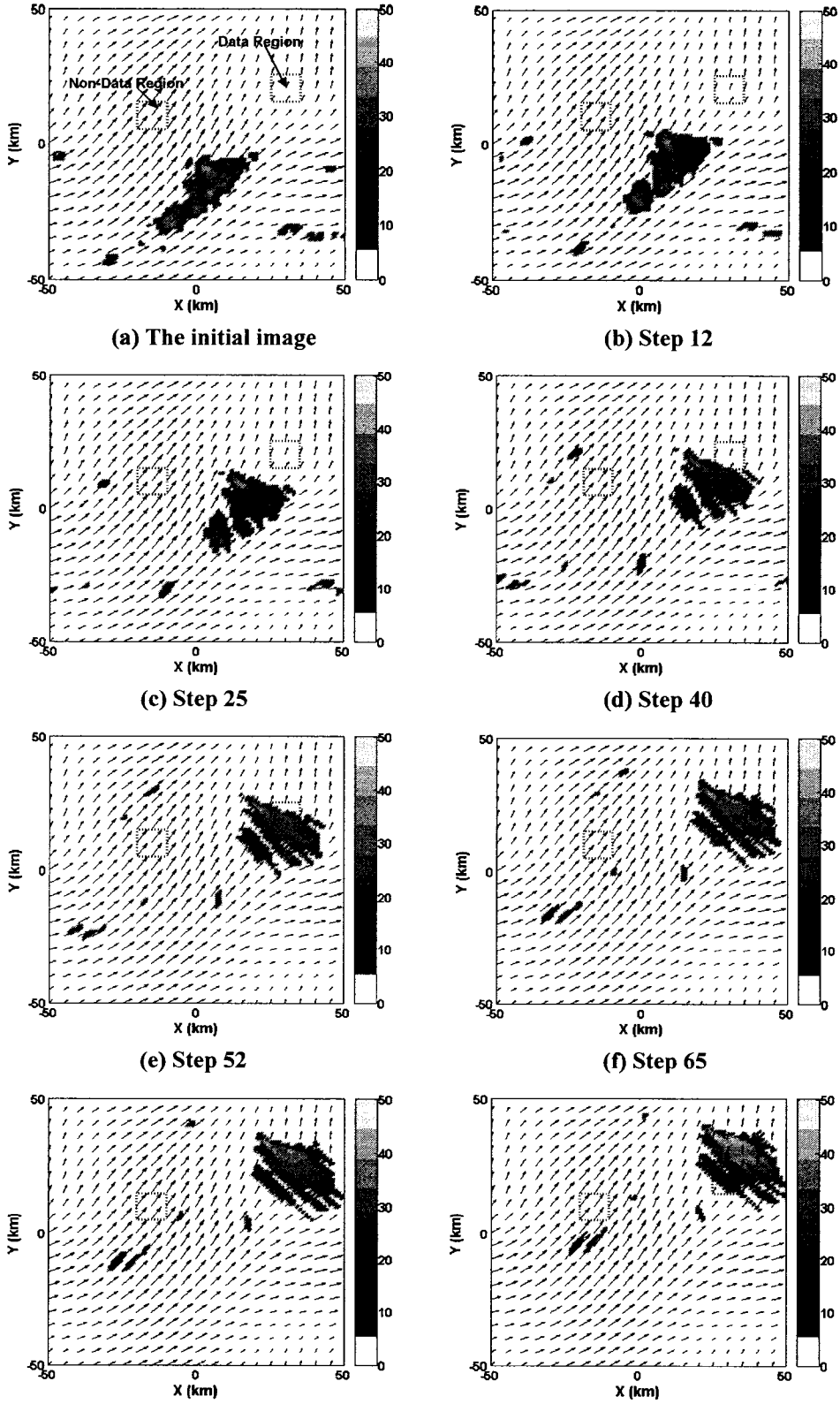

(a) The initial image (b) Step 12

(c) Step 25 (d) Step 40

(e) Step 52 (f) Step 65

(g) Step 72 (h) Step 80

Figure 7. Example images in synthesized reflectivity sequence (synthesis 1).

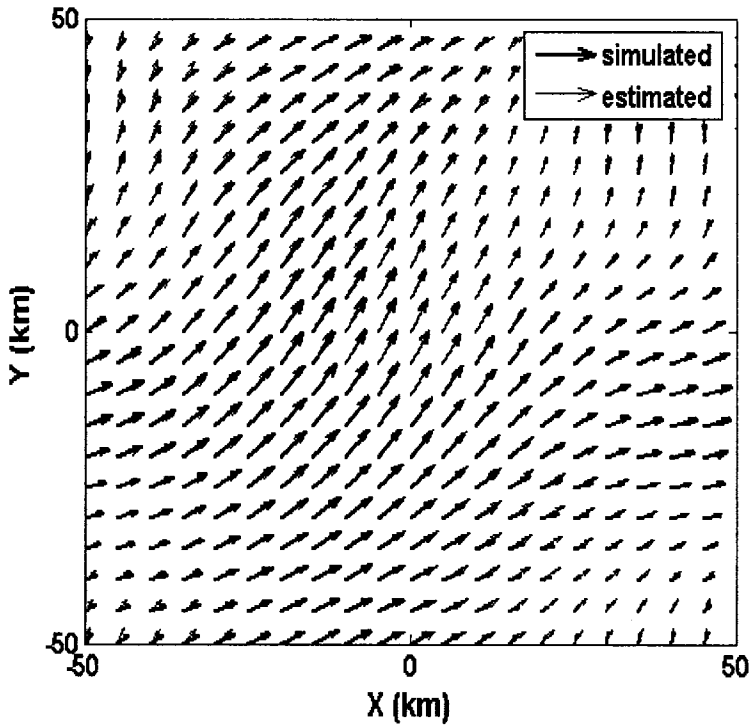

Figure 8. Comparison of true motion field (simulated) and estimated motion field in synthesis 1.

Table 1. Statistics for pixel-by-pixel comparison between estimated flow fields and true flow fields. The unit of flow-field velocity is km step^{-1}. CORR is the correlation coefficient. NSE is the normalized standard error in percent. SNR is the equivalent signal-to-noise ratio for estimation in dB. The statistics for synthesis 1 is conducted over the whole 2-D map (*-50* km $\leq x, y \leq$ *50* km). The statistics for synthesis 2 is conducted over the region near the growth center (*5* km $\leq x, y \leq$ *15* km). In synthesis 2, the parameters for S-term, U-field and V-field are the same as those shown in Fig 12.

		U-field				
		Bias	Std. Dev.	CORR	NSE (%)	SNR (dB)
Synthesis 1		-0.03	0.09	0.91	16	7.37
Synthesis 2	without S-term	-0.1	0.1	0.69	28	-8.3
	with S-term	-0.05	0.05	0.88	15	-2.79
		V-field				
		Bias	Std. Dev.	CORR	NSE (%)	SNR (dB)
Synthesis 1		-0.002	0.09	0.9	15	7.36
Synthesis 2	without S-term	-0.09	0.1	0.93	14	-3.53
	with S-term	-0.05	0.05	0.98	7	1.76

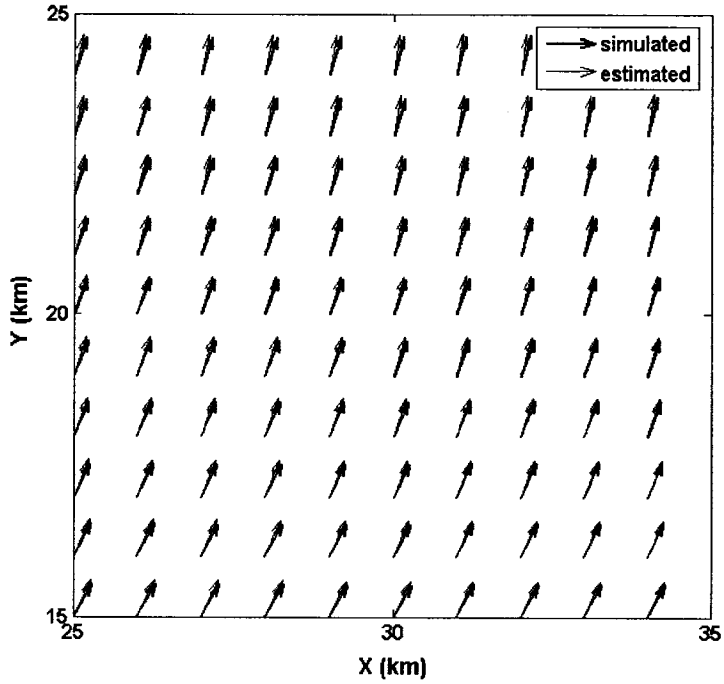

Figure 9. Comparison of true flow-field and estimated flow-field by the spectral algorithm: the zoomed-in region where the precipitation field ever presents (synthesis 1).

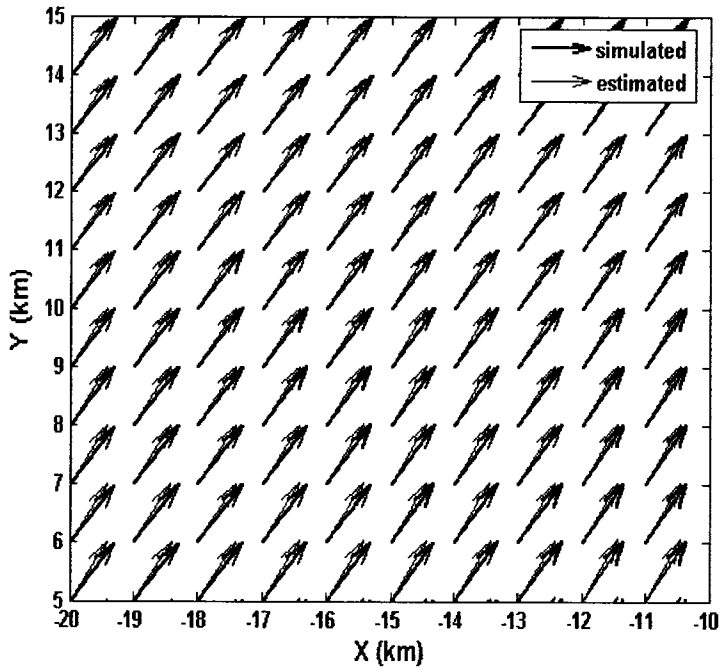

Figure 10. Comparison of true flow-field and estimated flow-field by the spectral algorithm: the zoomed-in region where the precipitation field never presents (synthesis 1).

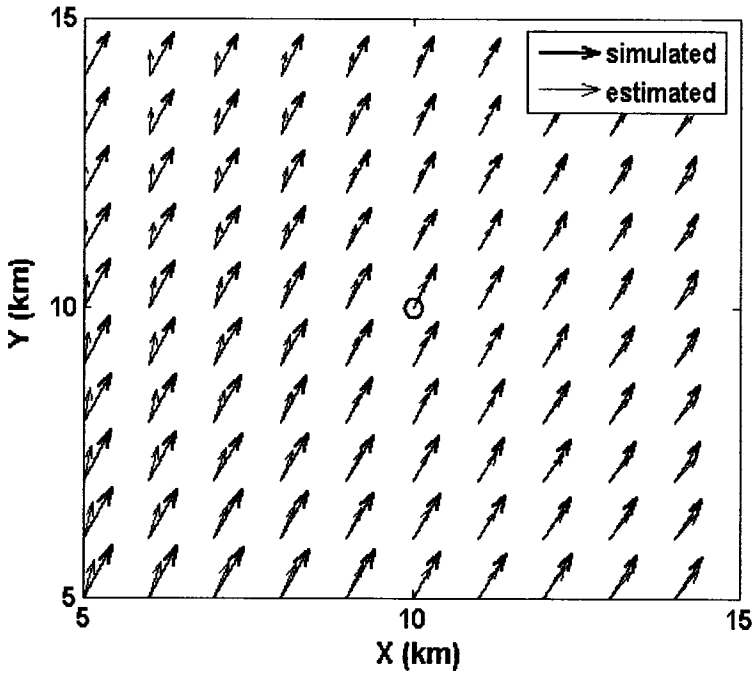

(a)

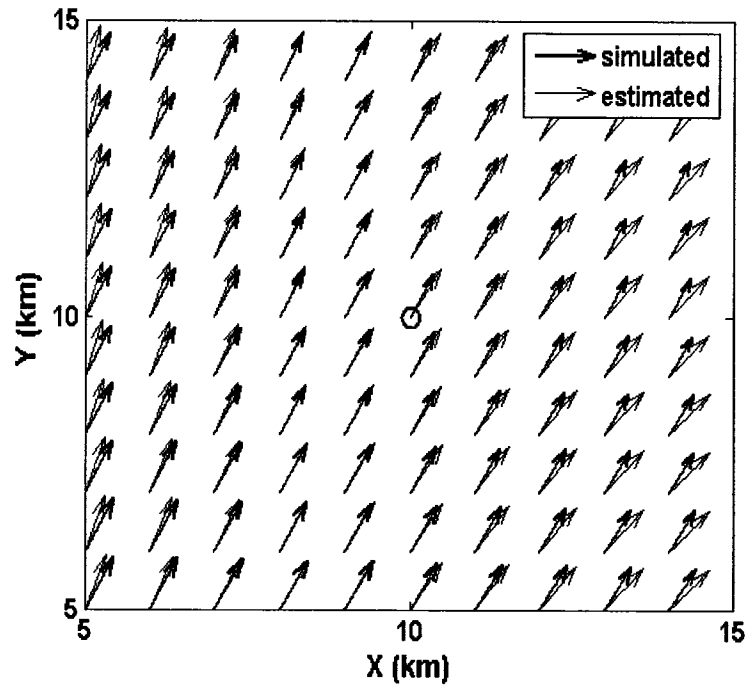

(b)

Figure 11. Comparison of the estimated flow fields by the spectral algorithm near the growth center: $x = 10$ km, $y = 10$ km, (a) without S-term, and (b) with S-term added in Eq 2.1. Averaged U- and V-field values are both scaled to 0.05 km step^{-1}. The peak value of S-term is scaled to 1.0 dBZ step^{-1}. The open circles indicate the growth center.

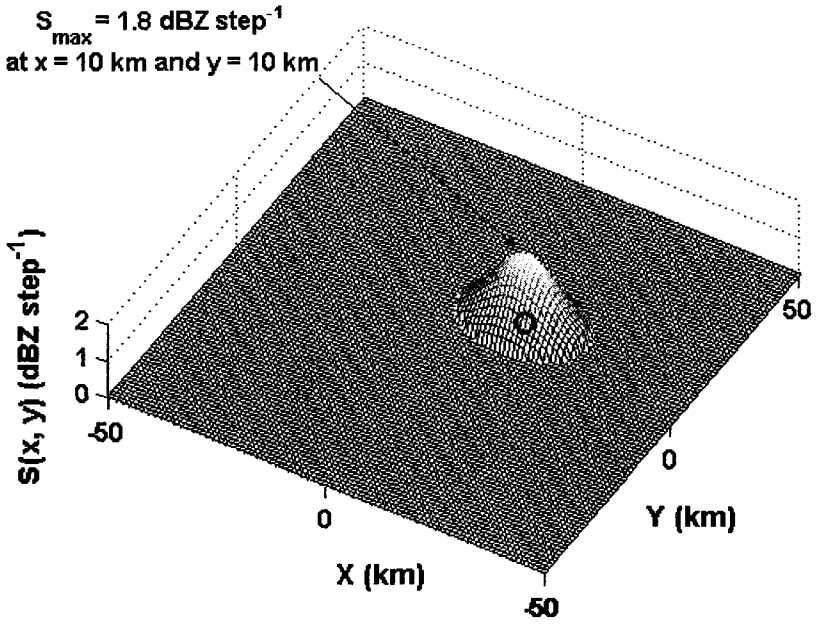

Figure 12. Steady S-term, $S(x, y)$, a two-dimensional Gaussian function with central peak located at $x = 10$ km and $y = 10$ km, which is used to simulate the localized growth mechanism. (Averaged U- and V-field values are both scaled to 0.5 km step^{-1} in synthesis 2).

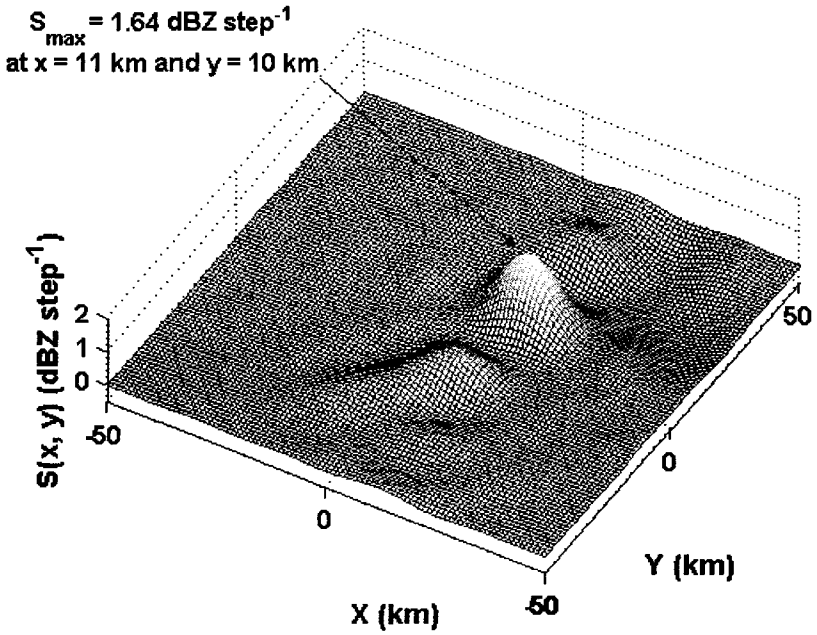

Figure 13. Estimated S-term, $S_{est}(x, y)$, using the spectral algorithm in Eq 2.1, whose central peak is determined to be at $x = 11$ km and $y = 10$ km. This automatically identified growth term matches the "true" S-term fairly well (synthesis 2).

b. *Observed radar reflectivity*

To further validate the spectral tracking algorithm, we have applied it to three sets of observed radar reflectivity (dBZ).

The first set of reflectivity data was collected by the WSR-88D radar (Melbourne, FL) during the storm event from 2102 UTC 23 August to 0057 UTC 24 August, 1998. This temporal sequence of radar images spans approximately 4 hr. The WSR-88D radar takes approximately 5 min to finish a volume scan. Each volume of PPI scan was converted to the CAPPI data in Cartesian coordinates. The interpolated 2D radar images at the height of 1 km above the ground are used in this study. The re-sampled radar images are in the two-dimensional region: -50 km $\leq x \leq 50$ km and -50 km $\leq y \leq 50$ km. The spatial sampling interval is 1 km on both x-axis and y-axis. The temporal sampling interval is 5 min whereas each image is projected onto regular points on time axis. Therefore we obtain a sequence of 48 radar images that are equally sampled on time axis. The spectral tracking algorithm is applied for each 6 consecutive radar images that span 25 min. Each estimated motion field is used to extrapolate for the next successive 12 radar images. Therefore this set gives us predicted radar images up to 1 hr. An example of the predicted reflectivity (30 min and 60 min) compared with the observed reflectivity is shown in Figure 14 (a).

The second set of reflectivity data was from the KOUN radar (Norman, OK) during the storm event from 0340 UTC to 0959 UTC 06 June, 2003. This temporal sequence of radar images spans approximately 6 hr 20 min. The KOUN radar takes approximately 6.5 min for each volume scan. Each volume of PPI scan was converted to the CAPPI data in Cartesian coordinates. The interpolated 2D radar images at the height of 1 km

above the ground are used. The re-sampled radar images are in the two-dimensional region: -350 km $\leq x \leq$ 350 km and -350 km $\leq y \leq$ 350 km. The spatial sampling interval is 1 km on both x-axis and y-axis. By projecting each image onto regular temporal points, we obtain a sequence of 59 radar images that are equidistantly sampled over time. The sampling interval is 6.5 min. The spectral tracking algorithm is applied for each 6 consecutive radar images that span approximately 30 min. Each estimated motion field is used to extrapolate for the next successive 9 radar images. This gives us predicted radar images up to approximately 1 hr. An example of the predicted reflectivity (30 min and 60 min) compared with the observed reflectivity is shown in Figure 14 (b).

The third set of reflectivity images was collected and merged from the four-radar network in the CASA IP1 project. The four radars of CASA IP1 are located at Chickasha (KSAO), Cyril (KCYR), Lawton (KLWE), and Rush Springs (KRSP) in Oklahoma. These are the X-band (3-cm) radars, each of which has a beam-width of 1.8 degree and a range of 30 km. The reflectivity has been corrected to compensate the path-integrated attenuation. The data from the CASA IP1 project has much higher spatial and temporal resolutions. The sequence of radar images spans approximately 48 min (00:10 UTC – 00:57 UTC, AUG 27, 2006), and the temporal resolution is approximately 30 sec. We therefore have 95 successive images in total. The storm event was associated with a cold front and the flash flood warnings were issued. PPI scans are converted to the CAPPI data in Cartesian coordinates. The interpolated 2D radar images at the height of 2.5 km above the ground are used for this study. The re-sampled radar images are in the two-dimensional region: -60 km $\leq x \leq$ 60 km and -50 km $\leq y \leq$ 70 km. The coordinate origin is at the center of four CASA radars. The spatial sampling resolution is 0.5 km on

both x-axis and y-axis. The spectral tracking algorithm is applied for each 25 consecutive radar images that span approximately 12.5 min. Each estimated motion field is used to extrapolate for the next successive 10 radar images. Subsequently this gives us the predicted radar images for five minutes. An example of the predicted reflectivity fields (5 min), using the spectral algorithm and the GDST-based algorithm, compared with the observed reflectivity field is shown in Figure 15.

We adopt three scores commonly used in the literature (Wilson et al, 1998; Wolfson et al 1999) to evaluate the forecasting performance:

1) critical success index (CSI), defined by

$$\mathrm{CSI} \equiv \frac{a}{a+b+c} \tag{2.10}$$

2) probability of detection (POD), defined by

$$\mathrm{POD} \equiv \frac{a}{a+b} \tag{2.11}$$

3) false alarm rate (FAR), defined by

$$\mathrm{FAR} \equiv \frac{c}{a+c} \tag{2.12}$$

where "*a*" is the number of correct detection of occurring event, "*b*" is the number of missed detection of occurring event, and "*c*" is the number of false detection of non-occurring event. Hereafter the rain event is defined as that a reflectivity (dBZ) value, on the neighbouring region of specified size, is found to be larger than the given threshold reflectivity value.

These scores are computed on a neighbouring region of *4* km × *4* km grids, with one level of reflectivity threshold (*25* dBZ), for the data from the WSR-88D radar (Melbourne, FL) and the KOUN radar (Norman, OK). For the data set from the four-

radar network (CASA IP1) in Oklahoma, the forecast scores are computed on a neighbouring region of *2* km × *2* km grids, with one level of reflectivity threshold (*30* dBZ). For the observed radar reflectivity, we do not know the true motion fields of the storm. Therefore we compare the nowcasting scores using the spectral algorithm with the "growth-decay storm tracker" (GDST) algorithm (Theriault et al, 2000). Results are shown in Figures 16 and 17, where the forecasting scores are averaged over all predictions of the same lead-time. These results reveal that the spectral tracking algorithm performs equally well or better than the GDST algorithm. It is notable in Fig 17 that the spectral tracking algorithm performs significantly better than the GDST based algorithm for the high-resolution data from the CASA IP1 radars. The impact of the sampling resolution on the nowcasting performance of the spectral algorithm and the GDST algorithm is studied in the next section.

The spectral algorithm developed in this research has demonstrated good and robust performance for the radar reflectivity tracking and nowcasting. It has shown the promising potential for operational applications. Therefore further studies are conducted concerning the real-time application of the new tracking and nowcasting system developed here. These studies will be detailed in section 2.4.

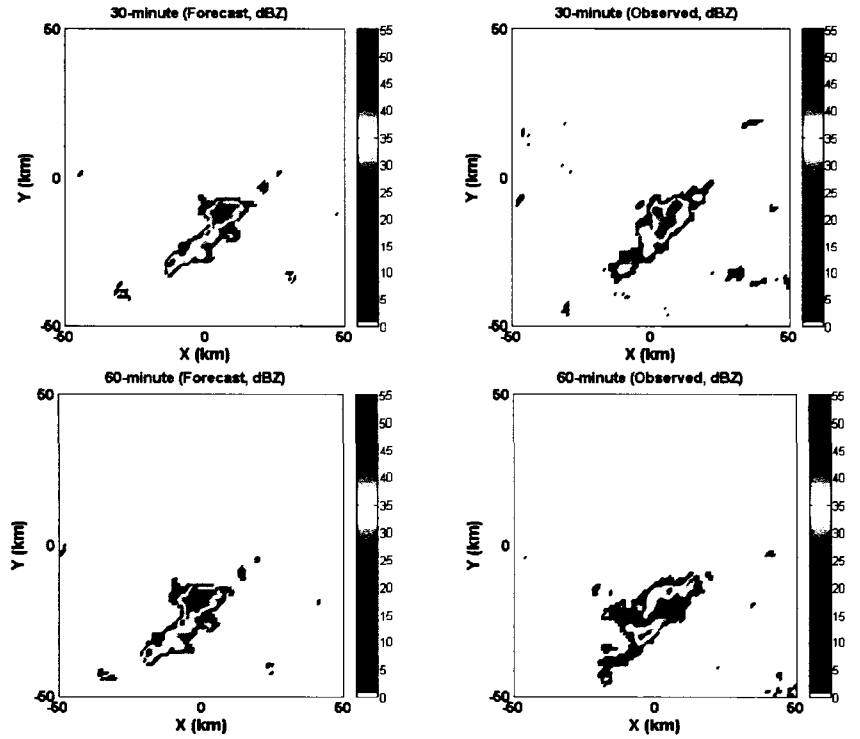

(a)

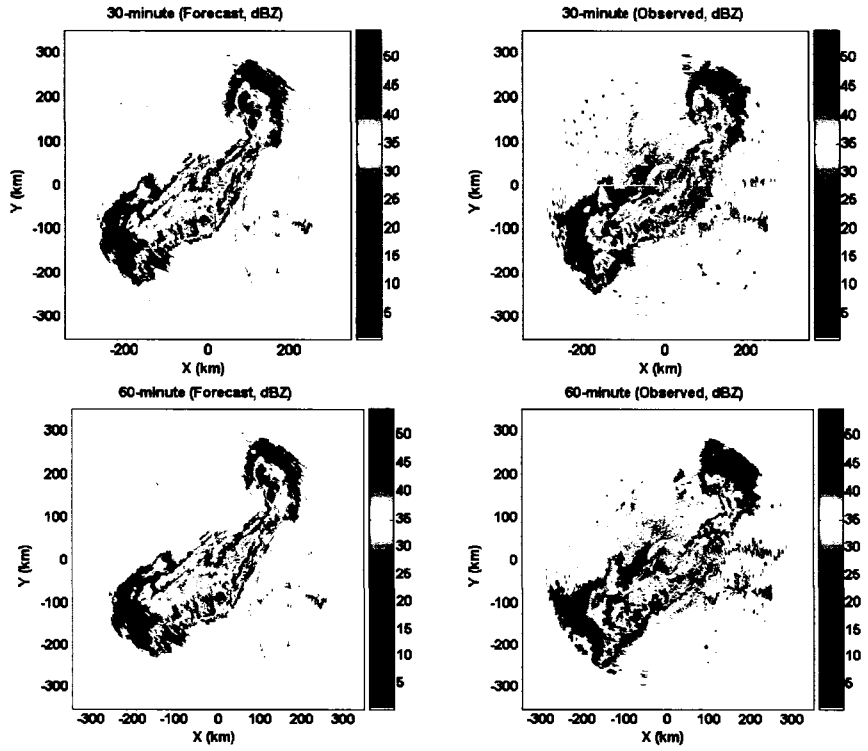

(b)

Figure 14. Comparison of forecast reflectivity and observed reflectivity from a) WSR-88D radar, Melbourne FL, b) KOUN radar, OK, for *30* min and *60* min, based on the motion tracking using the spectral algorithm.

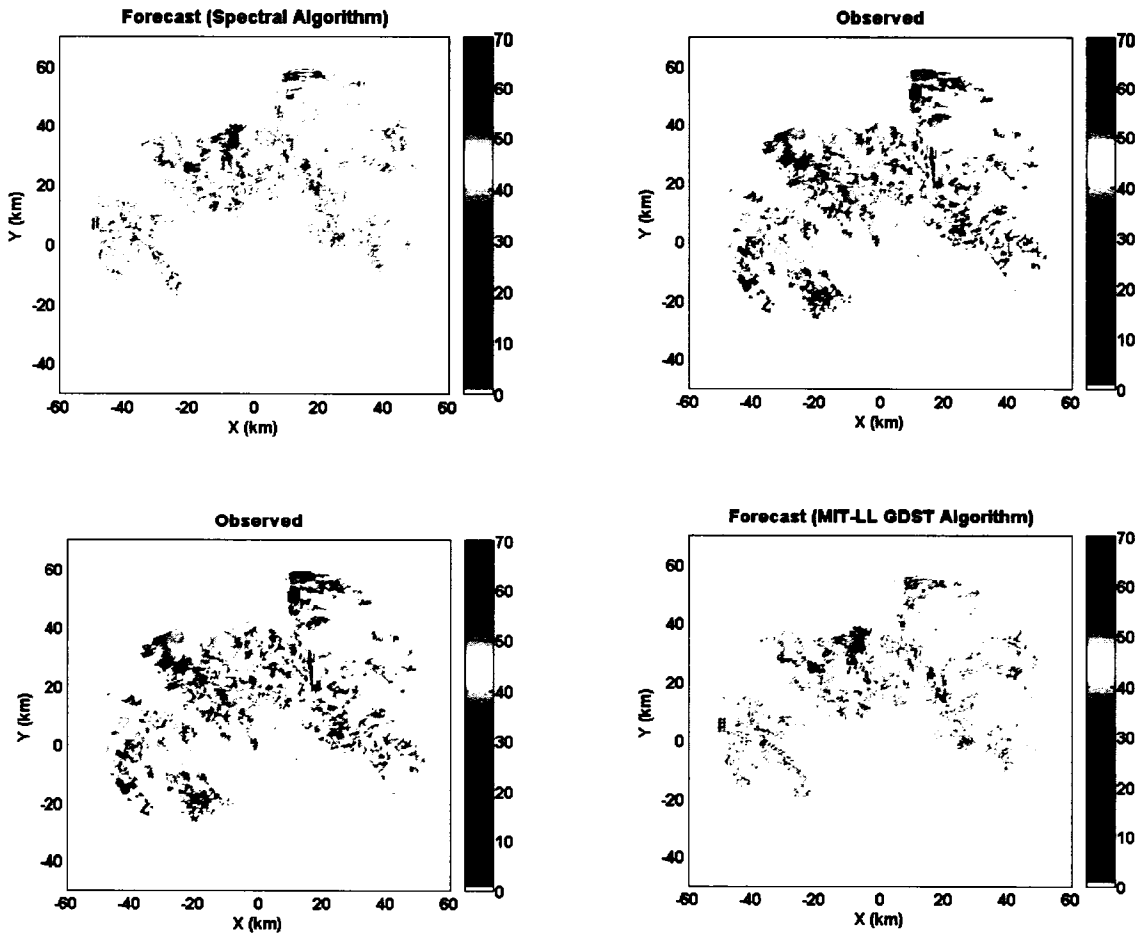

Figure 15. Comparison of predicted reflectivity fields (5-minute) and observed reflectivity fields from the four-radar network in Oklahoma (CASA IP1): predicted reflectivity fields are based on the spectral tracking algorithm (upper-left panel) and the GDST-based algorithm (lower-right panel).

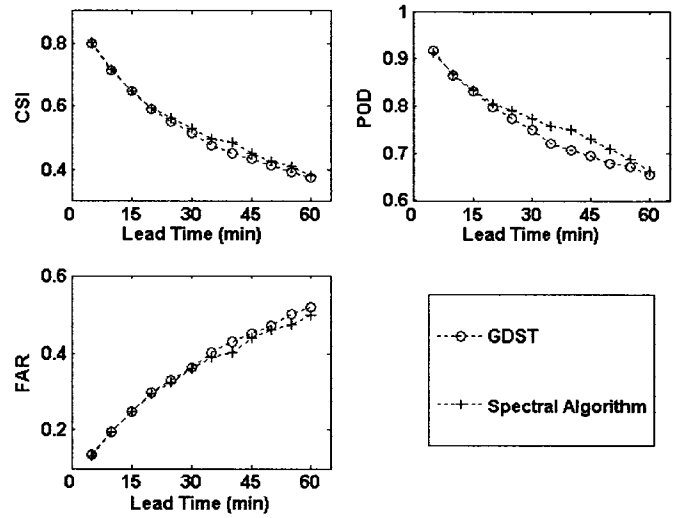

(a)

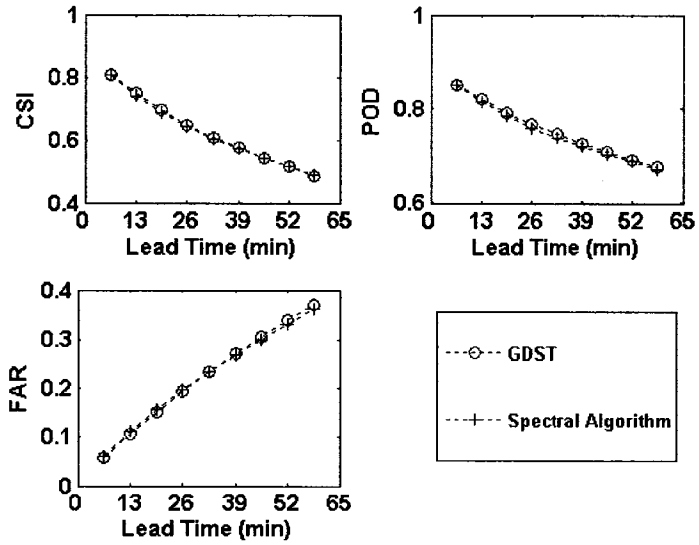

(b)

Figure 16. Nowcasting scores for observed radar data collected by: a) the WSR-88D radar (Melbourne, FL), b) the KOUN radar, OK. The spectral algorithm is compared with the "growth-decay storm tracker" (GDST) based algorithm. Horizontal axis is the leading time of nowcasting. CSI is the critical success index. POD is the probability of detection. FAR is the false alarm rate. Scores are computed over the neighboring grids of *4* km × *4* km (threshold *25* dBZ), and are averaged over all predictions of the same leading time.

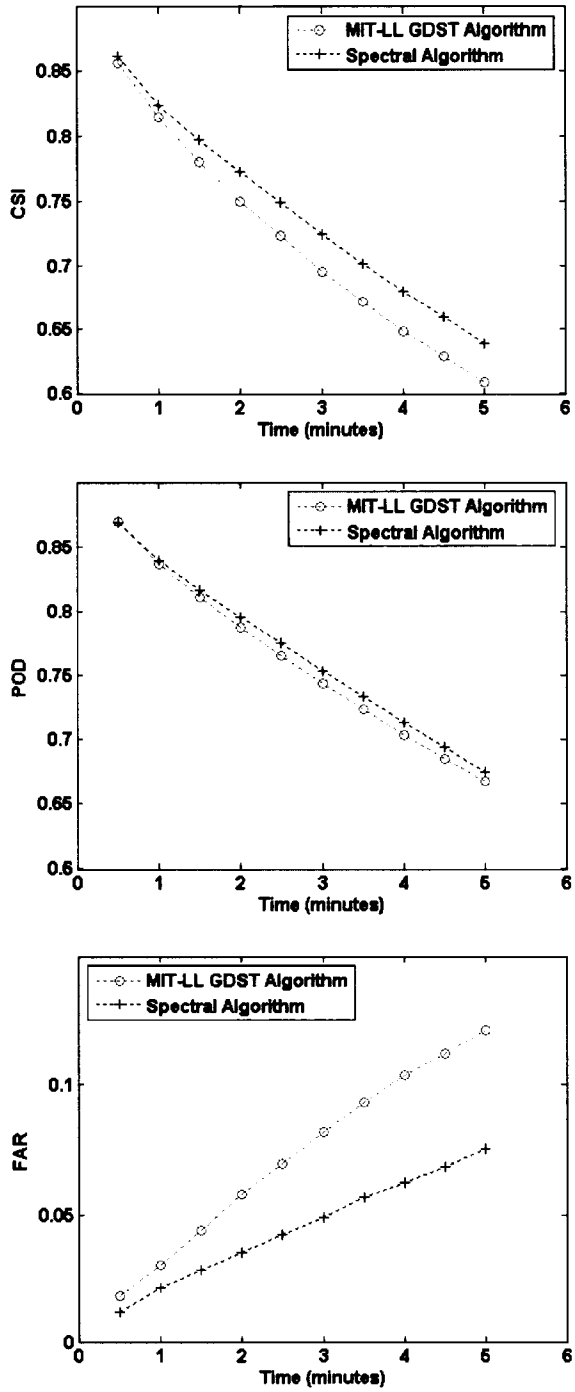

Figure 17. Nowcasting scores for observed radar data collected and merged from the four-radar network (KSAO, KCYR, KLWE, and KRSP) in the CASA IP1 project (OK). The spectral algorithm is compared with the "growth-decay storm tracker" (GDST) based algorithm. Horizontal axis is the leading time of nowcasting. CSI is the critical success index. POD is the probability of detection. FAR is the false alarm rate. Scores are computed over the neighboring grids of *2* km × *2* km (threshold *30* dBZ) and are averaged over all predictions of the same leading time.

c. *The effect of sampling resolution*

It is shown in Fig 17 that the spectral tracking algorithm performs significantly better than the GDST based algorithm for the high-resolution data from the CASA IP1 radars. Motivated by better understanding the impact of the sampling resolution on the nowcasting performance of the spectral algorithm and the GDST algorithm, we have conducted further studies using the reflectivity data collected by the CASA IP1 radars.

The reflectivity images were collected and merged from the four-radar network in the CASA IP1 project. The reflectivity values have been corrected to compensate the path-integrated attenuation. The data from the CASA IP1 project has high spatial and temporal resolutions. The sequence of radar images used in this study spans approximately 113 minutes (22:50 UTC August 15 – 00:44 UTC, August 16, 2006), and the temporal resolution is approximately 30 seconds. Therefore we have totally 225 successive images in the sequence. PPI scans are interpolated and merged to generate the CAPPI data in Cartesian coordinates. The interpolated 2D radar images at the height of 2.5 km above the ground are used for this study. The re-sampled radar images are in the two-dimensional region: -60 km $\leq x \leq$ 60 km and -*50* km $\leq y \leq$ 70 km. The origin of coordinates is at the center of four CASA radars. To study the effect of different sampling resolutions, two sets of re-sampled reflectivity sequences are obtained. In the first set of reflectivity sequences, the temporal resolution is fixed by 30 seconds and the spatial resolutions of re-sampled reflectivity images are 0.5 km and 1.0 km respectively. In the second set of reflectivity sequences, the spatial resolution is fixed by 0.5 km and the temporal resolutions of re-sampled reflectivity sequences are 30 seconds, 1 minute, 2 minutes and 3 minutes respectively. For each re-sampled reflectivity sequence, each 25

consecutive images are used for the motion estimation and the estimated motion field is applied to forecasting the reflectivity images in the next 30 minutes. The nowcasting scores are averaged over all predictions of the same lead time.

For the first set of reflectivity sequences, 30-minute forecasts are conducted using both the spectral tracking algorithm and the GDST algorithm. Results are shown in Fig 18 and Fig. 19. These results reveal that the higher spatial resolution significantly suppresses the false alarm rate for both the spectral tracking algorithm and the GDST based algorithm.

For the second set of reflectivity sequences, 30-minute forecasts are conducted using both the spectral tracking algorithm and the GDST based algorithm. Results are shown in Fig 20 and Fig 21. From Fig 20 it is seen that as the temporal resolution changes from 30 seconds to 3 minutes, the false alarm rate consistently increases for the spectral algorithm. From Fig 21 it is seen that as the temporal resolution changes from 30 seconds to 3 minutes, the false alarm rate varies in the more complex way for the GDST algorithm. The resolution of 1 minute gives the lowest false alarm rate for the GDST algorithm. For both algorithms the detection rate (POD) slightly and consistently increases when the resolution changes from 0.5 minutes to 1 minute. It is seen that the resolution of 1 minute gives the highest CSI scores for both algorithms.

Based on the above studies, the comparison of nowcasting scores between the spectral algorithm and the GDST algorithm are obtained using the reflectivity sequence with the spatial resolution of 0.5 km and the temporal resolution of 1 minute. The result is shown in Fig 22 (b). Fig 22 shows that the spectral algorithm consistently outperforms the GDST based algorithm.

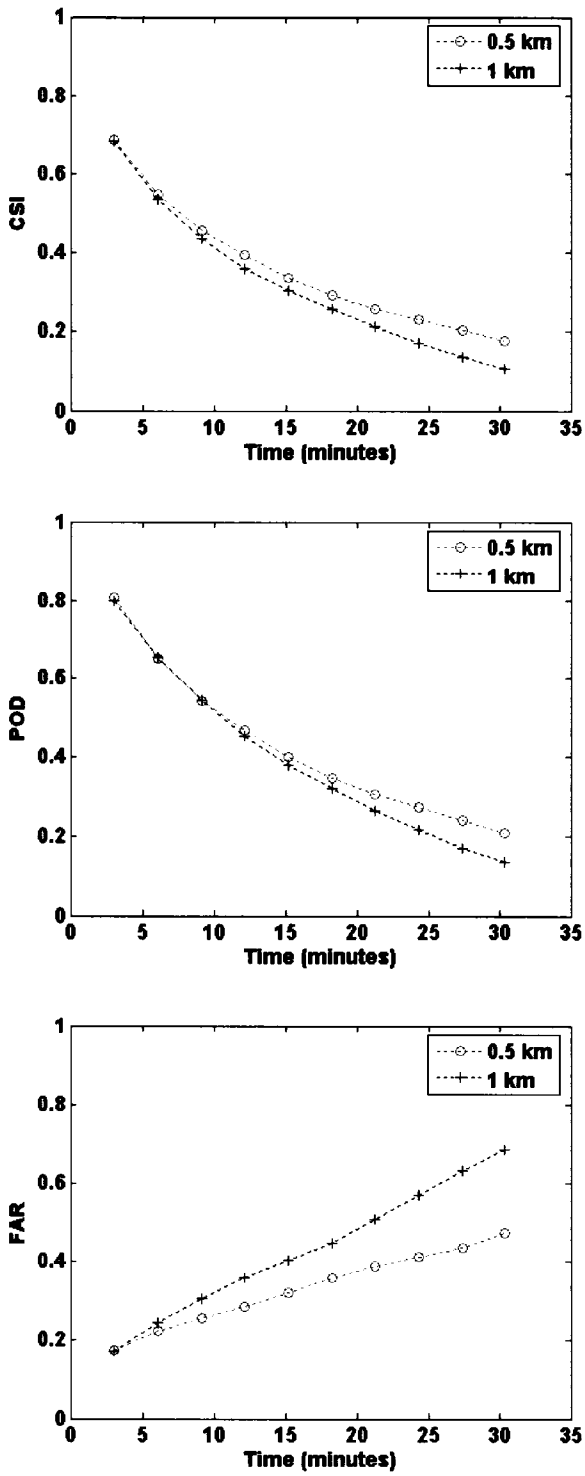

Figure 18. Nowcasting scores for observed reflectivity data collected and merged from the four-radar network (KSAO, KCYR, KLWE, and KRSP) in CASA IP1 project (OK, Aug 15 – Aug 16, 2006). The spectral tracking algorithm is applied on two reflectivity sequences. Spatial resolutions of two sequences are 0.5 km and 1 km, respectively. Scores are computed over the neighboring grids of *4* km × *4* km (threshold *25* dBZ) and are averaged over all predictions of the same leading time.

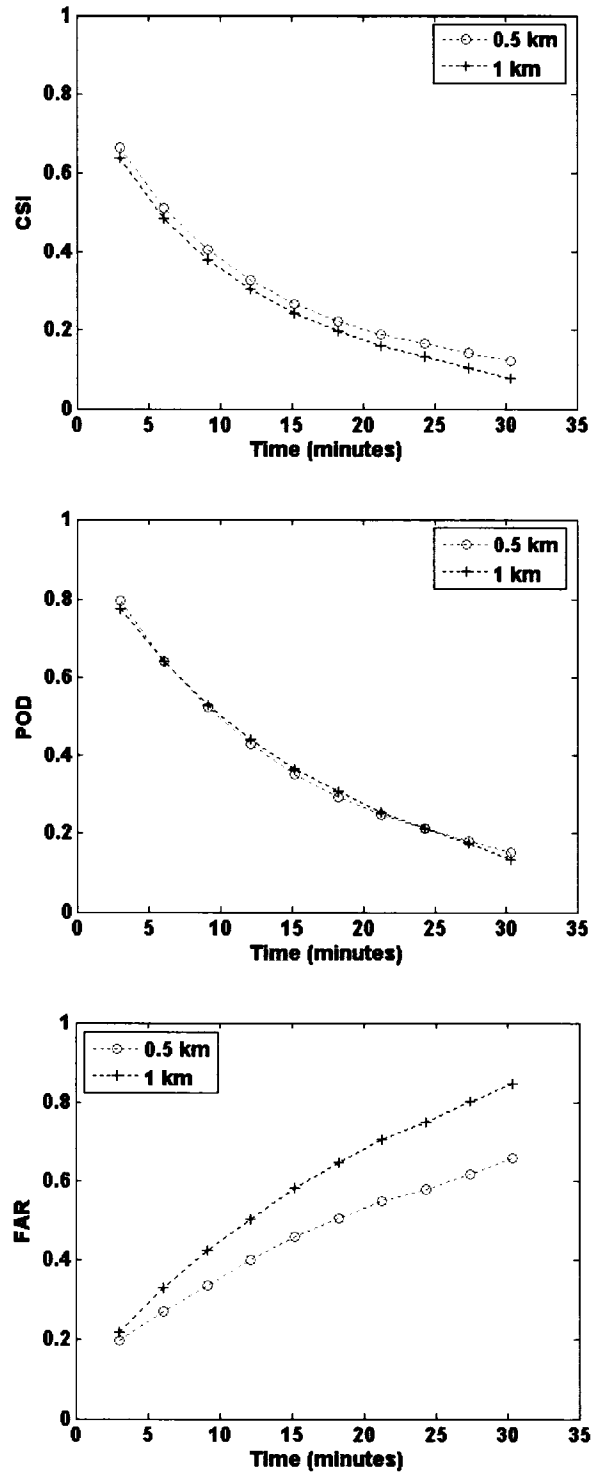

Figure 19. Nowcasting scores for observed reflectivity data collected and merged from the four-radar network (KSAO, KCYR, KLWE, and KRSP) in CASA IP1 project (OK, Aug 15 – Aug 16, 2006). The GDST based algorithm is applied on two reflectivity sequences. Spatial resolutions of two sequences are 0.5 km and 1 km, respectively. Scores are computed over the neighboring grids of *4* km × *4* km (threshold *25* dBZ) and are averaged over all predictions of the same leading time.

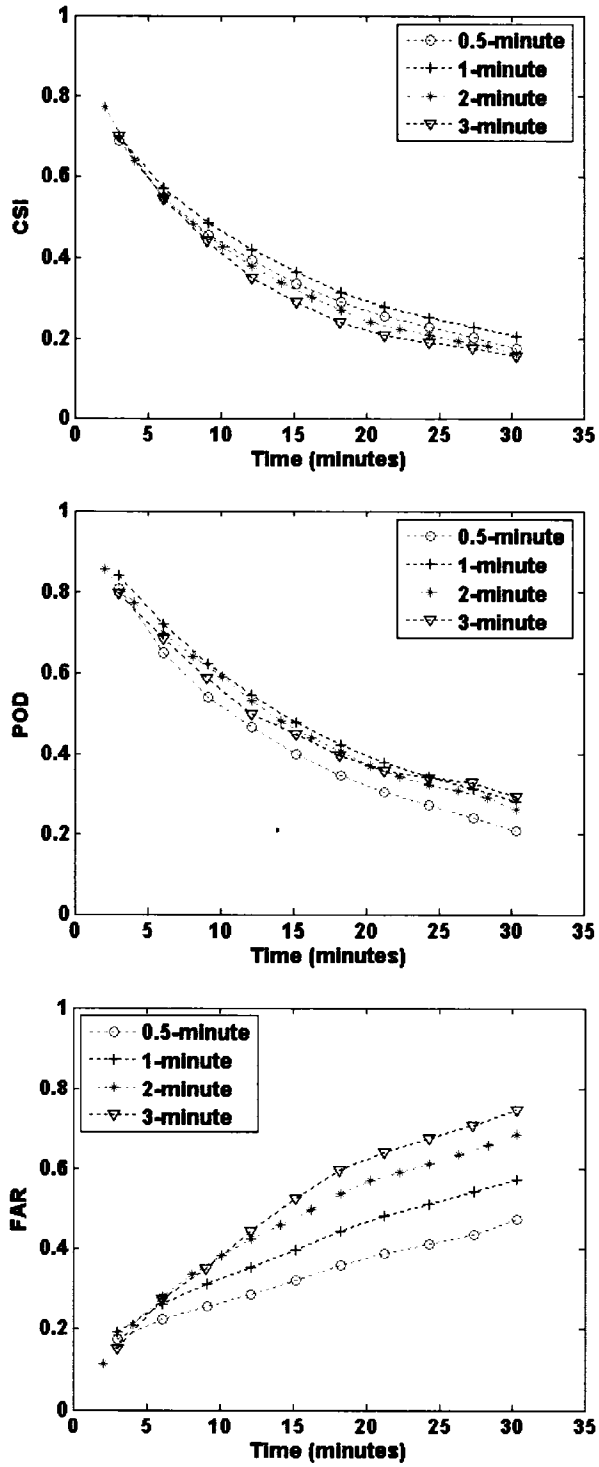

Figure 20. Nowcasting scores for observed reflectivity data collected and merged from the four-radar network (KSAO, KCYR, KLWE, and KRSP) in CASA IP1 project (OK, Aug 15 – Aug 16, 2006). The spectral tracking algorithm is applied on four reflectivity sequences. Temporal resolutions of four sequences are 30 sec, 1 min, 2 min and 3 min, respectively. Scores are computed over the neighboring grids of *4* km × *4* km (threshold *25* dBZ) and are averaged over all predictions of the same leading time.

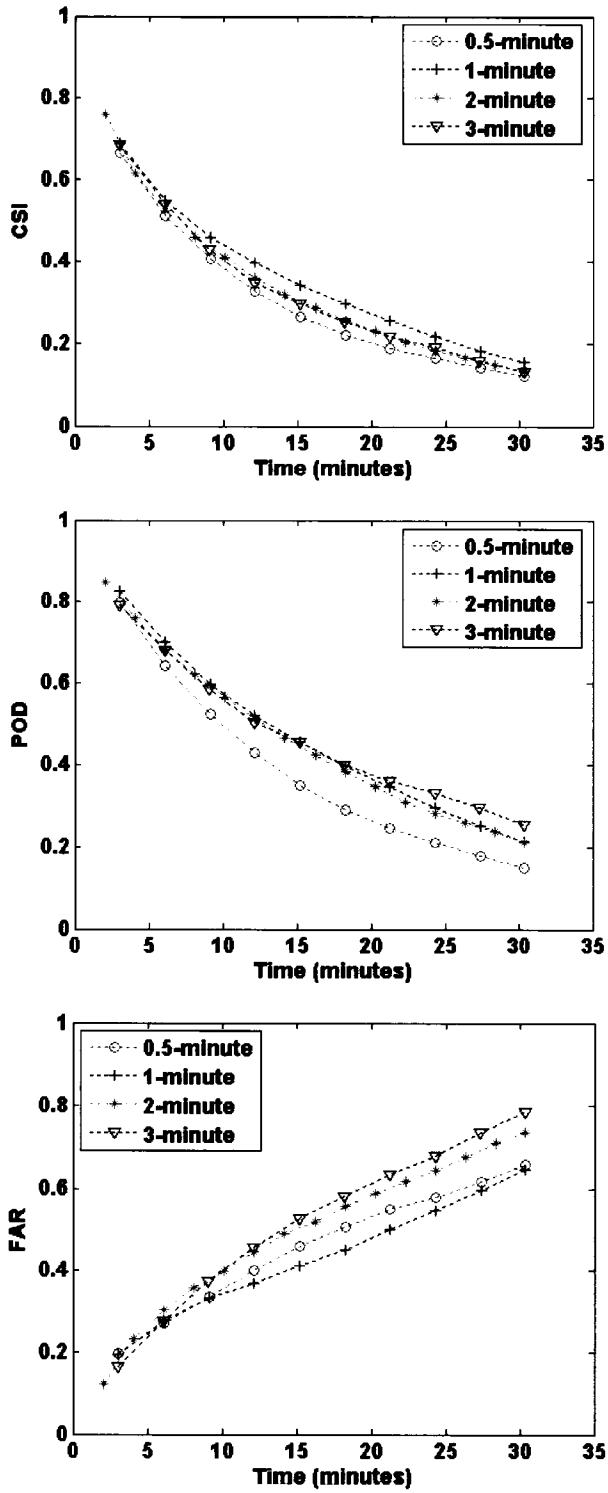

Figure 21. Nowcasting scores for observed reflectivity data collected and merged from the four-radar network (KSAO, KCYR, KLWE, and KRSP) in CASA IP1 project (OK, Aug 15 – Aug 16, 2006). The GDST based algorithm is applied on four reflectivity sequences. Temporal resolutions of four sequences are 30 sec, 1 min, 2 min and 3 min, respectively. Scores are computed over the neighboring grids of *4* km × *4* km (threshold *25* dBZ) and are averaged over all predictions of the same leading time.

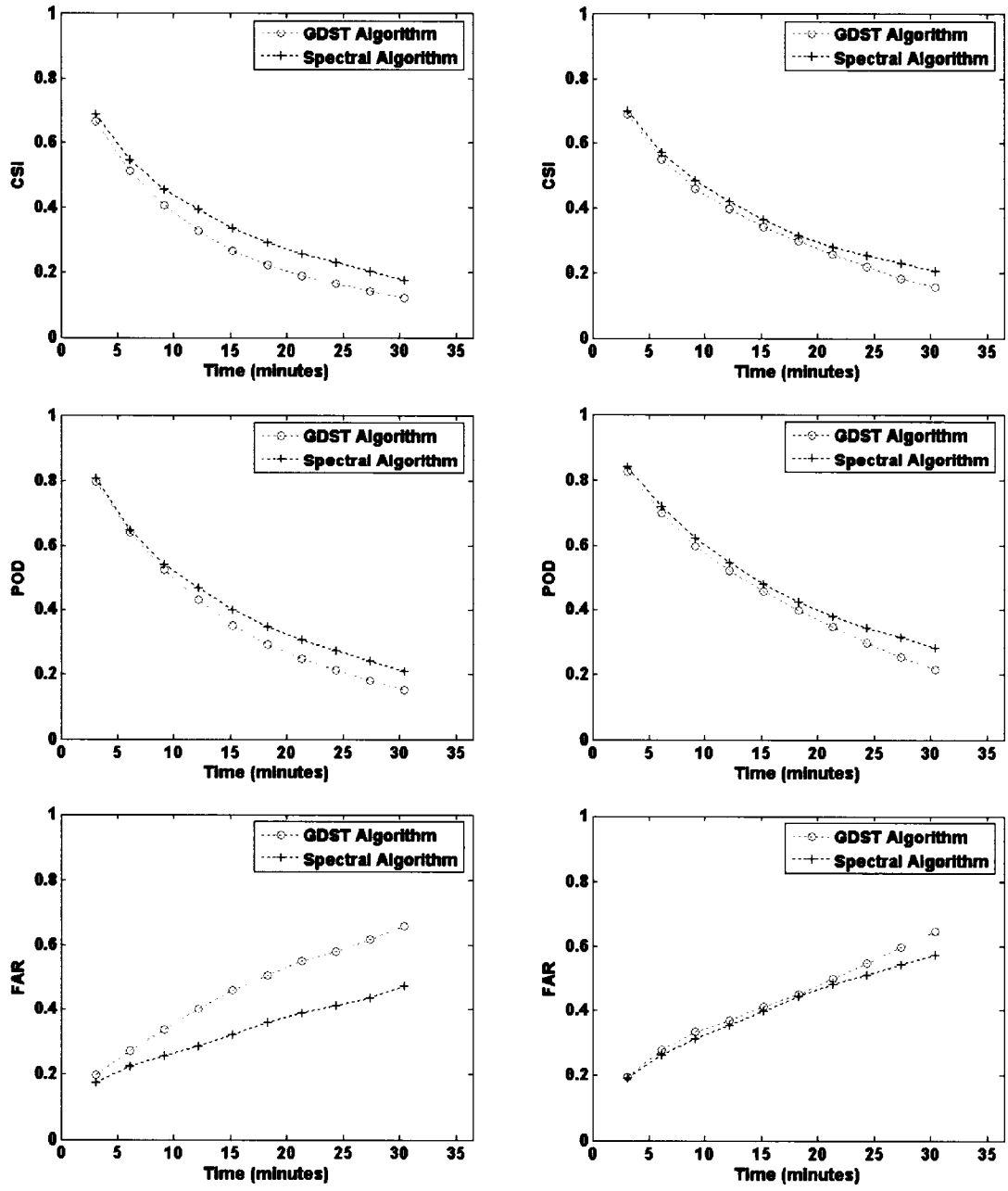

Figure 22. Nowcasting scores for observed reflectivity data collected and merged from the four-radar network in CASA IP1 project (OK, Aug 15 – Aug 16, 2006): (a) the spatial resolution is 0.5 km and the temporal resolution is 30 sec; (b) the spatial resolution is 0.5 km and the temporal resolution is 1 minute. The spectral algorithm is compared with the GDST based algorithm. Scores are computed over the neighboring grids of *4* km × *4* km (threshold *25* dBZ).

2.4. Feasibility of the Real-time Application of the Spectral Tracking and Nowcasting System

The Dynamic and Adaptive Radar Tracking of Storms (DARTS) based on the spectral algorithm has been developed and evaluated in above sections. DARTS has demonstrated the good and robust performance for the radar reflectivity tracking and nowcasting. Built upon these encouraging studies, the DARTS may be applied to operational applications. Therefore further studies are conducted in this section concerning the real-time application of the new tracking and nowcasting system.

Various case studies above have shown that DARTS can perform equally well or slightly better than the GDST algorithm. For operational applications, several practical aspects have to be carefully studied for the DARTS system. These include the computational speed, software implementation and the algorithm stability in the continuous long-term run. To address these practical aspects, real-time dynamic simulations have been conducted using the data sets from the WSR-88D radar (Melbourne, FL) and the CASA IP1 network radar (OK).

The performance in terms of nowcasting scores such as CSI, POD and FAR has been comprehensively evaluated in above studies. Case studies using three data sets have shown that DARTS can compete with the state-of-the-art algorithm (GDST). The following case studies are focused on the performance evaluation in terms of the feasibility for real-time applications. This includes the software implementation of the spectral algorithm and the computational speed based on the implemented software.

a. *Software implementation of spectral tracking algorithm*

The spectral algorithm for storm motion based tracking and nowcasting has been implemented in a software library. The library has been designed and written in C. The

C language is chosen because of the portability consideration. The current software depends on two public-domain scientific libraries, namely, Fast Fourier Transform in the West (FFTW, Frigo and Johnson 2005) and GNU Scientific Library (GSL). FFTW interfaces are used performing the fast Fourier transform and the inverse fast Fourier Transform. GSL interfaces are used solving the linear system equations. The solver component is factored out by a solver interface which can be used to configure user's own inversion algorithm. The solver interface is designed in such a way that various algorithms may be used to solve linear system equations. This may help improve the bottleneck of the computational speed in the spectral algorithm.

The software implementation described above is applied to two sets of reflectivity data: the dataset from the WSR-88D radar (Melbourne, FL 1998) and the dataset from the CASA IP1 network radar (OK, 2006). The software for the DARTS system is tested on the Linux operating system, with a dual-processor computer of medium computational power. The performance measured in CPU clock time for each component in current software has been obtained below. Based on these results, the feasibility of real-time application of DARTS system is further analyzed and simulated in the next section.

b. *WSR-88D radar data (Melbourne, FL)*

The first test of DARTS system is conducted using the reflectivity data collected by the WSR-88D radar (Melbourne, FL) during the storm event from 2102 UTC 23 August to 0057 UTC 24 August, 1998. The WSR-88D radar takes approximately five minutes for each volume scan. Each volume of PPI scan is interpolated for generating the CAPPI data in Cartesian coordinates. The interpolated 2D radar images at the height of 1 km above the ground are used in this study. The re-sampled radar images are in the two-

dimensional region: -50 km $\leq x \leq 50$ km and -50 km $\leq y \leq 50$ km. The WSR-88D radar is located at the origin of Cartesian coordinates. The spatial sampling interval is 1 km on both x-axis and y-axis. The temporal sampling interval is 5 minutes. The spectral tracking algorithm is applied for each six consecutive radar images that span approximately twenty-five minutes. The estimated motion field is used to track and forecast next twelve reflectivity images. This gives us predicted images up to one hour. Each image size is 101×101 pixels. The CPU clock time for each component of DARTS system and total CPU time for each complete loop run are shown in Table 2.

Table 2. CPU time for the testing run of DARTs software on reflectivity data from the WSR-88D radar (Melbourne, FL 1998): time is averaged over 100 processing loops.

Component	CPU Time (Seconds)
3D FFT	0.037
System Construction	0.037
System Solver	6.302
System Retrieval	0.002
Inverse FFT (2D and 3D)	0.003
Tracking and 12-step Forecasting	5.016
One Complete Processing Loop	11.397

c. *CASA IP-1 radar network data (OK)*

The second test of DARTS system is conducted using the reflectivity data collected and merged from the four-radar network in the CASA IP1 project. The four radars of CASA IP1 are located at Chickasha (KSAO), Cyril (KCYR), Lawton (KLWE), and Rush Springs (KRSP) in Oklahoma. These are the X-band (3-cm) radars, each of which has a beam-width of 1.8 degree and a range of 30 km. The reflectivity has been corrected to compensate the path-integrated attenuation. The storm data spans approximately forty-eight minutes (00:10 UTC – 00:57 UTC, August 27 in 2006). Each

volume of PPI scans is interpolated for generating the CAPPI data in Cartesian coordinates. The interpolated 2D radar images at the height of 2.5 km above the ground are used in this study. The re-sampled radar images are in the two-dimensional region: -60 km $\leq x \leq$ 60 km and -*50* km $\leq y \leq$ 70 km. The coordinate origin is the center of the four CASA radars. The spatial sampling resolution is 0.5 km on both x-axis and y-axis. The temporal resolution is approximately 30 seconds. The spectral tracking algorithm is applied for each 25 consecutive radar images that span approximately 12.5 minutes. Each estimated motion field is used to track and forecast next ten reflectivity images. This gives us predicted radar images for five minutes. Each image size is 241×241 pixels. The CPU clock time for each component of DARTS system and total CPU time for each complete loop run are shown in Table 3.

Table 3. CPU time for the testing run of DARTs software on reflectivity data from the CASA IP1 radar network (OK 2006): time is averaged over 61 processing loops.

Component	CPU Time (Seconds)
3D FFT	0.225
System Construction	0.039
System Solver	3.699
System Retrieval	0.006
Inverse FFT (2D and 3D)	0.020
Tracking and 10-step Forecasting	17.360
One Complete Processing Loop	21.349

d. *Dynamic simulations and considerations on real-time implementation of DARTS system*

To further study the feasibility of the real-time application of DARTS system, the continuous radar scanning, data pre-processing and storm tracking and nowcasting are simulated. Two sets of reflectivity data from the CASA IP1 project (OK, 2006) are used in the simulations. The first dataset spans approximately twelve hours (00:00 UTC –

12:21 UTC, August 27th, 2006). The second dataset spans four hours and forty-four minutes (22:00 UTC, August 15th, 2006 – 02:44 UTC, August 16th, 2006). Because the data were collected by short-range (30 km) network radars, the data pre-processing includes synchronizing and merging volume scans as well as interpolating volume scans. The two-dimensional reflectivity images of 2.5 km height above the ground are used as the input to DARTS system. The reflectivity values are corrected to compensate the integral path attenuation. The spatial resolution is 0.5 km × 0.5 km. The temporal resolution is around 30 seconds. As shown in the previous section, the 10-step nowcast (5 minutes) in a single loop takes approximately 21 seconds. Therefore 5-step nowcast (2.5 minutes) is conducted by the DARTS system during each simulated radar volume scan. During each volume scan 25 most recent images are used for the motion estimation and tracking. For the two datasets that are chosen, some volumes are missing and these volume gaps are sporadic. This is handled according to the following strategy:

1) The DARTS tracking and nowcasting are turned on when the most recent 25 history images are all available, which span approximately 12.5 minutes.
2) When one of the five predicted reflectivity images is missing, the most recent nowcast image is used to make the missing image available.

Based on the above strategy the volume gaps of radar scanning could be completely filled once the DARTS system is turned on. However this strategy is proposed for handling sporadic volume gaps, since the tracking and nowcasting would be inaccurate if too many radar scans are missing in operations. An alternative strategy for handling the large volume gap is to set a criterion for the gap-filling ratio in the most recent 25 images,

and the DARTS system is turned off once the ratio is beyond the specified ratio. The above simple strategy is applied in current simulations.

The dynamic simulation consists of three major components: 1) radar scan sequence emulator; 2) data pre-processing system; and 3) DARTS tracking and nowcasting system. In the radar scanning emulator, a timer is used for continuously monitoring and depositing the reflectivity data. All the timing information has been pre-extracted from each radar volume to a precision of one second. All radar volume files are stored in the NetCDF (network Common Data Form) Format. When the volume scans from all radars in the network are ready, the volume data are synchronized, merged and interpolated to generate the two-dimensional image at 2.5 km height. The generated reflectivity images are also stored in the NetCDF files and a message is sent to invoke the DARTS system. The third component implements the user interface for the DARTS software library. The DARTS system computes the motion estimation for 5-step tracking and nowcasting. Then it waits for the next image input.

The simulations are run on a dual-processor computer of medium computational power. Using the two datasets described above, simulations for the radar scanning, the data pre-processing and the DARTS are successfully run over the whole periods that data spans. It is observed that the radar volume scanning interval ranges from 25 to 30 seconds or more, while the data pre-processing time ranges from 4 to 8 seconds and the DARTS nowcasting time ranges from 9 to 15 seconds. All loops for the 5-step tracking and nowcasting based on the DARTS system can be completed during the radar scanning intervals. These simulations are based on the high-resolution reflectivity data over more than sixteen hours. They demonstrate that the DARTS system can be implemented for

real-time operational applications. It is also shown that DARTS is a robust system for real-time applications. The examples of predicted images (2.5-minute) that are compared with the observed images are shown in Figs 23 and 24.

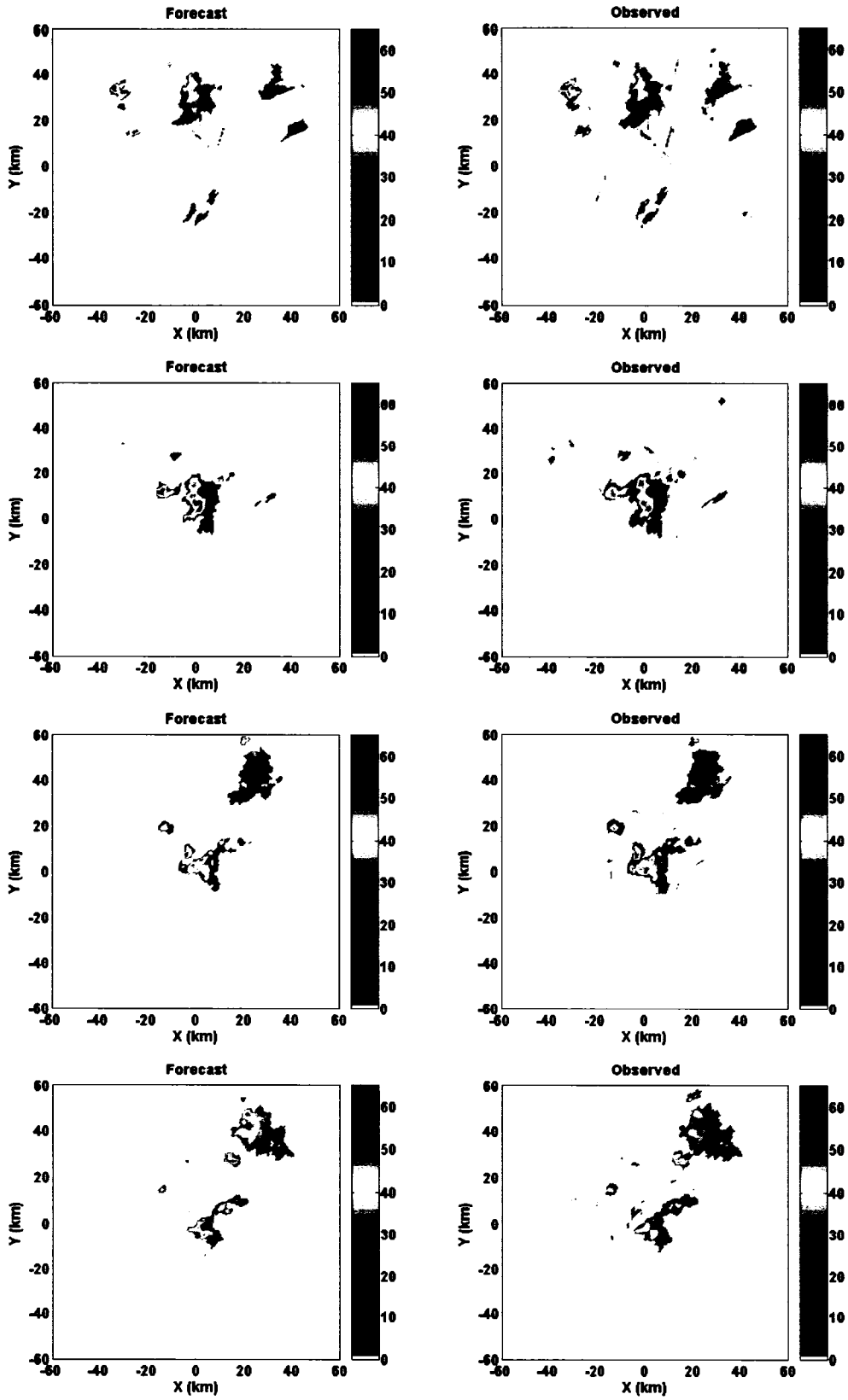

Figure 23. Examples of 5-step (2.5-minute) forecast images compared with the observed images in real-time simulations.

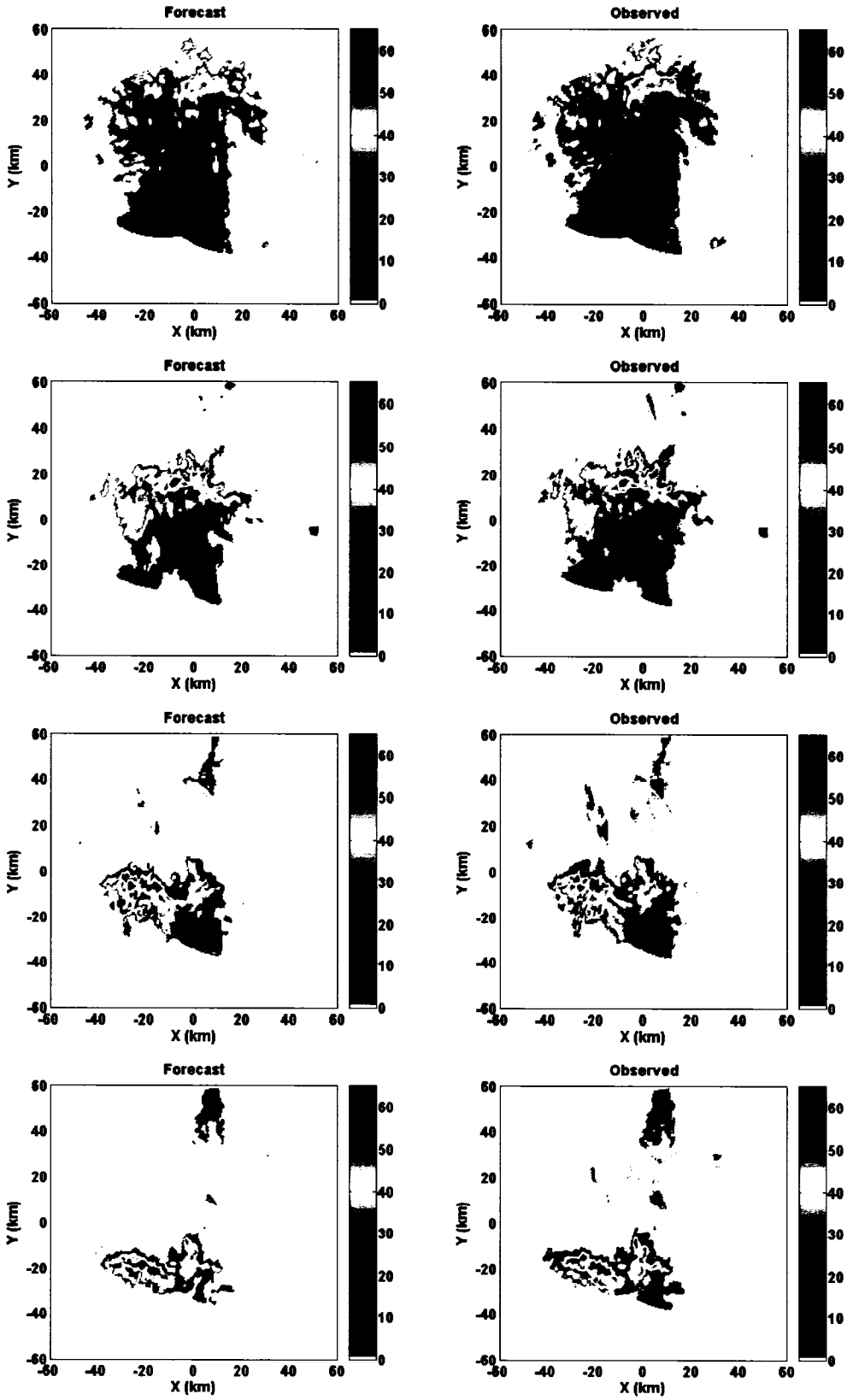

Figure 24. More examples of 5-step (2.5-minute) forecast images compared with the observed images in real-time simulations.

2.5. Summary and Discussion

A new spectral system for radar storm tracking and extrapolating is developed. The storm motion tracking algorithm, based on a modified spatiotemporal flow equation, is formulated and solved in the Fourier domain. Using simulations it is demonstrated that the spectral algorithm has the ability to mitigate the influence of local independent growth on the motion estimation. This implies that the spectral algorithm may improve the storm tracking in various complex weather systems. The scales of the storm tracking can be controlled by the choice of Fourier coefficients. A simple yet accurate and effective algorithm for extrapolating reflectivity fields has also been presented and assessed. It has demonstrated stable and excellent performance, while the computation is very efficient in applications.

New algorithms are then applied to nowcasting reflectivity fields up to one hour, using observed reflectivity from the WSR-88D radar (Melbourne, FL 1998) and the KOUN radar (Norman, OK 2003). They are also applied to nowcasting reflectivity fields for five minutes, using the high resolution data from the four-radar network in the CASA IP1 project (OK 2006). Nowcasting scores of the spectral tracking algorithm are compared with the GDST based algorithm. Using the high resolution data from the CASA IP1 network radars, the impact of space and time resolution on the nowcasting performance of both algorithms are also studied. The spectral tracking algorithm has demonstrated fairly good performance and it offers a new promising technique for the radar storm tracking and extrapolating.

CHAPTER III. SPACE-TIME MODELING OF RADAR OBSERVATIONS – THEORY

3.1. Overview

As discussed in chapter I, there exist several challenges when constructing the space-time model for radar observations: 1) *high dimensionality* resulting from the large data sets sampled over the extensive spatial domain in high resolution; 2) *non-stationarity* resulting from the storm motion and evolution; and 3) dynamic evolution of thunderstorms allowing the *non-stationary* growth or dissipation. The new algorithms, developed in chapter II, for radar storm tracking and extrapolating is focused on solving the second difficulty. The high dimensionality from high-resolution radar measurements extending a large area is a central issue in the spatial modeling. To generally account for the spatial variability, the kernel function based method developed in the statistical learning theory for modeling the mean component of radar measurements will be adopted. A vector representation for the spatial modeling is formulated based on finite kernel expansions. The linear dimension reduction to the vectors is conducted using the singular value decomposition (SVD) (Horn and Johnson 1999). The normalized coefficients by projecting the original vector into a low-dimensional subspace are interpreted as the state vector. To incorporate the temporal evolution, the state coefficients are allowed to change with time in a general functional form, which will be limited to the family of the linear transformation in the current research. Therefore a state-space modeling (SSM) framework based on linear dynamic systems (LDS) can be

formally constructed. The fundamental results for dynamic linear models with the Gaussian process will be briefly reviewed, where the formulation for the statistical filtering, predicting, and multiple-step forecasting will be summarized. The storm motion is a special application of the model developed here where the radar observational fields are modeled as an LDS over a short time of period. To further decompose the storm motion and the growth-decay evolution, the motion-compensated temporal alignment (MCTA) is formally developed and theoretical results are discussed.

3.2. Spatial Modeling – Representation

In this section a vector representation of the spatial model for the radar fields at a fixed time will be formulated. Because of the high resolution radar measurement over a large spatial domain, the vector consisting of all observational points gives a high-dimensional representation. The measurements at different spatial points are usually highly correlated and the direct vector representation in the high-dimensional space may be redundant. Further more, a general spatial representation that is flexible and may be adapted to accounting for different spatial correlations is desirable.

The mean process of the radar field, such as the reflectivity (dBZ), at the lowest elevation for a fixed time is modeled as a scalar function of the spatial coordinate variables. Let $\mathbf{x} \equiv (x, y)$ be the vector in the two-dimensional coordinate space, and $f_t(\mathbf{x})$ be a function, such as reflectivity field or rainfall-rate field in that space at a fixed time t. In general $f_t(\mathbf{x})$ is a non-linear function of the location, $\mathbf{x}$. Based on the kernel-functional expansion that was developed in the statistical learning theory (Vapnik 1995; Cristianini and Shawe-Taylor 2000), the radar measurement field, $f_t(\mathbf{x})$, at location $\mathbf{x}$ and the fixed time t can be written as

$$f_t(\mathbf{x}) = \sum_{j=1}^{J} K_t(\mathbf{x}, \mathbf{c}_j)\beta_t(j) + \varepsilon_t(\mathbf{x}) \tag{3.1}$$

where $K_t(\mathbf{x}, \mathbf{c}_j)$ is the j^{th} kernel function at time t, and $\mathbf{c}_j$ is the j^{th} kernel center that is in the same coordinate space as $\mathbf{x}$. $\beta_t(j)$ is the j^{th} expansion coefficient and J is the number of kernels, which is equal to or less than the number of observations. $\varepsilon_t(\mathbf{x})$ is assumed to be a white Gaussian noise process. The theory underpinning this "kernel" technique states in brief that, the decision or regression rule can be evaluated using inner products of the testing point and the training points, both of which are implicitly mapped into a nonlinear feature space. However, the underlying feature map is not explicitly needed as long as we can compute the inner product in the feature space. Such a direct evaluation of the inner product is called the *kernel* function (Cristianini and Shawe-Taylor 2000). A *kernel* function is defined as follows.

Definition 3.1 A *kernel* is a function K, such that for all $\mathbf{x}, \mathbf{c} \in \mathrm{X}$

$$K(\mathbf{x}, \mathbf{c}) \equiv \langle \phi(\mathbf{x}), \phi(\mathbf{c}) \rangle \tag{3.2}$$

where ϕ is a mapping from the inner product space X to a feature (inner product) space F. In the meantime the "kernel" based function expansion states that the intermediate non-linear map ϕ is not explicitly needed, as long as the *kernel* function can be explicitly computed. The sufficient conditions for a continuous symmetric function $K(\mathbf{x}, \mathbf{c})$ to be a kernel are given by Mercer's theorem (Cristianini and Shawe-Taylor 2000). The detailed discussion for the fundamentals of the kernel based technique can be found in Cristianini and Shawe-Taylor (2000), Cucker and Smale (2001), and Poggio and Smale (2003). Eq 3.1 can be understood by looking into two special kernels: 1) if we let $K_t(\mathbf{x}, \mathbf{c}_j)$ be a *SINC*-kernel in one-dimensional coordinate space, Eq 3.1 is reduced to the

form of the conventional sampling theorem, and $\beta_t(j)$ is the sampled functional value at point j (Oppenheim and Schafer, 1989); or 2) if we let $K_t(\mathbf{x},\mathbf{c}_j)$ be a *GAUSS*-kernel in the coordinate space, Eq 3.1 is reduced to the RBF neural network for the function approximation, and $\beta_t(j)$ is the j^{th} weight coefficient (Haykin 1999). In the first special case of *SINC* kernels, the number of kernels is equal to the number of observations and each observation is taken at the center of a *SINC*-kernel. In the case of Gaussian RBF network, the kernels have to be appropriately determined and the number of kernels is equal to or less than the number of observations. For the RBF neural network, weight coefficient $\beta_t(j)$ in Eq 3.1 does not have an explicit observational interpretation.

Applying Eq 3.1 to a set of observations at different locations $\mathbf{x}_i$ ($i = 1, 2, \cdots, n$) for a fixed time t,

$$f_t(\mathbf{x}_i) = \sum_{j=1}^{J} K_t(\mathbf{x}_i, \mathbf{c}_j)\beta_t(j) + \varepsilon_t(\mathbf{x}_i) \tag{3.3}$$

Therefore the observation equation for a radar measurement at the fixed time t admits a vector representation as implied by Eq 3.3, namely,

$$\vec{\mathbf{f}}_t = \mathbf{\Phi}_t \vec{\mathbf{b}}_t + \vec{\mathbf{e}}_t \tag{3.4}$$

where

$$\vec{\mathbf{f}}_t \equiv [f_t(\mathbf{x}_1),\ f_t(\mathbf{x}_2),\ \cdots,\ f_t(\mathbf{x}_i),\ \cdots,\ f_t(\mathbf{x}_n)]^{\mathbf{T}} \tag{3.5}$$

$$\mathbf{\Phi}_t \equiv \begin{bmatrix} K_t(\mathbf{x}_1,\mathbf{c}_1) & \cdots & K_t(\mathbf{x}_1,\mathbf{c}_J) \\ \cdots & \cdots & \cdots \\ K_t(\mathbf{x}_n,\mathbf{c}_1) & \cdots & K_t(\mathbf{x}_n,\mathbf{c}_J) \end{bmatrix} \tag{3.6}$$

$$\vec{\mathbf{b}}_t \equiv [\beta_t(1),\ \beta_t(2),\ \cdots,\ \beta_t(j),\ \cdots,\ \beta_t(J)]^{\mathbf{T}} \tag{3.7}$$

$$\vec{\mathbf{e}}_t \equiv [\varepsilon_t(\mathbf{x}_1),\ \varepsilon_t(\mathbf{x}_2),\ \cdots,\ \varepsilon_t(\mathbf{x}_i),\ \cdots,\ \varepsilon_t(\mathbf{x}_n)]^{\mathrm{T}} \tag{3.8}$$

Vector $\vec{\mathbf{b}}_t$ in Eq 3.7 is called the *vector representation* of the spatial model. Depending on the type of kernels, the definition of observation vector $\vec{\mathbf{f}}_t$ and the procedure for fitting the spatial model, $\vec{\mathbf{b}}_t$ may or may not be a dimension-reduced representation.

It would be desirable to incorporate multiple vector representations, e.g., multiple steps of one radar field and multiple radar fields, into a single model. This can be achieved by first combining the vectors of multiple steps for one radar field, such as reflectivity (Z in dBZ) into a single vector. Specifically, by concatenating a set of time-delayed vectors $\{\vec{\mathbf{b}}_{t+m-1},\ m=1,\ \cdots,\ M\}$ for a single radar field m', we define that

$$\vec{\mathbf{r}}_{t,m'} \equiv [\vec{\mathbf{b}}_t^{\mathrm{T}},\ \cdots,\ \vec{\mathbf{b}}_{t+m-1}^{\mathrm{T}},\ \cdots,\ \vec{\mathbf{b}}_{t+M-1}^{\mathrm{T}}]^{\mathrm{T}} = \oplus_{m=1}^{M} \vec{\mathbf{b}}_{t+m-1} \tag{3.9}$$

where subscript t is the discrete-time index, subscript m' is the index for the radar field, superscript "T" denotes the transpose of vector, and $\vec{\mathbf{b}}_t$ is defined in Eq 3.7. The concatenation of vector spaces is denoted by the direct sum, $\oplus$. It should also be noted that the definition of $\vec{\mathbf{r}}_{t,m'}$ in Eq 3.9 is just for a single radar field, such as the reflectivity ($m' = Z$).

Example: let $\vec{\mathbf{f}}_t$ in Eq 3.4 be a set of reflectivity (Z) observations at 10 different locations $\mathbf{x}_i$ ($i = 1,\ 2,\ \cdots,\ 10$) and time t,

$$\vec{\mathbf{f}}_t \equiv [Z_t(\mathbf{x}_1),\ Z_t(\mathbf{x}_2),\ \cdots,\ Z_t(\mathbf{x}_{10})]^{\mathrm{T}} \tag{3.10}$$

and assume that the spatial variability is modeled using 2 kernels. For the purpose of discussion here, the type of kernels in the model is not relevant. Therefore they are not specified. The vector representation $\vec{\mathbf{b}}_t$ is then given by

$$\vec{\mathbf{b}}_t \equiv [\beta_t(1),\ \beta_t(2)]^{\mathbf{T}} \tag{3.11}$$

Similarly, for the one-step delay at $t+1$, we have

$$\vec{\mathbf{f}}_{t+1} \equiv [Z_{t+1}(\mathbf{x}_1),\ Z_{t+1}(\mathbf{x}_2),\ \cdots,\ Z_{t+1}(\mathbf{x}_{10})]^{\mathbf{T}} \tag{3.12}$$

and

$$\vec{\mathbf{b}}_{t+1} \equiv [\beta_{t+1}(1),\ \beta_{t+1}(2)]^{\mathbf{T}} \tag{3.13}$$

The correlations between $\beta_t(1)$ and $\beta_t(2)$, or between $\beta_{t+1}(1)$ and $\beta_{t+1}(2)$, have encoded the spatial correlations at a fixed time (t or $t+1$). To account for the temporal correlations in one-step delay as well as the spatial correlations, we need to encode the correlations among all above four components, namely, $\beta_t(1)$, $\beta_t(2)$, $\beta_{t+1}(1)$ and $\beta_{t+1}(2)$. Therefore $\vec{\mathbf{b}}_t$ and $\vec{\mathbf{b}}_{t+1}$ are concatenated to form a more general vector representation:

$$\vec{\mathbf{r}}_{t,Z} \equiv [\vec{\mathbf{b}}_t^{\mathbf{T}}, \vec{\mathbf{b}}_{t+1}^{\mathbf{T}}]^{\mathbf{T}} = [\beta_t(1),\ \beta_t(2),\ \beta_{t+1}(1),\ \beta_{t+1}(2)]^{\mathbf{T}} \tag{3.14}$$

In this example the concatenated vector $\vec{\mathbf{r}}_{t,Z}$ is for the reflectivity field from t to $t+1$, where the number of reflectivity observations $n = 10$, the number of kernels $J = 2$ and the number of delayed vectors $M = 2$.

Secondly, to account for the correlations among different radar fields, such as reflectivity (Z) and other fields, a set of $\vec{\mathbf{r}}_{t,m'}$ ($m' = Z,\ \cdots,\ M'$) for different radar fields can be concatenated to form a generalized vector

$$\vec{\mathbf{r}}_t \equiv [\vec{\mathbf{r}}_{t,Z}^{\mathrm{T}}, \cdots, \vec{\mathbf{r}}_{t,m'}^{\mathrm{T}}, \cdots, \vec{\mathbf{r}}_{t,M'}^{\mathrm{T}}]^{\mathrm{T}} \tag{3.15}$$

where $\vec{\mathbf{r}}_{t,m'}$ is defined in Eq 3.9, as discussed above. For the sake of convenience and without the loss of clarity, M' denotes both the last radar field and the number of different radar fields. The vector $\vec{\mathbf{r}}_t$ defined in Eq 3.15 is called the *generalized vector representation*. When M' is for only a single radar field, such as reflectivity Z (dBZ), the definition of $\vec{\mathbf{r}}_t$ (Eq 3.15) is then reduced to $\vec{\mathbf{r}}_{t,m'}$ (Eq 3.9).

In general the concatenated vector representation is a high-dimensional vector, where there may exist high redundancy due to the correlation among its elements. The singular value decomposition (SVD) is used to obtain the low-dimensional representation for the system. Let q be the dimension of the generalized vector representation $\vec{\mathbf{r}}_t$, then q is given by

$$q = J \times M \times M' \tag{3.16}$$

where J is the number of kernels, M is the number of time delays and M' is the number of radar fields. Let $\{\vec{\mathbf{r}}_t \in \mathbf{R}^q,\ t = 1, \cdots, p\}$ be a set of *generalized vector representations* (Eq 3.15) at different time, which are obtained from a short sequence of radar observations. Let p be the number of time vectors in the sequence, which is currently usually far less than the dimension of the vector space, i.e., $p << q$. We may perform the SVD in the following way.

Let $\vec{\mathbf{r}}_0$ be a given constant vector, such as the mean vector defined by

$$\vec{\mathbf{r}}_0 \equiv \frac{1}{p}\sum_{t=1}^{p} \vec{\mathbf{r}}_t \tag{3.17}$$

where the generalized vector representation $\vec{\mathbf{r}}_t$ is defined in Eq 3.15.

Firstly, we subtract $\vec{\mathbf{r}}_0$ from each $\vec{\mathbf{r}}_t$, and define the data vector $\vec{\mathbf{d}}_t$ by

$$\vec{\mathbf{d}}_t \equiv \vec{\mathbf{r}}_t - \vec{\mathbf{r}}_0 \quad (t = 1, \cdots, p) \tag{3.18}$$

Secondly, a $q \times p$ data matrix $\mathbf{D}$ is constructed such that $\mathbf{D}$ has each vector $\vec{\mathbf{d}}_t$ as its column, namely,

$$\mathbf{D} \equiv [\vec{\mathbf{d}}_1, \cdots, \vec{\mathbf{d}}_t, \cdots, \vec{\mathbf{d}}_p] \tag{3.19}$$

Thirdly, the SVD of matrix $\mathbf{D}$ (Horn and Johnson 1999) is given by

$$\mathbf{D} = \mathbf{U}\mathbf{S}\mathbf{V}^{\mathbf{T}} \tag{3.20}$$

where $\mathbf{U} \in \mathbf{R}^{q \times q}$, $\mathbf{S} \in \mathbf{R}^{q \times p}$, $\mathbf{V} \in \mathbf{R}^{p \times p}$ for the full-sized SVD;

or $\mathbf{U} \in \mathbf{R}^{q \times p}$, $\mathbf{S} \in \mathbf{R}^{p \times p}$, $\mathbf{V} \in \mathbf{R}^{p \times p}$ for the economical-sized SVD.

In the current research the economical-sized SVD will be used, for which the fast and efficient computational algorithm exists. Following the standard SVD method (Horn and Johnson 1999), the matrix that projects the data vector $\vec{\mathbf{d}}_t$ into the optimal subspace followed by the normalization is given by

$$\mathbf{P}_{\mathbf{S}} \equiv \mathbf{S}^{-1}\mathbf{U}^{\mathbf{T}} \tag{3.21}$$

where $\mathbf{S}$ is a diagonal square matrix, whose diagonal elements consist of the singular values in decreasing order. This is understood by noticing the relation

$$\mathbf{V}^{\mathbf{T}} = \mathbf{P}_{\mathbf{S}}\mathbf{D} \tag{3.22}$$

Let vector $\vec{\boldsymbol{\theta}}_t$ $(t = 1, \cdots, p)$ be each column in matrix $\mathbf{V}^{\mathbf{T}}$, i.e.,

$$\mathbf{V}^{\mathbf{T}} = [\vec{\boldsymbol{\theta}}_1, \cdots, \vec{\boldsymbol{\theta}}_t, \cdots, \vec{\boldsymbol{\theta}}_p] \tag{3.23}$$

Then Eq 3.22 implies that each column vector $\vec{\boldsymbol{\theta}}_t$ in matrix $\mathbf{V}^{\mathbf{T}}$ is interpreted as $\vec{\mathbf{d}}_t$'s subspace projection that is normalized by the singular values. Therefore vector $\vec{\boldsymbol{\theta}}$ is a

normalized low-dimensional representation for the vector $\vec{\mathbf{d}}_t$. This subspace representation is known to be optimal in the least square sense for all given data vectors ($\vec{\mathbf{d}}_t$). Regardless of its optimality for representing the given history data, the subspace may not be complete for representing the future or unobserved data. Therefore we should be cautious when interpreting the prediction based on this subspace representation.

3.3. Temporal Modeling – Dynamics

The dynamic model for temporal evolution is constructed by allowing the low-dimensional vector, $\vec{\theta}$, to change with time. This is achieved by specifying a probability model $P(\vec{\theta}_{t+1} | \vec{\theta}_t)$ to link low-dimensional vectors over time. The temporal model can be written by

$$\vec{\theta}_{t+1} = \vec{\mathbf{f}}(\vec{\theta}_t) + \vec{\eta}_t \tag{3.24}$$

where $\vec{\mathbf{f}}(\cdot)$ is the deterministic dynamic mapping in a general functional form and $\vec{\eta}_t$ is a stochastic noise process. For linear systems, $\vec{\mathbf{f}}(\cdot)$ is a transition matrix to transform the current vector to the next vector, namely,

$$\vec{\theta}_{t+1} = \mathbf{F}_t \vec{\theta}_t + \vec{\eta}_t \tag{3.25}$$

where $\mathbf{F}_t$ is assumed to be a reversible dynamic mapping, i.e., $\mathbf{F}_t^{-1}$ exists (Ljung 1998). $\vec{\eta}_t$ is assumed to be a zero-mean white Gaussian process.

3.4. State Space Modeling – Space-Time Model

a. *Linear Gaussian state-space model*

In the conventional mathematical notations for the state-space model (SSM), the observation vector is denoted by $\vec{\mathbf{y}}_t$ and the state vector is denoted by $\vec{\mathbf{x}}_t$. However, to

avoid recycling the mathematical notations that may cause confusions here, the notations different from the conventional ones are adopted in the following discussion. Let $\vec{\mathbf{z}}_t$ be the observation vector and $\vec{\boldsymbol{\theta}}_t$ be the state vector. The linear Gaussian SSM takes the form (Brockwell and Davis 1991 & 1996; West and Harrison 1997)

$$\vec{\mathbf{z}}_t = \mathbf{G}_t \vec{\boldsymbol{\theta}}_t + \vec{\boldsymbol{\varepsilon}}_t \qquad \vec{\boldsymbol{\varepsilon}}_t \sim N(0,\ \mathbf{R}_t) \tag{3.26}$$

$$\vec{\boldsymbol{\theta}}_{t+1} = \mathbf{F}_t \vec{\boldsymbol{\theta}}_t + \vec{\boldsymbol{\eta}}_t \qquad \vec{\boldsymbol{\eta}}_t \sim N(0,\ \mathbf{Q}_t) \tag{3.27}$$

where $t \geq 1$, $\vec{\boldsymbol{\varepsilon}}_t$ is a zero-mean white Gaussian process with covariance matrix $\mathbf{R}_t$, $\vec{\boldsymbol{\eta}}_t$ is a zero-mean white Gaussian process with covariance matrix $\mathbf{Q}_t$, and $\vec{\boldsymbol{\varepsilon}}_t$ and $\vec{\boldsymbol{\eta}}_t$ are independent to each other:

$$E(\vec{\boldsymbol{\varepsilon}}_t) = 0,\ E(\vec{\boldsymbol{\eta}}_t) = 0; \tag{3.28}$$

$$E(\vec{\boldsymbol{\varepsilon}}_t \vec{\boldsymbol{\varepsilon}}_t^{\mathrm{T}}) = \mathbf{R}_t,\ E(\vec{\boldsymbol{\eta}}_t \vec{\boldsymbol{\eta}}_t^{\mathrm{T}}) = \mathbf{Q}_t,\ E(\vec{\boldsymbol{\eta}}_t \vec{\boldsymbol{\varepsilon}}_t^{\mathrm{T}}) = \mathbf{0}. \tag{3.29}$$

where $E(\cdot)$ denotes the expectation operation. The observation equation (3.26) relates the data vector $\vec{\mathbf{z}}_t$ to the unobserved state vector $\vec{\boldsymbol{\theta}}_t$. The state equation (3.27) links the state vectors over time via the linear dynamic mapping. $\mathbf{F}_t$ and $\mathbf{G}_t$ are known as the evolution and observation matrices, respectively. The model is completed by specifying the initial condition for the state vector, $P(\vec{\boldsymbol{\theta}}_1) \sim N(\vec{\boldsymbol{\theta}}_1;\ E\vec{\boldsymbol{\theta}}_1,\ \boldsymbol{\Omega}_1)$. The Kalman filtering (Kalman 1960) and the solutions for the linear Gaussian SSM are reviewed in the Appendix C. These are standard results and can be found in textbooks and literature (Brockwell and Davis 1991 & 1996; West and Harrison 1997).

Example: let $\vec{\mathbf{f}}_t$ in Eq 3.4 be a set of reflectivity (Z) observations at 10 different locations $\mathbf{x}_i$ ($i = 1, 2, \cdots, 10$) and time t, and let these observations are sampled at 5 different time steps ($t = 1, \cdots, 5$),

$$\vec{\mathbf{f}}_t \equiv [Z_t(\mathbf{x}_1),\ Z_t(\mathbf{x}_2),\ \cdots,\ Z_t(\mathbf{x}_{10})]^{\mathrm{T}} \qquad (t = 1, \cdots, 5) \tag{3.30}$$

Assuming that the spatial variability is modeled using the *SINC* kernel, it gives the vector representation $\vec{\mathbf{b}}_t = \vec{\mathbf{f}}_t$ ($t = 1, \cdots, 5$). For the sake of simplicity, by taking no time-delay and using only the reflectivity field (Z) in the model, we have $\vec{\mathbf{r}}_t = \vec{\mathbf{r}}_{t,Z} = \vec{\mathbf{b}}_t$ ($t = 1, \cdots, 5$) (see Eqs 3.9 and 3.15). Let the constant vector $\vec{\mathbf{r}}_0 = \mathbf{0}$, therefore the data vector $\vec{\mathbf{d}}_t = \vec{\mathbf{r}}_t$ (Eq 3.18). From these chaining relations, we therefore have that

$$\begin{aligned} \mathbf{D} &\equiv [\vec{\mathbf{d}}_1,\ \vec{\mathbf{d}}_2,\ \vec{\mathbf{d}}_3,\ \vec{\mathbf{d}}_4,\ \vec{\mathbf{d}}_5] \\ &= [\vec{\mathbf{f}}_1,\ \vec{\mathbf{f}}_2,\ \vec{\mathbf{f}}_3,\ \vec{\mathbf{f}}_4,\ \vec{\mathbf{f}}_5] \end{aligned} \tag{3.31}$$

Further applying Eqs 3.20 and 3.23, it gives that

$$\vec{\mathbf{f}}_t = \mathbf{US}\vec{\boldsymbol{\theta}}_t \qquad (t = 1, \cdots, 5) \tag{3.32}$$

where $\vec{\mathbf{f}}_t \equiv [Z_t(\mathbf{x}_1),\ Z_t(\mathbf{x}_2),\ \cdots,\ Z_t(\mathbf{x}_{10})]^{\mathrm{T}}$ gives observation vector $\vec{\mathbf{z}}_t$, and **US** gives observation matrix $\mathbf{G}_t$ in Eq 3.26. $\vec{\boldsymbol{\theta}}_t$ and $\vec{\boldsymbol{\theta}}_{t+1}$ are linked by the dynamic map $\mathbf{F}_t$, which is to be estimated (Eq 3.27).

b. *A general framework*

It is seen that the temporal modeling, Eq 3.25, is directly cast to the state evolution equation (3.27) in SSM. For the spatial modeling, the vector representation and the SVD given above can be cast to the observation equation (3.26). This is shown as follows.

From Eqs 3.18, 3.19, 3.20 and 3.23, we have

$$\vec{\mathbf{r}}_t - \vec{\mathbf{r}}_0 = \mathbf{U}\mathbf{S}\vec{\theta}_t \tag{3.33}$$

where $\vec{\mathbf{r}}_t$ is defined in Eq 3.15 by concatenating a set of delayed vectors $\{\vec{\mathbf{b}}_{t+m-1},\ m = 1,\ \cdots,\ M\}$ for a single radar field, such as reflectivity Z. From Eqs 3.9 and 3.15, we have

$$\vec{\mathbf{r}}_t \equiv [\vec{\mathbf{r}}_{t,Zh}] = \oplus_{m=1}^{M} \vec{\mathbf{b}}_{t+m-1} \tag{3.34}$$

From Eq 3.4 and the above equation, we obtain that,

$$\oplus_{m=1}^{M} \vec{\mathbf{f}}_{t+m-1} = [\oplus_{m=1}^{M} \mathbf{\Phi}_{t+m-1}]\vec{\mathbf{r}}_t + \oplus_{m=1}^{M} \vec{\mathbf{e}}_{t+m-1} \tag{3.35}$$

Multiplying Eq 3.33 by $\oplus_{m=1}^{M} \mathbf{\Phi}_{t+m-1}$ from the left and adding to Eq 3.35 gives

$$\vec{\mathbf{z}}_t = \mathbf{G}_t\vec{\theta}_t + \vec{\varepsilon}_t \tag{3.36}$$

where $\vec{\mathbf{z}}_t$ is the observation vector given by

$$\vec{\mathbf{z}}_t = \oplus_{m=1}^{M} \vec{\mathbf{f}}_{t+m-1} - [\oplus_{m=1}^{M} \mathbf{\Phi}_{t+m-1}]\vec{\mathbf{r}}_0 \tag{3.37}$$

$\vec{\mathbf{f}}_t$ and $\mathbf{\Phi}_t$ are defined in Eq 3.5 and Eq 3.6, respectively. $\mathbf{G}_t$ and $\vec{\varepsilon}_t$ are given by

$$\mathbf{G}_t = [\oplus_{m=1}^{M} \mathbf{\Phi}_{t+m-1}]\mathbf{U}\mathbf{S} \tag{3.38}$$

$$\vec{\varepsilon}_t = \oplus_{m=1}^{M} \vec{\mathbf{e}}_{t+m-1} \tag{3.39}$$

For $\vec{\mathbf{r}}_t$ defined by combining more than one radar fields, such as reflectivity, differential reflectivity and others (Eq 3.15), similar derivations can be shown. Therefore the spatial modeling in Eq 3.36 can be cast to the observation equation (3.26) in the linear Gaussian SSM.

3.5. Motion as Linear Transformation

The storm motion is a special application of the linear SSM developed above. The motion can be modeled as a linear flow matrix in the sub-state-space. Theoretical

properties of the motion flow matrix and the discrete map matrix will be discussed. Empirical structural characteristics of motion flow matrices are shown. Theoretical properties of motion flow matrices are verified using the observed reflectivity data.

a. *Motion in sub-state-space model*

We start from the motion flow equation

$$\frac{\partial}{\partial t} f_t(\mathbf{x}) = -u_t(\mathbf{x}) \frac{\partial}{\partial x} f_t(\mathbf{x}) - v_t(\mathbf{x}) \frac{\partial}{\partial y} f_t(\mathbf{x}) \tag{3.40}$$

where $\mathbf{x} \equiv (x, y)$ is the coordinates on the two-dimensional plane. $u_t(\mathbf{x})$ and $v_t(\mathbf{x})$ are the x- and y-direction velocity fields, respectively. $f_t(\mathbf{x})$ is the spatiotemporal radar measurement field. Substituting the kernel-based expansion (Eq 3.3) into the right hand side (RHS) of Eq 3.40, and dropping off the random noise term, we obtain (for $\mathbf{x} = \mathbf{x}_i$, $i = 1, \cdots, n$)

$$\frac{\partial}{\partial t} f_t(\mathbf{x}_i) = \sum_{j=1}^{J} A_{ij,t} \beta_t(j) \tag{3.41}$$

where

$$A_{ij,t} \equiv -u_t(\mathbf{x}_i) K'_{x_i,j} - v_t(\mathbf{x}_i) K'_{y_i,j} \tag{3.42}$$

$$K'_{x_i,j} \equiv \frac{\partial}{\partial x} K_t(\mathbf{x}, \mathbf{c}_j)\Big|_{\mathbf{x}=\mathbf{x}_i} \tag{3.43}$$

$$K'_{y_i,j} \equiv \frac{\partial}{\partial y} K_t(\mathbf{x}, \mathbf{c}_j)\Big|_{\mathbf{x}=\mathbf{x}_i} \tag{3.44}$$

To obtain an explicit expression for the observation vector on the left hand side (LHS) of the above equation, i.e., $[f_t(\mathbf{x}_1), \cdots, f_t(\mathbf{x}_i), \cdots, f_t(\mathbf{x}_n)]^{\mathrm{T}}$, we adopt the *SINC-*

kernel function. We assume time-independent *SINC*-kernels and uniform samples, namely,

$$\begin{aligned} K_t(\mathbf{x}_i,\mathbf{c}_j) \equiv K(\mathbf{x}_i,\mathbf{c}_j) &\equiv SINC\left(\frac{x_i}{\Delta_x}-m_j\right)SINC\left(\frac{y_i}{\Delta_y}-n_j\right) \\ &= SINC(m_i-m_j)SINC(n_i-n_j)=\delta_{ij} \end{aligned} \tag{3.45}$$

where the observation locations are defined by $\mathbf{x}_i \equiv (m_i\Delta_x,\ n_i\Delta_y)$ $(i=1,\cdots,n)$ and the kernel centers are defined by $\mathbf{c}_j \equiv (m_j\Delta_x,\ n_j\Delta_y)=\mathbf{x}_j$ $(j=1,\cdots,J)$. In this case, the number of observations is equal to the number of *SINC*-kernels, namely, $n=J$.

It is therefore straightforward to show that

$$\frac{\partial}{\partial t}\vec{\mathbf{b}}_t = \mathbf{A}_t\vec{\mathbf{b}}_t \tag{3.46}$$

The element of the flow matrix $\mathbf{A}_t$ is defined in Eq 3.42, and the vector representation $\vec{\mathbf{b}}_t$ is defined in Eq 3.7.

As a special case, let $\vec{\mathbf{r}}_t \equiv \vec{\mathbf{b}}_t$ and $\vec{\mathbf{r}}_0 \equiv \mathbf{0}$. So we have (see Eq 3.18)

$$\vec{\mathbf{d}}_t \equiv \vec{\mathbf{r}}_t - \vec{\mathbf{r}}_0 = \vec{\mathbf{b}}_t \tag{3.47}$$

Applying the projection matrix (Eq 3.21) to Eq 3.46, from the above relationship and the SVD (Eqs 3.19, 3.20 and 3.23), we get

$$\begin{aligned} &\frac{\partial}{\partial t}(\mathbf{S}^{-1}\mathbf{U}^{\mathrm{T}})\vec{\mathbf{b}}_t = (\mathbf{S}^{-1}\mathbf{U}^{\mathrm{T}})\mathbf{A}_t\vec{\mathbf{b}}_t \\ &\Rightarrow \frac{\partial}{\partial t}(\mathbf{S}^{-1}\mathbf{U}^{\mathrm{T}})\vec{\mathbf{d}}_t = (\mathbf{S}^{-1}\mathbf{U}^{\mathrm{T}})\mathbf{A}_t\vec{\mathbf{d}}_t \\ &\Rightarrow \frac{\partial}{\partial t}(\mathbf{S}^{-1}\mathbf{U}^{\mathrm{T}})(\mathbf{US})\vec{\boldsymbol{\theta}}_t = (\mathbf{S}^{-1}\mathbf{U}^{\mathrm{T}})\mathbf{A}_t(\mathbf{US})\vec{\boldsymbol{\theta}}_t \\ &\Rightarrow \frac{\partial}{\partial t}\vec{\boldsymbol{\theta}}_t = (\mathbf{S}^{-1}\mathbf{U}^{\mathrm{T}})\mathbf{A}_t(\mathbf{US})\vec{\boldsymbol{\theta}}_t \end{aligned} \tag{3.48}$$

Therefore the final form of motion equation in the low-dimensional state space is given by

$$\frac{\partial}{\partial t}\vec{\theta}_t = \mathbf{A}_t^P\vec{\theta}_t \tag{3.49}$$

$$\mathbf{A}_t^P \equiv (\mathbf{S}^{-1}\mathbf{U}^T)\mathbf{A}_t(\mathbf{US}) \tag{3.50}$$

Equations 3.49 and 3.50 show that, the motion can be written as a flow matrix in the sub-state-space representation and the mean process is a continuous LDS.

b. *Motion as a skew-symmetric flow matrix*

Motion can be considered as a conservational process for the entire system, since it only transfers the "mass" from one location to another location without generating or absorbing the transferred "mass". Based on this physical intuition, the state vector's norm $\vec{\theta}_t^T\vec{\theta}_t$ is assumed to be a conservation function with respect to time, namely,

$$\frac{\partial}{\partial t}\left(\vec{\theta}_t^T\vec{\theta}_t\right) = 0 \qquad (\forall\vec{\theta}_t) \tag{3.51}$$

This is an assumption and it results in several theoretical consequences that will be verified using observational reflectivity data in following studies.

From Equations 3.49 and 3.51, it can be easily shown that

$$\begin{aligned}
&\frac{\partial}{\partial t}\left(\vec{\theta}_t^T\vec{\theta}_t\right) = 0 \\
&\Rightarrow \vec{\theta}_t^T\left(\frac{\partial}{\partial t}\vec{\theta}_t\right) + \left(\frac{\partial}{\partial t}\vec{\theta}_t^T\right)\vec{\theta}_t = 0 \\
&\Rightarrow \vec{\theta}_t^T\left(\mathbf{A}_t^P + \mathbf{A}_t^{PT}\right)\vec{\theta}_t = 0 \qquad (\forall\vec{\theta}_t) \\
&\Rightarrow \mathbf{A}_t^P + \mathbf{A}_t^{PT} = 0
\end{aligned} \tag{3.52}$$

Therefore the motion is represented by a skew-symmetric flow-matrix:

$$\mathbf{A}_t^P = -\mathbf{A}_t^{PT} \text{ (or } \mathbf{A}_t = -\mathbf{A}_t^T) \tag{3.53}$$

For a discrete-time linear dynamic map with state vector's norm conserved, namely,

$$\vec{\theta}_{t+1} = \mathbf{F}_t \vec{\theta}_t \tag{3.54}$$

$$\vec{\theta}_{t+1}^T \vec{\theta}_{t+1} = \vec{\theta}_t^T \vec{\theta}_t \qquad (\forall \vec{\theta}_t, \vec{\theta}_{t+1}) \tag{3.55}$$

The dynamic mapping matrix $\mathbf{F}_t$ is an orthogonal matrix. This can be easily shown as follows.

Substituting Eq 3.54 into the LHS of Eq 3.55, we obtain that:

$$\vec{\theta}_t^T (\mathbf{F}_t^T \mathbf{F}_t - \mathbf{I}) \vec{\theta}_t = 0 \qquad (\forall \vec{\theta}_t) \tag{3.56}$$

where $\mathbf{I}$ is the identity matrix. Therefore,

$$\mathbf{F}_t^T \mathbf{F}_t = \mathbf{I} \tag{3.57}$$

Multiplying Eq 3.54 by $\mathbf{F}_t^T$ from the left and using Eq 3.57, we get

$$\mathbf{F}_t^T \vec{\theta}_{t+1} = \vec{\theta}_t \tag{3.58}$$

Substituting this result into the RHS of Eq 3.55, we obtain that:

$$\vec{\theta}_{t+1}^T (\mathbf{I} - \mathbf{F}_t \mathbf{F}_t^T) \vec{\theta}_{t+1} = 0 \qquad (\forall \vec{\theta}_{t+1}) \tag{3.59}$$

Therefore,

$$\mathbf{F}_t \mathbf{F}_t^T = \mathbf{I} \tag{3.60}$$

Collecting Eq 3.57 and Eq 3.60, therefore we have proved that the discrete-time map $\mathbf{F}_t$ is an orthogonal matrix. This implies that $\mathbf{F}_t$ is invertible and the inversion matrix is $\mathbf{F}_t^T$. In above discussions we have assumed that matrices and vectors are real, and superscript "T" denotes the transpose.

The corresponding discrete-time map for Eq 3.49 can be derived as below. Specifically, given the continuous-time flow equation (3.49) and the skew-symmetric

flow matrix $\mathbf{A}_t^{\mathbf{P}}$, it will be shown below that $\vec{\theta}_t$ is mapped to $\vec{\theta}_{t+1}$ by the matrix exponential of $\mathbf{A}_t^{\mathbf{P}}$. To see this, we first approximate Eq 3.49 in the discrete form by

$$\vec{\theta}_{t+\delta t} \cong \left(\mathbf{I} + \mathbf{\Lambda}_t^{\mathbf{P}} \cdot \delta t\right)\vec{\theta}_t \tag{3.61}$$

For a discrete-time LDS, letting $\delta t = \frac{T}{N}$, we have that:

$$\begin{aligned}\vec{\theta}_{t+T} &= \lim_{\delta t \to 0}\left(\mathbf{I} + \mathbf{A}_t^{\mathbf{P}} \cdot \delta t\right)^N \vec{\theta}_t \\ &= \lim_{N \to \infty}\left(\mathbf{I} + \frac{\mathbf{A}_t^{\mathbf{P}} \cdot T}{N}\right)^N \vec{\theta}_t\end{aligned} \tag{3.62}$$

For a skew-symmetric matrix $\mathbf{A}_t^{\mathbf{P}}$, it is known that,

$$\mathbf{A}_t^{\mathbf{P}} = \mathbf{P}\mathbf{\Lambda}\mathbf{P}^{\mathbf{H}} \tag{3.63}$$

$$\mathbf{P}\mathbf{P}^{\mathbf{H}} = \mathbf{P}^{\mathbf{H}}\mathbf{P} = \mathbf{I} \tag{3.64}$$

where superscript "H" denotes the transposed conjugate, and $\mathbf{\Lambda}$ is the diagonal matrix with zero or purely imaginary eigen-values.

Substituting Eq 3.63 into Eq 3.62 and using Eq 3.64, we obtain:

$$\begin{aligned}\vec{\theta}_{t+T} &= \lim_{N \to \infty}\left(\mathbf{P}\mathbf{P}^{\mathbf{H}} + \frac{\mathbf{P}\mathbf{\Lambda}\mathbf{P}^{\mathbf{H}} \cdot T}{N}\right)^N \vec{\theta}_t \\ &= \lim_{N \to \infty}\left(\mathbf{P}(\mathbf{I} + \frac{\mathbf{\Lambda} \cdot T}{N})\mathbf{P}^{\mathbf{H}} \cdot \mathbf{P}(\mathbf{I} + \frac{\mathbf{\Lambda} \cdot T}{N})\mathbf{P}^{\mathbf{H}} \cdots \mathbf{P}(\mathbf{I} + \frac{\mathbf{\Lambda} \cdot T}{N})\mathbf{P}^{\mathbf{H}} \cdot \mathbf{P}(\mathbf{I} + \frac{\mathbf{\Lambda} \cdot T}{N})\mathbf{P}^{\mathbf{H}}\right)\vec{\theta}_t \\ &= \lim_{N \to \infty}\mathbf{P}\begin{pmatrix} \ddots & 0 & 0 \\ 0 & (1 + \frac{\lambda_i \cdot T}{N})^N & 0 \\ 0 & 0 & \ddots \end{pmatrix}\mathbf{P}^{\mathbf{H}}\vec{\theta}_t = \mathbf{P}\begin{pmatrix} \ddots & 0 & 0 \\ 0 & e^{\lambda_i \cdot T} & 0 \\ 0 & 0 & \ddots \end{pmatrix}\mathbf{P}^{\mathbf{H}}\vec{\theta}_t \\ &\equiv \mathbf{P} \cdot e^{\mathbf{\Lambda} \cdot T} \cdot \mathbf{P}^{\mathbf{H}}\vec{\theta}_t \equiv e^{\mathbf{A}_t^{\mathbf{P}} \cdot T}\vec{\theta}_t\end{aligned} \tag{3.65}$$

Let $T = 1$ in above equation, we therefore get

$$\vec{\theta}_{t+1} = e^{\mathbf{A}_t^{\mathbf{P}}}\vec{\theta}_t \equiv \mathbf{F}_t\,\vec{\theta}_t \tag{3.66}$$

Similarly we may prove that the discrete-time map, $\mathbf{F}_t \equiv e^{\mathbf{A}_t^P}$, is real, given that $\mathbf{A}_t^P$ is real. From the above equation it is also seen that,

$$\mathbf{F}_t^H\mathbf{F}_t = \mathbf{P}\begin{pmatrix} \ddots & 0 & 0 \\ 0 & e^{-\lambda_i} & 0 \\ 0 & 0 & \ddots \end{pmatrix}\mathbf{P}^H\mathbf{P}\begin{pmatrix} \ddots & 0 & 0 \\ 0 & e^{\lambda_i} & 0 \\ 0 & 0 & \ddots \end{pmatrix}\mathbf{P}^H = \mathbf{P}\begin{pmatrix} \ddots & 0 & 0 \\ 0 & e^{-\lambda_i+\lambda_i} & 0 \\ 0 & 0 & \ddots \end{pmatrix}\mathbf{P}^H = \mathbf{I} \quad (3.67)$$

Similarly it can be shown that,

$$\mathbf{F}_t\mathbf{F}_t^H = \mathbf{I} \quad (3.68)$$

Since the discrete map $\mathbf{F}_t \equiv e^{\mathbf{A}_t^P}$ is real, we conclude that

$$\mathbf{F}_t^T\mathbf{F}_t = \mathbf{F}_t\mathbf{F}_t^T = \mathbf{I} \quad (3.69)$$

This is consistent with the previous discussion. To summarize, the motion that is modeled in Eq 3.40 can be represented by a linear flow matrix in the subspace ($\mathbf{A}_t^P$ in Eq 3.49), which is real and skew-symmetric. The corresponding discrete-time linear map is a real orthogonal matrix, which is the matrix exponential of $\mathbf{A}_t^P$. The experimental studies are conducted below to verify the above theoretical results.

c. *Empirical studies*

As shown above the motion can be represented by a skew-symmetric flow matrix in the subspace (Eq 3.53). This is one of the essential theoretical results derived from the assumption that is described in Eq 3.51. In following studies this theoretical result is verified using the observed reflectivity data.

A skew-symmetric matrix has following basic features:

1) All diagonal elements are equal to zero.

2) Non-diagonal elements are equal to the negative value of transposed elements, namely, $\mathbf{A}_{ij} = -\mathbf{A}_{ji}$.

It would also be useful to study the empirical structure characteristics of the motion matrix in the subspace. Therefore the matrix $\mathbf{A}_t^p$ in Eq 3.49 is computed for verifying the skew-symmetry and studying the empirical structure using the observed reflectivity sequence (Melbourne, FL, 1998). The data set was described in the previous chapter. The sequence consists of *48* radar images (reflectivity in dBZ) and the temporal resolution is about *5* min. The distributed motion fields are estimated beforehand by the spectral tracking algorithm. The subspace decomposition is computed by the SVD (Eq 3.20). *15* consecutive images are used for computing the SVD. The motion matrix is computed and projected into the subspace that is spanned by the *15* images. Fig 25 gives an example of eigen-images computed by the SVD and Fig 26 shows the corresponding singular value spectrum. In Fig 25 eigen-images are ordered in the significance that is measured by the singular values (Fig 26). It is seen that the decreasing singular values in general correspond to the decreasing spatial scales. It is also known that these eigen-images are orthogonal basis. Therefore they provide an empirically orthogonal and scaling representation, with neighboring basis having the feature of similar scales. A typical example of the motion matrix in subspace ($\mathbf{A}_t^p$) is shown in Fig 27. Fig 27 visualizes three important properties of matrix $\mathbf{A}_t^p$:

1) Diagonal elements are close to zero.

2) Non-diagonal elements are close to the negative value of transposed elements.

3) Matrix $\mathbf{A}_t^p$ typically has the diagonal band-structure.

The first two properties illustrate that $\mathbf{A}_t^p$ is skew-symmetric, as discussed above. To quantitatively verify the skew-symmetry, the motion matrices in subspace are computed using all the *48* reflectivity images. Then diagonal and non-diagonal elements are extracted. For the non-diagonal elements, the value of each element in the lower-left triangle versus the transposed element in the upper-right triangle is plotted in Fig 28. The fitted line accurately matches $\mathbf{A}_{t,ji}^p = -\mathbf{A}_{t,ij}^p$, as predicted by theory. The histogram of the value of diagonal elements is plotted in Fig 29, where the distribution is highly concentrated at 0. This verifies that $\mathbf{A}_{t,ii}^p = 0$.

The third property implies that the storm motion may be largely described by the interaction between neighboring eigen-components of similar scales. This empirical observation may be generalized and used for determining the model structure in following studies. The generalized assumption states that, *both storm motion and evolution processes may be modeled by the interaction between fewer neighboring empirical eigen-components, while the eigen-components are ordered in the decreasing significance for representing observed radar precipitation fields.* In following discussion of the evolutionary transition matrix, only the elements in neighbor of the diagonal are to be set nonzero and be estimated. This model structure can significantly reduce the number of parameters for the model estimation.

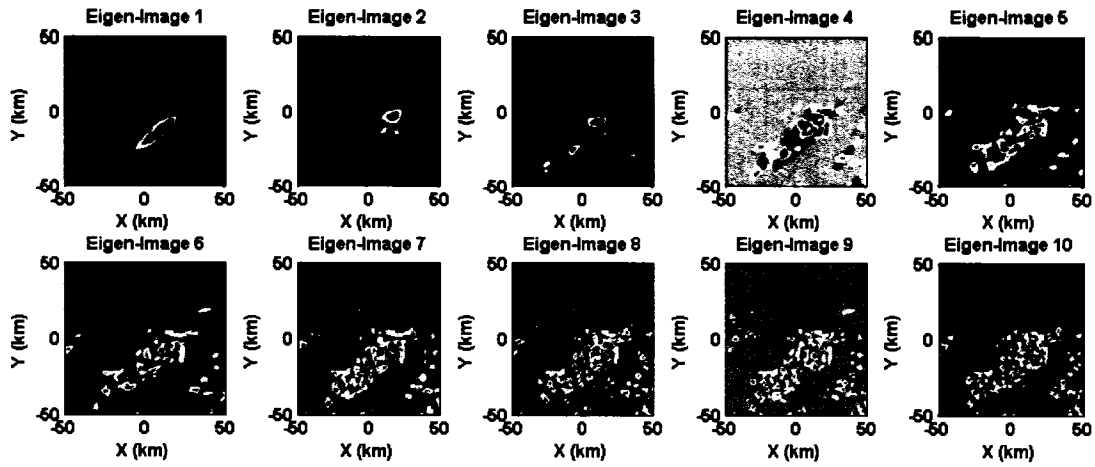

Figure 25. An example of eigen-images via SVD using 15 consecutive radar images (reflectivity in dBZ), only the first 10 eigen-images are shown.

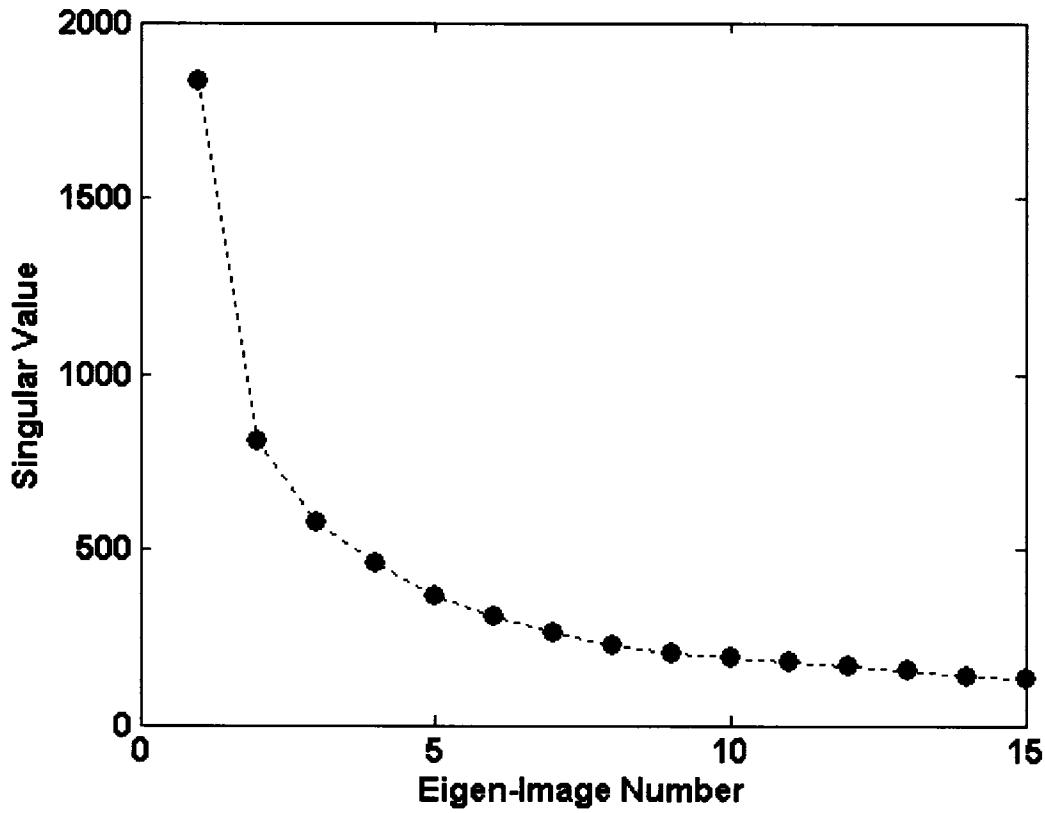

Figure 26. Singular value spectrum for the eigen-images in Fig 25.

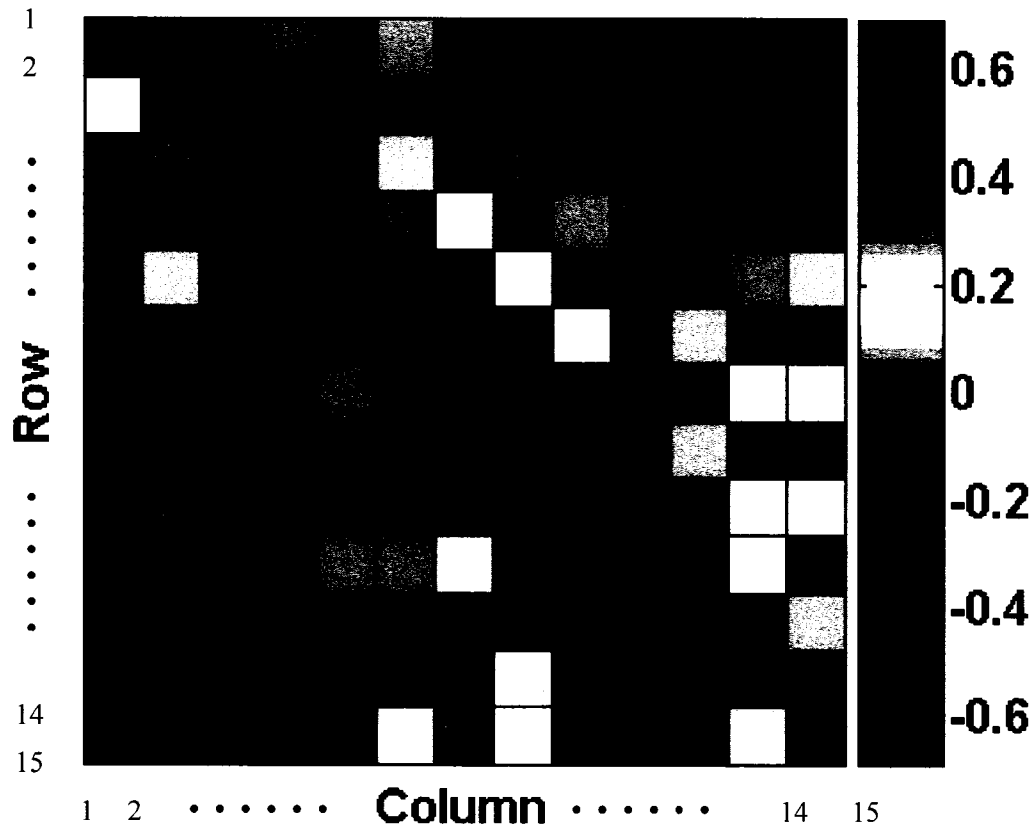

Figure 27. Example of matrix $\mathbf{A}_t^p$ represented in low-dimensional subspace, whose dimension is 15.

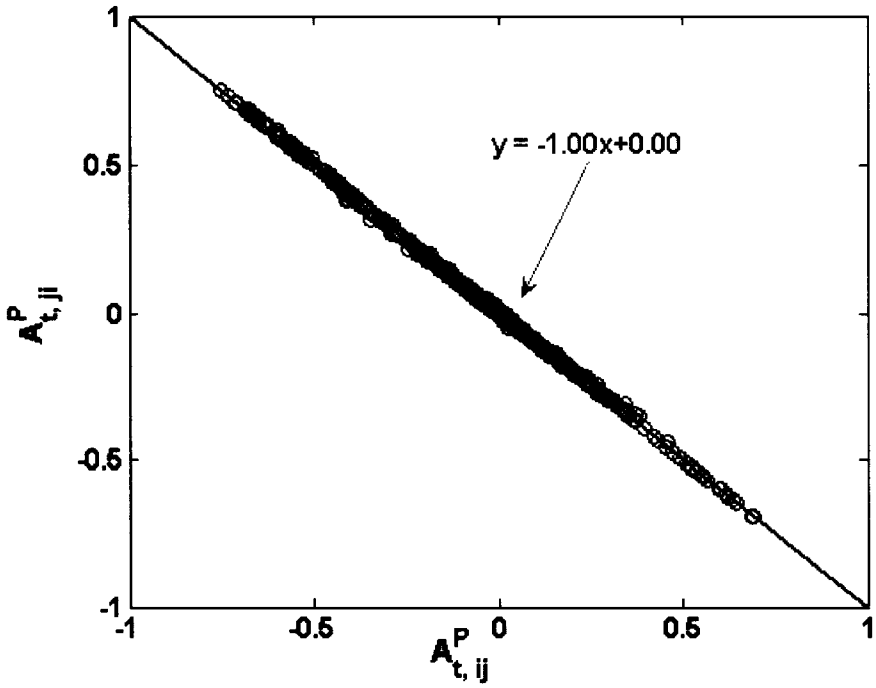

Figure 28. Value of each non-diagonal element versus its transposed element in matrix $\mathbf{A}_t^p$

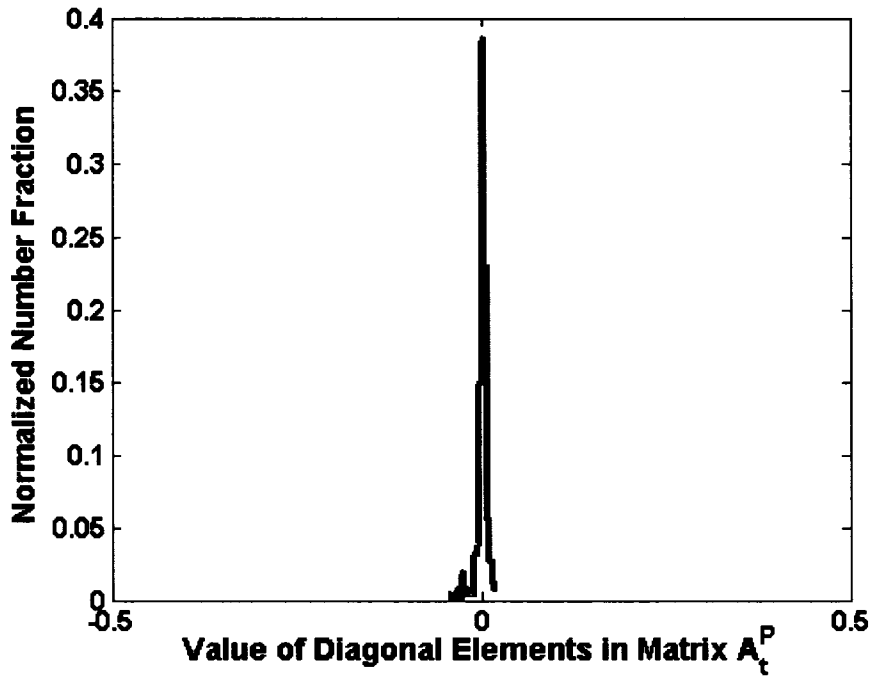

Figure 29. Histogram of the value of diagonal elements in matrix $\mathbf{A}_t^p$

3.6. Motion Compensated Temporal Alignment (MCTA) Dynamic Linear Models

To further study storm motion and storm evolution within the state-space framework, the Motion Compensated Temporal Alignment (MCTA) transformation is introduced based on three assumptions. The question that we are trying to answer here is: how can we separate the storm motion and the storm evolution in dynamic linear models (DLM)? The motivation of following discussions is to establish a generic technique to analyze dynamic storm evolutions, such as the growth and the decay, with the storm motion pattern removed. It is shown below how to generally analyze the motion and the evolution, and how to remove the motion trend and establish the evolution-only dynamic linear systems. The symmetry or the equivalency of MCTA systems is assumed.

a. *Assumptions and definitions*

It has been argued that the motion process can be adequately represented by a linear flow matrix in the vector space for the scales of measurement considered here. The derivation of the linear flow equation for the motion process has used the *SINC*-kernel function (see Eq 3.46 and Eq 3.49). However, it can be generalized, as shown below.

Substituting Eq 3.3 into the LHS of Eq 3.41, and dropping off the random noise term, we obtain (for the observations at locations $\mathbf{x} = \mathbf{x}_i$, $i = 1,\cdots,n$, and time t)

$$\sum_{j=1}^{J} K_t(\mathbf{x}_i, \mathbf{c}_j) \frac{\partial}{\partial t} \beta_t(j) = \sum_{j=1}^{J} A'_{ij,t} \beta_t(j) \tag{3.70}$$

where

$$A'_{ij,t} \equiv A_{ij,t} - \frac{\partial}{\partial t} K_t(\mathbf{x}_i, \mathbf{c}_j) \tag{3.71}$$

$A_{ij,t}$ is defined in Eq 3.42. Eq 3.70 can be rewritten in the matrix form as

$$\boldsymbol{\Phi}_t \frac{\partial}{\partial t}\vec{\mathbf{b}}_t = \mathbf{A}'_t \vec{\mathbf{b}}_t \tag{3.72}$$

where matrix $\boldsymbol{\Phi}_t$ is defined in Eq 3.6, vector $\vec{\mathbf{b}}_t$ is defined in Eq 3.7, and matrix $\mathbf{A}'_t$ is defined in Eq 3.71. Assuming that there is sufficient number of observations ($n \geq J$) and taking the pseudo-inverse of matrix $\boldsymbol{\Phi}_t$, we get that,

$$\frac{\partial}{\partial t}\vec{\mathbf{b}}_t = \mathbf{A}''_t \vec{\mathbf{b}}_t \tag{3.73}$$

where $\mathbf{A}''_t \equiv (\boldsymbol{\Phi}_t^{\mathrm{T}}\boldsymbol{\Phi}_t)^{-1}\boldsymbol{\Phi}_t^{\mathrm{T}}\mathbf{A}'_t$. Eq 3.73 gives us a linear flow equation (in comparison with Eq 3.46). We conclude that in general cases the motion process can be represented by a linear flow matrix in the finite-dimensional vector space.

To decompose the motion and the evolution processes, we next introduce and discuss a transformation that aligns radar observation fields in spatial coordinates by removing the motion trend.

The system's state at time "*t*" is represented by the vector $\vec{\boldsymbol{\theta}}_t$. As discussed above the discrete-time map for the motion process is a real orthogonal matrix, which is the matrix exponential of the continuous-time motion matrix. So the motion process at time "*t*" can be written as a linear map, namely, $\mathbf{T}_t$. It is assumed in general that $\mathbf{T}_t$ is a reversible process, i.e., the inverse $\mathbf{T}_t^{-1}$ exists. In the linear dynamic framework it is also assumed that the storm evolution can generally be written by another linear map, $\boldsymbol{\varphi}_t$. The overall temporal process that links the state at "*t*" to the state at "*t+1*" is a composite process. It is given by the composite linear map "$\boldsymbol{\varphi}_t\mathbf{T}_t$". It is further assumed that the evolution process is invariant under the motion transformation, though these two processes are not commutable in the simplistic way. These assumptions are summarized as follows.

Assumption 3.1 *Motion is an* ***invertible linear map*** $\mathbf{T}_t$ $(\exists\ \mathbf{T}_t^{-1})$.

Assumption 3.2 The *overall temporal change from "t" to "t+1" is a* ***composite*** *process*

$$\vec{\theta}_{t+1} = \varphi_t \mathbf{T}_t \vec{\theta}_t \tag{3.74}$$

where φ_t *is called* ***linear evolution.***

Assumption 3.3 *Linear evolution* φ_t *is* ***motion-invariant*** *(or:* ***symmetric*** *with respect to motion map* $\mathbf{T}_t$*)*

$$\varphi_t = \mathbf{T}_t \varphi_{t-1} \mathbf{T}_t^{-1} \tag{3.75}$$

Assumption 3.3 states the equivalency of linear evolution maps at different time. For the generalized models, assumption 3.3 may not be necessary. Here for temporal sequences of a short time period and weakly time-dependent dynamics, this is assumed to be a good approximation. Eq 3.74 tells that, at each step from "*t*" to "*t+1*", the overall temporal change is decomposed into two sequential processes: first, an intermediate state, $\vec{\theta}'_t = \mathbf{T}_t \vec{\theta}_t$, is obtained via the motion transformation. Then the state of next step, $\vec{\theta}_{t+1} = \varphi_t \vec{\theta}'_t$, is obtained via the linear evolution of the intermediate state. Intuitively the first step of motion process is to align the location of radar precipitation fields at time "*t*" and time "*t+1*" with reference to time "*t+1*". This is essentially the idea for motion tracking and extrapolative nowcasting. This is also the key element for us to introduce the MCTA sequence. Briefly speaking, we firstly align all radar precipitation fields with reference to a certain temporal point, and we secondly link these aligned radar precipitation fields via the evolutionary map. The alignment transformation in the first

step, which gives us a new vector sequence, is called the Motion Compensated Temporal Alignment (MCTA).

Definition 3.6 The *MCTA sequence* is a finite sequence defined as follows

$$\{\mathbf{T}_t\mathbf{T}_{t-1}\cdots\mathbf{T}_1\vec{\theta}_1,\ \cdots,\ \mathbf{T}_t\mathbf{T}_{t-1}\vec{\theta}_{t-1},\ \mathbf{T}_t\vec{\theta}_t\} \tag{3.76}$$

Or

$$\{\vec{\theta}'_\tau\ :\ \vec{\theta}'_\tau \equiv \mathbf{T}_t\mathbf{T}_{t-1}\cdots\mathbf{T}_\tau\vec{\theta}_\tau,\ \tau=1,\ \cdots,\ t\} \tag{3.77}$$

In the MCTA sequence defined in equations (3.76) and (3.77), all vectors are aligned with reference to time "$t+1$". The general way is to define such a sequence with reference to an arbitrarily fixed temporal point.

Definition 3.7 The *generalized MCTA sequence* is defined by

$$\{\cdots,\vec{\chi}_\tau,\cdots;\ \vec{\chi}_t;\ \cdots,\vec{\chi}_{t+m},\cdots;\ \tau<t,\ m\geq 1\} \tag{3.78}$$

$$\text{(a) } \vec{\chi}_\tau \equiv \mathbf{T}_{t-1}\cdots\mathbf{T}_\tau\vec{\theta}_\tau,\ \tau=1,\ \cdots,\ t-1; \tag{3.79}$$

$$\text{(b) } \vec{\chi}_t \equiv \vec{\theta}_t; \tag{3.80}$$

$$\text{(c) } \vec{\chi}_{t+m} \equiv \mathbf{T}_t^{-1}\cdots\mathbf{T}_{t+m-1}^{-1}\vec{\theta}_{t+m},\ 1\leq m<\infty \tag{3.81}$$

In above definitions and discussions, $\vec{\theta}$ is the state vector in a vector space of finite dimension, and $\mathbf{T}_t$ is the discrete-time motion matrix that is real, invertible, finite and square.

b. *Analysis of MCTA sequence*

Starting from above assumptions and definitions, we can easily establish following general properties for MCTA sequences.

Theorem 3.2 (***MCTA Sequence***)

The MCTA sequence $\{\vec{\theta}'_\tau\}$ defined in Eq 3.77 is a linear dynamic process given by

$$\vec{\theta}'_{\tau+1} = \varphi_t \vec{\theta}'_\tau \quad (\forall 1 \le \tau,\ \tau+1 \le t+1) \tag{3.82}$$

Proof: $\forall 1 \le \tau,\ \tau+1 \le t+1$,

$$\vec{\theta}_{\tau+1} = \varphi_\tau \mathbf{T}_\tau \vec{\theta}_\tau \tag{3.83}$$

Multiplying both sides by $\mathbf{T}_{\tau+1}$ from the left gives,

$$\mathbf{T}_{\tau+1}\vec{\theta}_{\tau+1} = \mathbf{T}_{\tau+1}\varphi_\tau \mathbf{T}_\tau \vec{\theta}_\tau$$

$$\Rightarrow \mathbf{T}_{\tau+1}\vec{\theta}_{\tau+1} = (\mathbf{T}_{\tau+1}\varphi_\tau \mathbf{T}_{\tau+1}^{-1})\mathbf{T}_{\tau+1}\mathbf{T}_\tau \vec{\theta}_\tau$$

$$\Rightarrow \mathbf{T}_{\tau+1}\vec{\theta}_{\tau+1} = \varphi_{\tau+1}(\mathbf{T}_{\tau+1}\mathbf{T}_\tau \vec{\theta}_\tau) \tag{3.84}$$

Multiplying both sides from the left by $\mathbf{T}_{\tau+2}$ and repeating the above derivation recursively, we therefore get that,

$$\mathbf{T}_t \cdots \mathbf{T}_{\tau+1}\vec{\theta}_{\tau+1} = \varphi_t(\mathbf{T}_t \cdots \mathbf{T}_{\tau+1}\mathbf{T}_\tau \vec{\theta}_\tau) \tag{3.85}$$

$$\Rightarrow \vec{\theta}'_{\tau+1} = \varphi_t \vec{\theta}'_\tau \qquad \text{(Q.E.D.)} \tag{3.86}$$

Theorem 3.3 (***Generalized MCTA Sequence***)

The generalized MCTA sequence that is defined in Eq 3.78, aligned with reference to time "*t*", is a linear dynamic process given by

$$\vec{\chi}_{k+1} = \varphi_{t-1}\vec{\chi}_k \tag{3.87}$$

$\forall \vec{\chi}_k,\ \vec{\chi}_{k+1} \in \{\cdots, \vec{\chi}_\tau, \cdots;\ \vec{\chi}_t;\ \cdots, \vec{\chi}_{t+m}, \cdots;\ \tau < t,\ m \ge 1\}$.

Proof: as shown in theorem 3.2, $\forall \vec{\chi}_\tau,\ \vec{\chi}_t$ $(\tau < t)$, we have that

$$\vec{\chi}_{\tau+1} = \varphi_{t-1}\vec{\chi}_\tau \qquad (\tau < t) \tag{3.88}$$

Next we show a simple lemma: given

$$\vec{\beta} = \varphi_k \mathbf{T}_k \vec{\alpha} \qquad (\forall \vec{\alpha},\ \vec{\beta}) \tag{3.89}$$

multiplying both sides from the left by $\mathbf{T}_k^{-1}$, and applying Eq 3.75, then

$$\begin{aligned} &\mathbf{T}_k^{-1}\vec{\boldsymbol{\beta}} = \mathbf{T}_k^{-1}\boldsymbol{\varphi}_k\mathbf{T}_k\vec{\boldsymbol{\alpha}} \\ &\Rightarrow (\mathbf{T}_k^{-1}\vec{\boldsymbol{\beta}}) = \boldsymbol{\varphi}_{k-1}\mathbf{T}_{k-1}(\mathbf{T}_{k-1}^{-1}\vec{\boldsymbol{\alpha}}) \end{aligned} \tag{3.90}$$

For $\vec{\chi}_t$, $\vec{\chi}_{t+m}$ $(m \geq 1)$, starting from

$$\vec{\boldsymbol{\theta}}_{t+m} = \boldsymbol{\varphi}_{t+m-1}\mathbf{T}_{t+m-1}\vec{\boldsymbol{\theta}}_{t+m-1} \quad (m \geq 1) \tag{3.91}$$

and repeatedly applying the lemma given by Eq 3.90, we get that,

$$\Rightarrow (\mathbf{T}_{t+m-1}^{-1}\vec{\boldsymbol{\theta}}_{t+m}) = \boldsymbol{\varphi}_{t+m-2}\mathbf{T}_{t+m-2}(\mathbf{T}_{t+m-2}^{-1}\vec{\boldsymbol{\theta}}_{t+m-1})$$

$$\Rightarrow (\mathbf{T}_{t+m-2}^{-1}\mathbf{T}_{t+m-1}^{-1}\vec{\boldsymbol{\theta}}_{t+m}) = \boldsymbol{\varphi}_{t+m-3}\mathbf{T}_{t+m-3}(\mathbf{T}_{t+m-3}^{-1}\mathbf{T}_{t+m-2}^{-1}\vec{\boldsymbol{\theta}}_{t+m-1})$$

$$\Rightarrow (\mathbf{T}_t^{-1}\cdots\mathbf{T}_{t+m-1}^{-1}\vec{\boldsymbol{\theta}}_{t+m}) = \boldsymbol{\varphi}_{t-1}\mathbf{T}_{t-1}(\mathbf{T}_{t-1}^{-1}\mathbf{T}_t^{-1}\cdots\mathbf{T}_{t+m-2}^{-1}\vec{\boldsymbol{\theta}}_{t+m-1}) \quad \text{(by recursion)}$$

$$\Rightarrow (\mathbf{T}_t^{-1}\cdots\mathbf{T}_{t+m-1}^{-1}\vec{\boldsymbol{\theta}}_{t+m}) = \boldsymbol{\varphi}_{t-1}\mathbf{T}_{t-1}\mathbf{T}_{t-1}^{-1}(\mathbf{T}_t^{-1}\cdots\mathbf{T}_{t+m-2}^{-1}\vec{\boldsymbol{\theta}}_{t+m-1})$$

$$\Rightarrow (\mathbf{T}_t^{-1}\cdots\mathbf{T}_{t+m-1}^{-1}\vec{\boldsymbol{\theta}}_{t+m}) = \boldsymbol{\varphi}_{t-1}(\mathbf{T}_t^{-1}\cdots\mathbf{T}_{t+m-2}^{-1}\vec{\boldsymbol{\theta}}_{t+m-1}) \tag{3.92}$$

According to Eq 3.81, the last line simply gives:

$$\vec{\chi}_{t+m} = \boldsymbol{\varphi}_{t-1}\vec{\chi}_{t+m-1} \quad (m \geq 1) \tag{3.93}$$

Following equations (3.88) and (3.93), the theorem is proved (Q.E.D.).

The following result establishes the equivalency between the composite process $\boldsymbol{\varphi}_t\mathbf{T}_t$ and the commutative process $\mathbf{T}_t\boldsymbol{\varphi}_{t-1}$.

Corollary 3.1 (***Commutative Composite Process***)

Composite linear dynamic systems (Eq 3.74) satisfying the motion-invariance (Eq 3.75) have the following commutative dynamics

$$\vec{\boldsymbol{\theta}}_{t+1} = \mathbf{T}_t\boldsymbol{\varphi}_{t-1}\vec{\boldsymbol{\theta}}_t \tag{3.94}$$

Or

$$\mathbf{T}_t^{-1}\vec{\theta}_{t+1} = \varphi_{t-1}\vec{\theta}_t \tag{3.95}$$

Proof: Multiplying Eq 3.75 by $\mathbf{T}_t$ from the right, we get

$$\varphi_t\mathbf{T}_t = \mathbf{T}_t\varphi_{t-1} \tag{3.96}$$

Substituting this result into Eq 3.74 gives that

$$\vec{\theta}_{t+1} = \mathbf{T}_t\varphi_{t-1}\vec{\theta}_t \quad \text{(Q.E.D.)} \tag{3.97}$$

This result tells that the motion process and evolution process cannot commute with each other in the simplistic way. As they commute the linear evolution would have to shift one step in time to account for the motion effect.

Above theorems show that, in any MCTA sequence, two successive state vectors associated with two radar fields are linked by a single evolutionary matrix. This matrix is though dependent on the reference time and has certain symmetric property (Eq 3.75). Therefore only evolutionary dynamics are to be modeled in any of the MCTA spaces and these models are equivalently related through an invariance transformation (Eq 3.75). An MCTA sequence forms a space where the evolution of radar fields is ascribed to the dynamic processes other than the storm movement, and therefore the evolution-only processes can be modeled in the MCTA space.

Fig 30 shows an example of the MCTA sequence computed using *9* reflectivity fields from the WSR-88D radar in Melbourne, FL (1998). It is seen that all reflectivity fields are well aligned in spatial coordinates, and all temporal changes among them are ascribed to the dynamic evolution process.

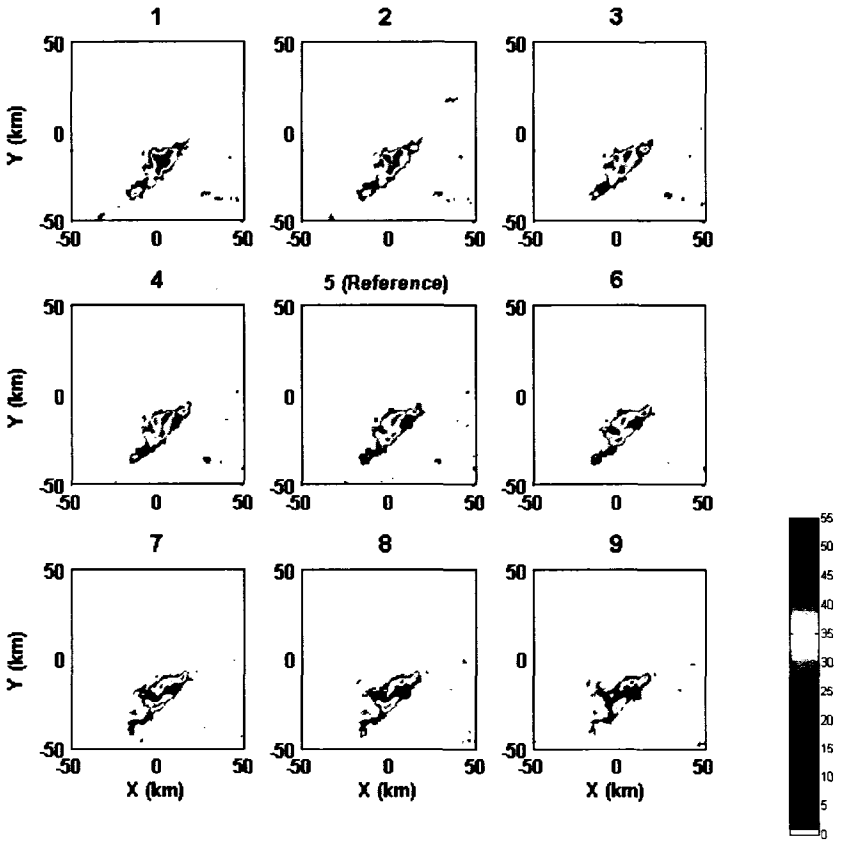

Figure 30. An example of MCTA sequence consisting of nine reflectivity images: all images are aligned with reference to the 5^{th} image.

CHAPTER IV. SPACE-TIME MODELING OF RADAR OBSERVATIONS – MODEL ESTIMATION, CLASSIFICATION AND SIMULATION

4.1. Model Estimation

The theoretical background for the space-time modeling of radar observations has been developed in chapter three. In this chapter the theory is applied to characterizing the space-time variability of radar observations. The space-time model is first estimated using the short sequence of observed radar fields. Then the characteristic parameters derived from model parameters are used for the storm classification and the stochastic simulation. The empirical studies in chapter three revealed that the eigen-images based on the SVD provide an empirically scaling representation, namely, the decreasing singular values in general correspond to the decreasing spatial scales of eigen-images. Therefore the singular value spectrum can be used to characterize the spatial variability of radar observations. The temporal processes of radar observations consist of the storm motion and the storm evolution. The motion-compensated temporal alignment (MCTA) transformation developed in chapter three is applied to remove the motion trend. Only the linear evolution model is estimated in the MCTA space. The linear evolution matrix is assumed to have the diagonal band structure, which can be estimated based on the radar observations. According to the linear dynamic system (LDS) theory, the eigen-frequencies of the evolutionary matrix can therefore be used to characterize the temporal variability of radar observations. The spatiotemporal characteristic variables are combined to form the feature vector for the clustering analysis. The estimated model

based on radar observations is further used for simulating the stochastic space-time radar reflectivity field (dBZ). The details of the model estimation procedure are described as follows.

The first step for the model estimation is to obtain the storm motion and conduct the motion-compensated temporal alignment (MCTA). Specifically, given a short sequence of radar reflectivity images, the motion field is estimated by applying the spectral algorithm developed in chapter two. Then the MCTA is performed by either forward or backward advection of radar images with reference to the image in the middle of sequence. The MCTA sequence obtained this way will be used in the following steps.

The second step for the model estimation is to compute the spatial modeling and dimension reduction by the SVD. As discussed in chapter three, the observation vector essentially consists of the radar measurement values at regular pixels. Using the SINC-kernel in the spatial modeling, observation vectors can be directly used for computing the SVD. Specifically, the sequence of radar images is converted to the sequence of vectors. The data matrix is constructed by taking each vector as one of the columns. Then the SVD is computed on the data matrix. The projection matrix and the singular values obtained here will be used in the temporal modeling and estimation.

The third step for the model estimation is to compute the state vectors in the subspace and estimate the dynamic flow matrix using the sequence of state vectors. To reduce the number of estimated parameters in linear map matrix, only the diagonal elements, the nearest and the second nearest neighboring elements to diagonals are estimated. All other elements are zeros. To approximate the flow matrix in the continuous linear dynamic system, the interpolation on the time axis is conducted before computing state vectors.

The interpolation is conducted using the conventional SINC-kernels. The flow diagram for model estimation is summarized in Fig 31.

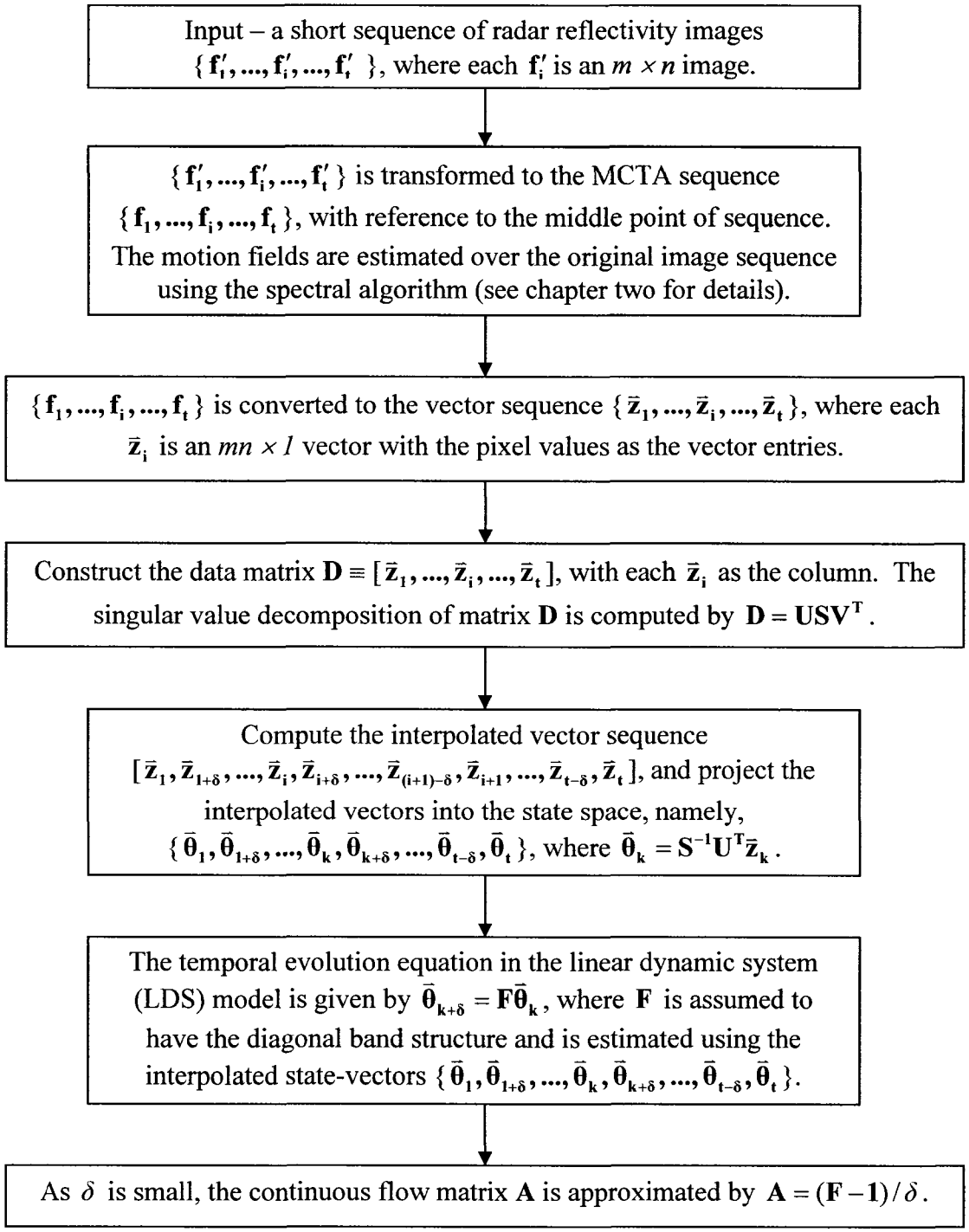

Figure 31. The procedure of model estimation for space-time radar reflectivity fields (dBZ).

4.2. Characterization of Space-Time Variability of Radar Observations

The estimation of space-time radar reflectivity model has been described in the previous section. Below the estimated model parameters are applied to characterizing the spatiotemporal variability of observed radar reflectivity fields. It is also shown that the estimated feature variables can be further applied to classifying storms based on both spatial characteristics and dynamic characteristics. The results obtained in current research are consistent with previous findings by other researchers (Wilson et al 1998; Germann and Zawadzki 2002). In current research a general model is developed that is able to combine both spatial characteristics and dynamic characteristics of radar observations for classification and simulation.

a. *Spatial characterization*

As discussed above the eigen-images are computed using the observed reflectivity images. Typical eigen-images are generally ordered in decreasing spatial scales along with decreasing singular values, as shown in Fig 33. These eigen-images are computed using the observed reflectivity images in Fig 32. Since each singular value weights the corresponding eigen-image for reconstructing observed radar images, the singular value spectrum encodes the spatial scaling characteristics of observed radar fields. The larger scale storms tend to be weighed more in smaller eigen-numbers, while the smaller scale storms tend to shift the weights toward the larger eigen-numbers. Therefore the singular value spectrum can be used to characterize the spatial variability of radar fields. The parameters for the spatial characterization consist of the maximal singular value and the ratios of the maximal singular value to all other singular values. The larger are these parameters, the larger spatial scale the radar fields have.

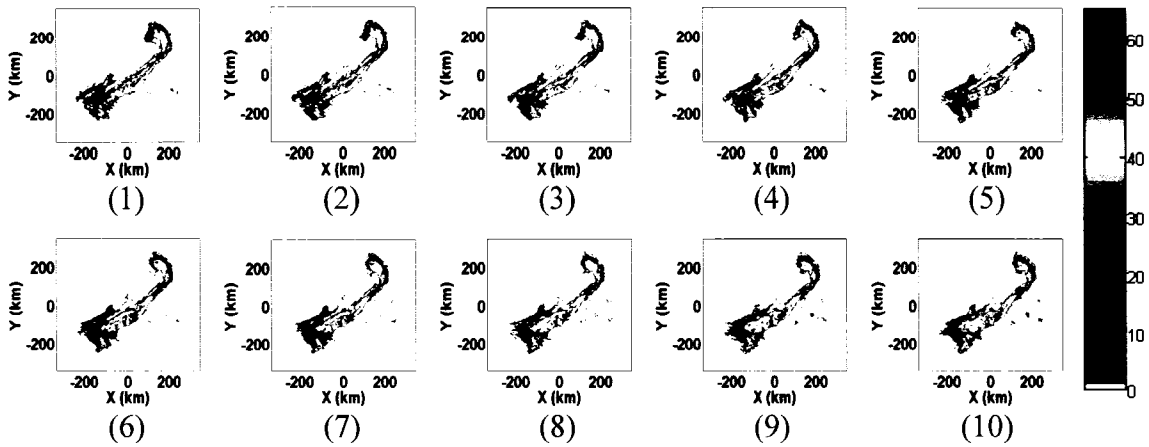

Figure 32. An observed sequence of ten reflectivity images (dBZ). The data was collected by the KOUN radar on June 6th, 2003 (03:40 UTC – 09:59 UTC). The spatial resolution is 3 km and the temporal resolution is approximately 6.5 minutes.

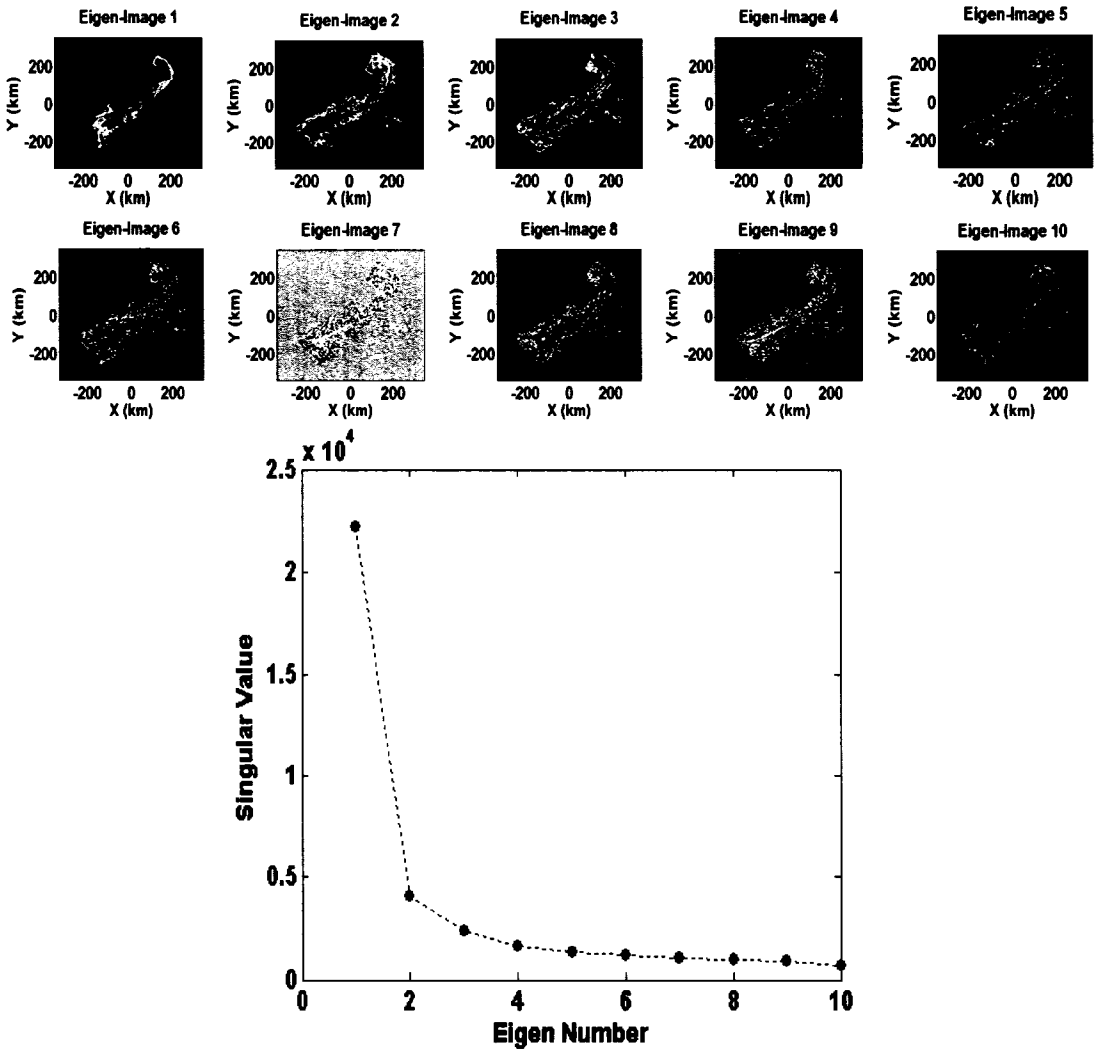

Figure 33. Eigen-images and the singular values for the observed reflectivity sequence in Fig 32.

b. *Temporal characterization*

The temporal variability of radar fields is modeled by state space dynamics. The linear evolution matrix in the MCTA subspace is estimated as described in Fig 31. According to the linear dynamic theory, important dynamic characteristics are determined by the eigen-frequencies of linear flow matrix (**A**) when the continuous-time model is used. Therefore the eigen-frequencies of estimated flow matrix (**A**) can be used to characterize the temporal variability of radar fields. The characteristic parameters consist of the inverses of the eigen-frequencies of linear flow matrix (**A**). These parameters explicitly represent the temporal scales of dynamic variations in observed radar fields. The estimated linear flow matrix in the state space for the sequence of reflectivity images in Fig 32 is given by

$$\mathbf{A} = \begin{bmatrix} 0 & .001 & -.0001 & 0 & 0 & 0 & 0 & 0 & 0 & 0 \\ -.044 & 0 & .028 & .004 & 0 & 0 & 0 & 0 & 0 & 0 \\ -.001 & -.087 & 0 & .059 & -.003 & 0 & 0 & 0 & 0 & 0 \\ 0 & .001 & -.12 & 0 & -.092 & -.028 & 0 & 0 & 0 & 0 \\ 0 & 0 & .020 & .145 & 0 & -.112 & -.019 & 0 & 0 & 0 \\ 0 & 0 & 0 & .030 & .163 & 0 & .144 & -.046 & 0 & 0 \\ 0 & 0 & 0 & 0 & .046 & -.180 & 0 & .186 & .047 & 0 \\ 0 & 0 & 0 & 0 & 0 & .047 & -.207 & 0 & .249 & .017 \\ 0 & 0 & 0 & 0 & 0 & 0 & -.058 & -.262 & 0 & -.284 \\ 0 & 0 & 0 & 0 & 0 & 0 & 0 & .017 & -.325 & 0 \end{bmatrix} \quad (\text{min}^{-1}) \qquad (4.1)$$

The characteristic durations that correspond to five eigen-frequencies of matrix **A** are 14.7 minutes, 25.6 minutes, 42.7 minutes, 99.7 minutes, and 1799.1 minutes, respectively.

c. *Case Studies*

As discussed above the characteristic parameters in spatial model are the maximal singular value and the ratios of the maximum singular value to other singular values, and the characteristic parameters in temporal model are inverses of the eigen-frequencies of

linear flow matrix. The spatial parameters represent how observed radar fields are distributed over different empirical scales, while the temporal parameters characterize the dynamic durations of observed radar fields. So these parameters are used to define the feature vector for the short sequence of reflectivity images. This feature vector can be used for discriminative analysis and classification applications. The temporal feature variables combined with the SVD analysis provide further understanding of dynamic variability for different empirical scaling components in observed radar fields. Case studies using the observed radar reflectivity during three months are conducted below to demonstrate these applications.

The data for the case studies were collected by the KOUN radar located at Norman (OK). The radar reflectivity (ZH in dBZ) and differential reflectivity (ZDR in dB) for the storm events over April, May and June in 2003 are used. The storm days and time of all available data are listed in Table 4. During the pre-processing, all the raw data in sweeps are combined to generate the volume data. Then the CAPPI data at 2-km height in Cartesian coordinates are extracted from each volume scan. The obtained radar images are within the two-dimensional spatial region: -348 km $\leq x, y \leq$ 348 km. KOUN radar is located at the origin of the coordinates. The pixel resolution of each radar image is 3 km by 3 km. The 3-km resolution instead of 1-km resolution is used here to make the large amount of data manageable for computers. The temporal resolution for all image sequences is approximately 6.5 minutes.

To estimate the model for a short sequence of reflectivity images, a 14-frame sliding window is used. For each whole storm sequence, the first 14-frame short sequence is used for estimating the model parameters. Then the window slides forward two frames

and the next 14-frame image sequence is used for estimating the next model's parameters. This proceeds until the end of the whole data sequence is reached. For each short image sequence (14-frame), the space-time model is estimated by following the procedure described in Fig 31. The parameters that are stored include the spatiotemporal feature vectors described above, the eigen-images in reconstruction matrix **U** (Fig 31), the singular values computed by SVD, and the linear flow matrix in the MCTA subspace. These model parameters can be applied to the classification and the stochastic simulation of radar storm fields.

The classification based on the spatiotemporal features using KOUN dataset is reported here. The following results are based on the model estimation for 14-frame short sequences. After collecting the feature vectors of all short sequences, the K-means clustering algorithm (Duda, Hart and Stork 2000) is applied and the feature vectors are partitioned into two clusters. The mean vector for each cluster is computed and reported. The case studies are conducted as follows.

The 14-frame window is employed for each short sequence. The parameters of mean feature vectors for two clusters are shown in Table 5. From Table 5 we see that the characteristic time for KOUN reflectivity data over three months ranges from tens of minutes to thousands of minutes. The dominant discriminative parameters for partitioning two-class feature vectors are singular value ratios and the largest characteristic time, while the smaller characteristic temporal scales remain similar between two classes. As discussed above the larger singular value ratios imply the larger spatial scales of reflectivity fields. It is also seen in Table 5 that the space-time reflectivity fields of class 1 have the larger spatial scales as well as the larger temporal

scales. This implies that there exist the positive correlations between spatial scales and temporal scales, which is consistent with previous studies (Wilson et al 1998; Germann and Zawadzki 2002).

Table 4. Storm days and time of KOUN radar data in 2003. KOUN radar is located at Norman, OK.

Day	Start (UTC)	End (UTC)	Day	Start (UTC)	End (UTC)
April 19	04:38:02	14:08:58	June 05	05:34:41	16:33:43
April 23	13:25:35	23:57:30	June 06	01:28:54	04:05:33
April 24	00:04:02	07:08:08	June 10	21:09:19	23:52:13
May 8	04:38:03	23:43:07	June 11	00:00:25	04:06:19
May 10 (a)	00:04:43	06:27:48	June 12 (a)	01:38:37	04:51:41
May 10 (b)	16:50:12	20:14:42	June 12 (b)	11:55:49	15:37:40
May 14	04:00:40	13:39:09	June 13 (a)	10:45:45	14:22:04
May 16	05:26:08	21:03:56	June 13 (b)	23:35:10	23:54:45
May 19	22:31:33	23:56:25	June 14 (a)	00:01:18	01:52:16
May 20	00:02:57	10:35:58	June 14 (b)	17:58:52	20:44:56
May 24	07:59:17	15:22:56	June 14 (c)	23:08:34	23:54:17
June 2	03:44:17	07:08:50	June 15	00:00:49	01:58:22
June 04	11:08:19	17:55:57	June 26	00:10:42	07:47:25

Table 5. Characteristic parameters of mean feature vectors for two clusters: model parameters are estimated based on 14-frame windows of reflectivity (dBZ) over three months in 2003 (KOUN). Singular-value ratios are ratios of the maximum value to all values.

Singular-Value Ratios	
Class 1	Class 2
21.10	13.98
19.72	13.02
18.66	12.32
17.73	11.69
16.65	11.07
15.47	10.23
14.16	9.34
12.70	8.41
11.07	7.39
9.24	6.16
7.27	4.96
5.25	3.71
3.31	2.36
1.0	1.0

Characteristic Time (minute)	
Class 1	Class 2
1652.5	1068.1
165.2	159.6
73.5	72.3
43.6	43.3
29.3	29.7
22.2	22.2
17.1	17.6

Magnitude for Characteristic Time	
Class 1	Class 2
0.336	0.319
0.280	0.261
0.183	0.175
0.112	0.118
0.080	0.085
0.075	0.066
0.064	0.050

4.3. Stochastic Simulation of Radar Reflectivity

The estimated model and parameters obtained in above studies can be further applied to simulating the space-time radar reflectivity fields. As discussed above the spatial variability can be controlled by the singular value spectrum, and the temporal or dynamic variability can be controlled by the characteristic time for the linear flow matrix. The simulation procedure based on this principle assumes that the eigen-images that give an empirical scaling representation are available. Therefore it requires that a large database of space-time radar observations should be available. Equipped with the models estimated for short sequences of reflectivity images, the procedure for the stochastic simulation of space-time radar reflectivity is detailed below.

Step 1: *the characteristic times are specified based on the estimated values*. The inverse of these parameters gives the eigen-frequencies of linear flow matrix. These parameters determine how fast the temporal variations of simulated reflectivity fields are. The number of eigen-frequencies is determined by the dimension of subspace. It is given by

$$n_{eign} = \text{int}(\frac{p}{2}) \tag{4.2}$$

where p is the dimension of the subspace and function "int(x)" gives the integer part of variable "x". For example, for the 14-frame short sequences, the subspace dimension is 14 and the number of eigen-frequencies is 7.

Step 2: *the linear map matrix is generated based on the specified eigen-frequencies*. Given the estimated linear flow matrices for short sequences, the histograms of the nearest and the second nearest elements to diagonals are computed. The nearest and the second nearest elements to the diagonal of flow matrix are stochastically generated using

these histograms. As discussed in chapter three, the flow matrix is skew-symmetric. Therefore only half of the matrix elements need to be simulated and the transposed elements are determined by taking negative values. The eigen-vectors of the simulated flow matrix are computed, while the eigen-values are replaced by the eigen-frequencies specified in step 1. As shown in chapter three, the discrete mapping matrix **F** is given by

$$\mathbf{F} = \mathbf{X}\exp(i\Lambda \cdot \delta t)\mathbf{X}' \tag{4.3}$$

where columns of matrix **X** are eigen-vectors of the simulated flow matrix, $\mathbf{X}'$ is the transposed conjugate of **X**, and Λ is the diagonal matrix consists of specified eigen-frequencies. δt is the step time of discrete linear map.

Step 3: *the initial state vector* $\vec{\theta}_0$ *is randomly initialized and is normalized.* Once the initial state vector is generated, subsequent state vectors are iteratively computed by

$$\vec{\theta}_{t+\delta t} = \mathbf{F}\vec{\theta}_t \quad (t \geq 0) \tag{4.4}$$

Step 4: *the singular value spectrum is specified based on estimated values.* The singular values in diagonal matrix **S** are computed by the SVD (Fig 31). These values are replaced by the specified values to control the spatial variability. The leading values are increased for simulating the larger scale reflectivity fields, while the leading values are decreased for simulating the smaller scale reflectivity fields. Due to the dependency of spatial scales and temporal scales, the spatial variability determined by singular values and the temporal variability determined by eigen-frequencies should be specified consistently to generate the simulation that makes physical sense.

Step 5: *each reflectivity field is reconstructed using eigen-images in the given database.* Using the eigen-images stored in matrix **U**, each reflectivity image is reconstructed by

$$\mathbf{I}_t = \mathbf{US}\vec{\theta}_t \tag{4.5}$$

Step 6: *each simulated reflectivity image is advected forwardly or backwardly using the simulated motion field.* The motion field is simulated in the spectral domain, where the power spectrum has the exponentially decaying form $\propto \exp(-\frac{\sqrt{k_x^2 + k_y^2}}{a})$, and phases are random with a uniform distribution over $[0, 2\pi]$. The decay constant "a" is 0.85 for all simulations. The inverse fast Fourier transform is used to compute the motion field in the spatial domain. This approach is developed through empirical experiments. The motion field simulated in this way gives qualitatively realistic motion field that is comparable to the motion field estimated from the reflectivity data. Since the reflectivity images generated in step 5 are all in the MCTA space, the motion mechanism is directly simulated by the advection with reference to a given radar image.

In current studies the KOUN dataset over three months in 2003 is used for demonstrating the application of space-time models on stochastic simulation of radar reflectivity fields. Three types of simulations are conducted and the examples of simulated reflectivity sequences are demonstrated below.

a. *Simulation 1 – larger scale reflectivity field with slower variation*

In the first simulation the eigen-images are obtained using the reflectivity data observed by the KOUN radar on June 6th, 2003 (03:40 UTC – 09:59 UTC). A 1-hour larger-scale reflectivity sequence is simulated. The temporal resolution is 5 minutes and the spatial resolution is 3 km. The eigen-images are computed from an observed reflectivity sequence of 15-frame length. Therefore the subspace dimension is 15 and the eigen-images are shown in Fig 34. To simulate the larger spatial scales, the largest five

singular values are weighed more based on the estimated singular values. Specifically, given the estimated singular values, the first five values are scaled by following factors: *1.6, 1.12, 1.09, 1.06, 1.03*, while rest values are kept the same (Fig 35). The seven temporal scales used for this simulation are: *132* minutes, *157* minutes, *189* minutes, *283* minutes, *314* minutes, *471* minutes, *1100* minutes. The simulated sequence of twelve reflectivity images are displayed in Fig 36, and the simulated motion field is shown in Fig 43. This simulation demonstrates that the reflectivity field of larger spatial scales possesses the slower temporal variations.

b. *Simulation 2 – smaller scale reflectivity field with faster variation*

In the second simulation the eigen-images are also obtained using the reflectivity data observed by the KOUN radar on May 16, 2003 (05:26 UTC – 18:16 UTC). A *30*-minute smaller-scale reflectivity sequence is simulated. The temporal resolution is 2.5 minutes and the spatial resolution is 3 km. The eigen-images are computed from an observed reflectivity sequence of 15-frame length. The subspace dimension is 15 and the eigen-images are shown in Fig 37. To simulate the smaller spatial scales, the largest five singular values are weighed less based on the estimated singular values. Specifically, given the estimated singular values, the first five values are scaled by following factors: 0.6, *0.92, 0.94, 0.96, 0.98*, while rest values are kept the same (Fig 38). The seven temporal scales used for this simulation are: *16* minutes, *22* minutes, *28* minutes, *38* minutes, *63* minutes, *314* minutes, *785* minutes. The simulated sequence of twelve reflectivity images are displayed in Fig 39, and the simulated motion field is shown in Fig 44. This simulation demonstrates that the reflectivity field of smaller spatial scales possesses the faster temporal variations.

c. *Simulation 3 – reflectivity field with complex variation*

In the third simulation the eigen-images are obtained using the reflectivity data observed by the KOUN radar on June 5th, 2003 (05:34 UTC – 16:33 UTC). A reflectivity sequence of *60* minutes is simulated. The temporal resolution is 5 minutes and the spatial resolution is 3 km. The eigen-images are computed from an observed reflectivity sequence of 15-frame length. The subspace dimension is 15 and the eigen-images are shown in Fig 40. The singular values in the estimated model are used in this simulation (Fig 41). The seven temporal scales used for this simulation are: *16* minutes, *22* minutes, *31* minutes, *63* minutes, *126* minutes, *943* minutes, *1414* minutes. The simulated sequence of twelve reflectivity images are displayed in Fig 42, and the simulated motion field is shown in Fig 45. This simulation demonstrates an example of the space-time reflectivity fields that possess complex temporal variations.

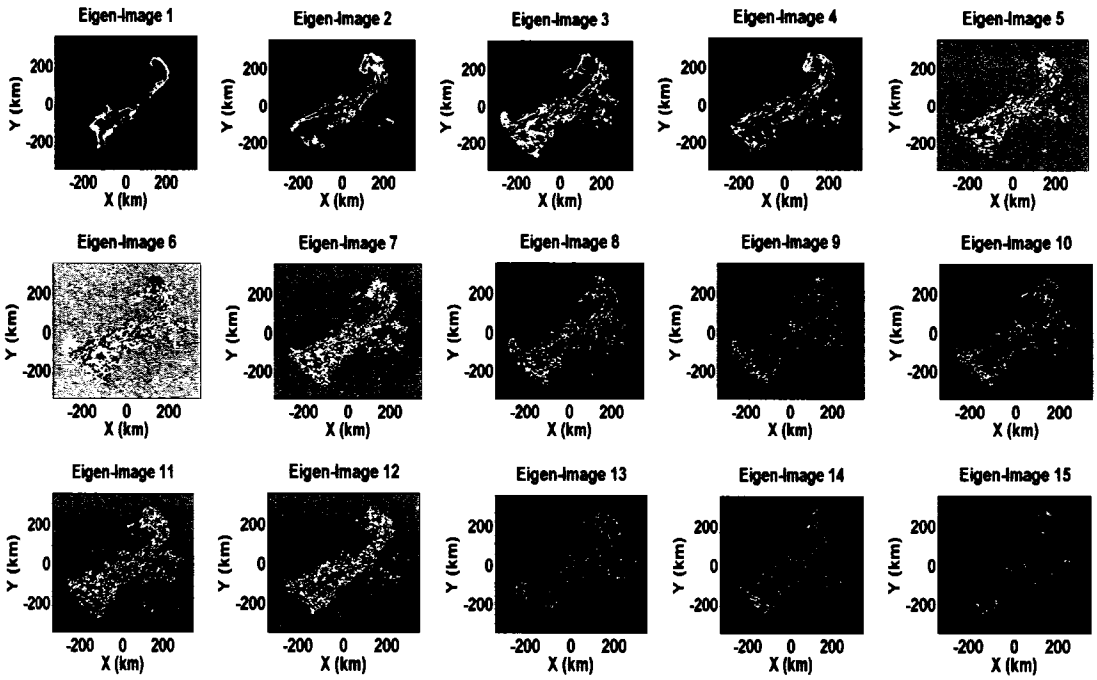

Figure 34. The eigen-images for a short sequence of 15 reflectivity (dBZ) images: these eigen-images are used in simulation 1.

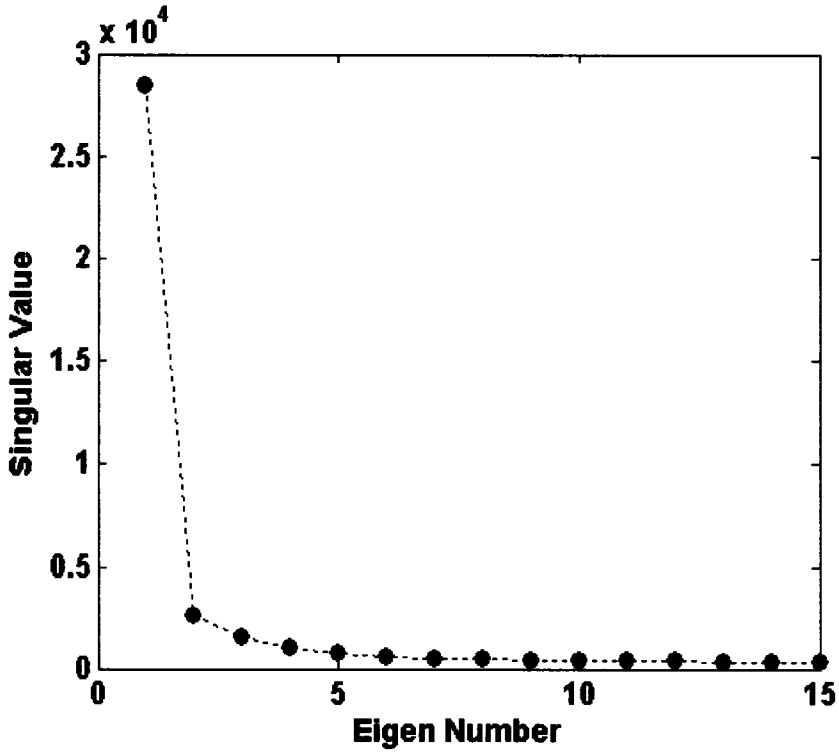

Figure 35. The singular value spectrum used in simulation 1.

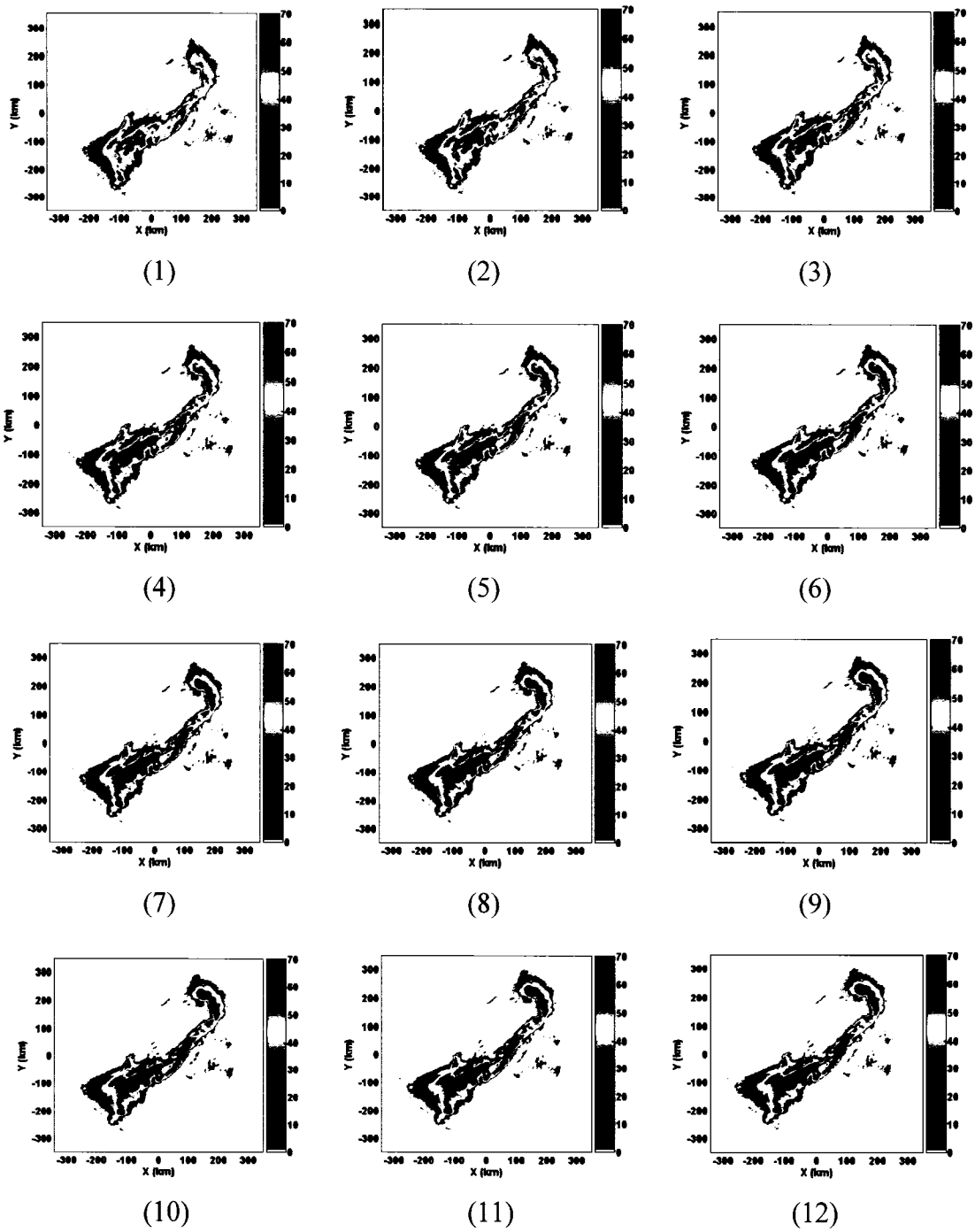

Figure 36. The simulated 60-minute sequence of reflectivity images based on the observed KOUN dataset on June 6th, 2003 (03:40 UTC – 09:59 UTC): the spatial resolution is 3 km and the step interval is 5 minutes.

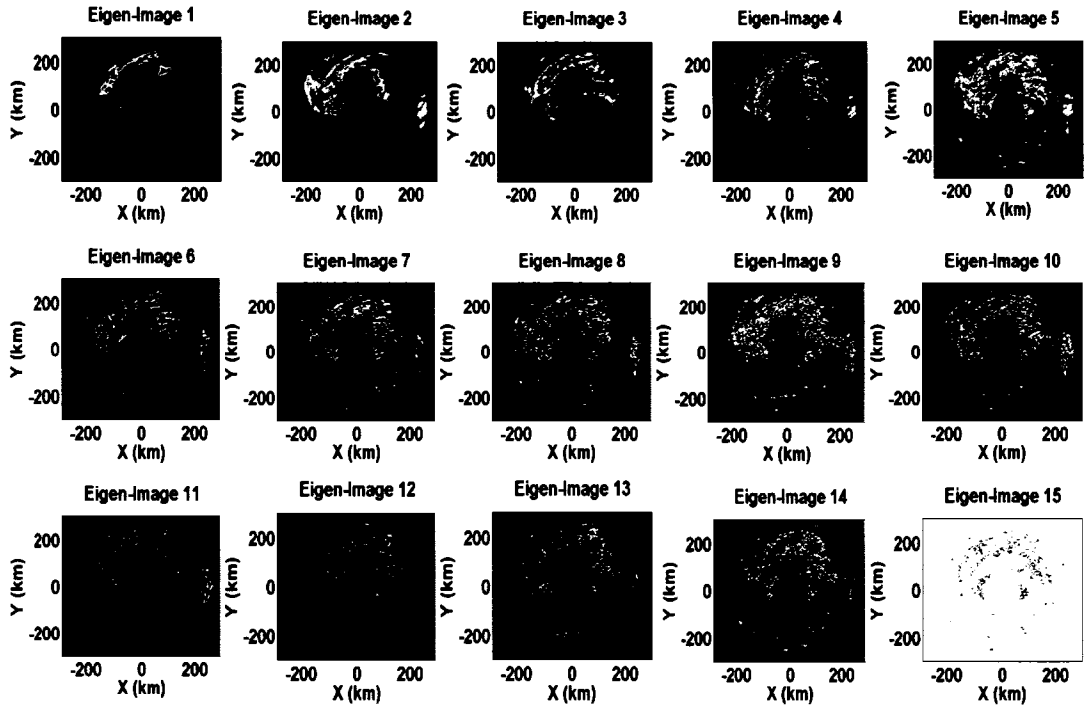

Figure 37. The eigen-images for a short sequence of 15 reflectivity (dBZ) images: these eigen-images are used in simulation 2.

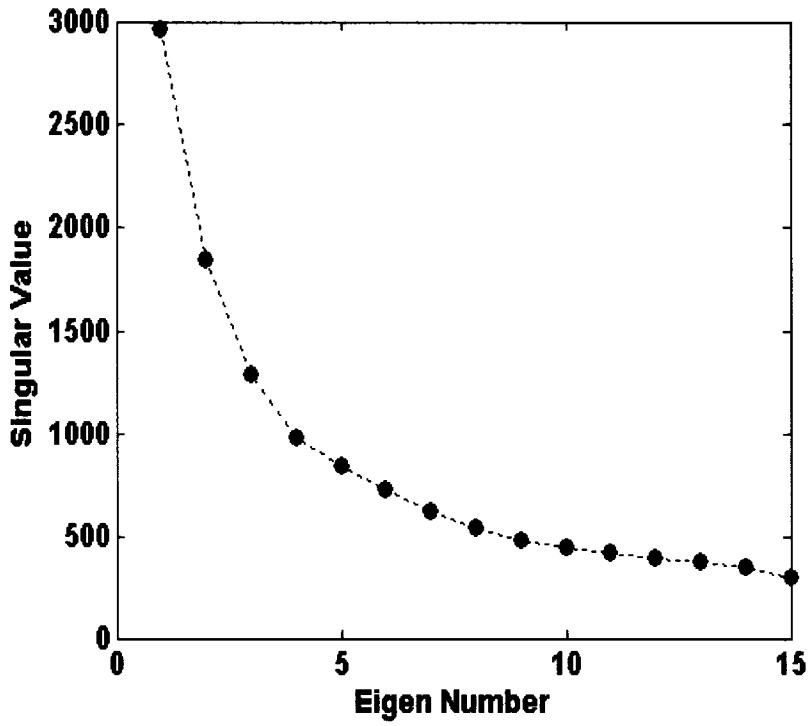

Figure 38. The singular value spectrum used in simulation 2.

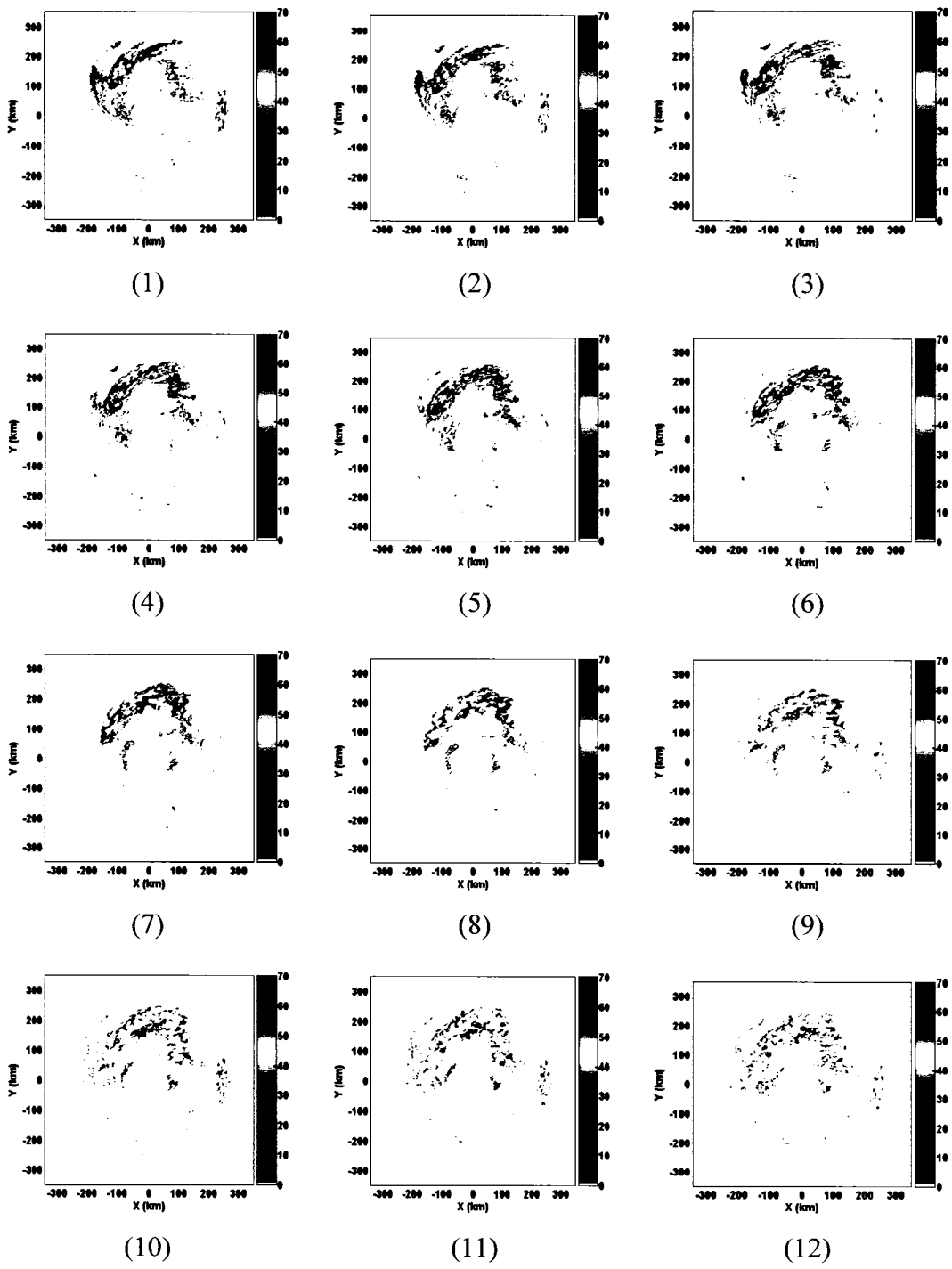

Figure 39. The simulated 30-minute sequence of reflectivity images based on the observed KOUN dataset on May 16, 2003 (05:26 UTC – 18:16 UTC): the spatial resolution is 3 km and the step interval is 2.5 minutes.

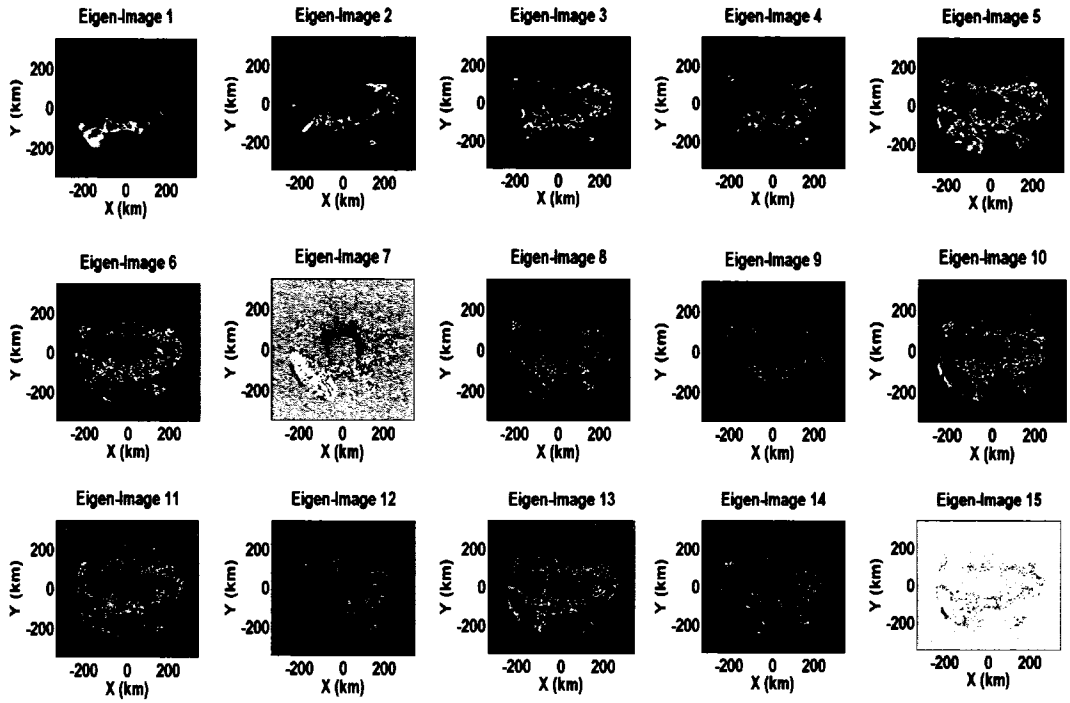

Figure 40. The eigen-images for a short sequence of 15 reflectivity (dBZ) images: these eigen-images are used in simulation 3.

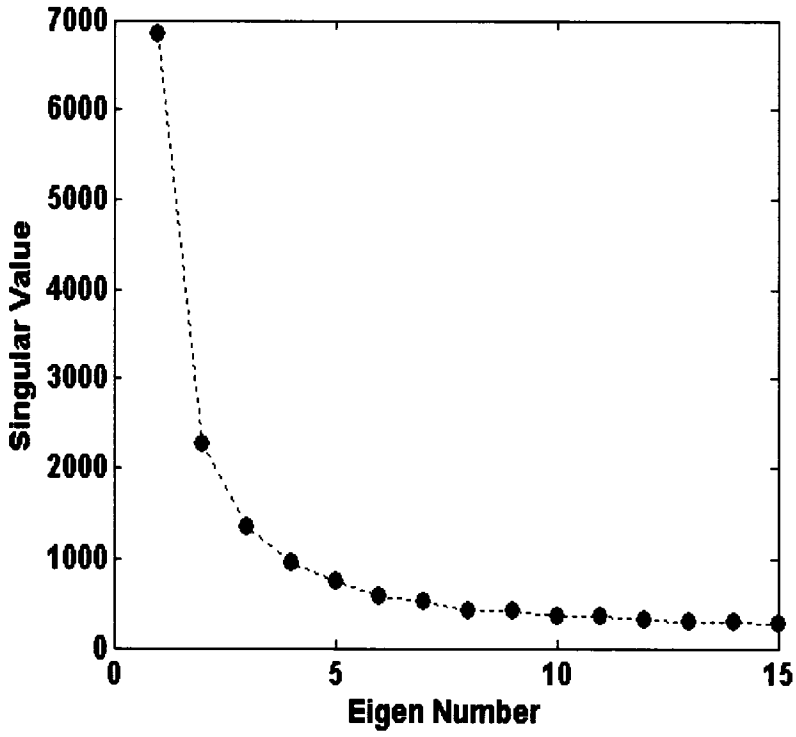

Figure 41. The singular value spectrum used in simulation 3.

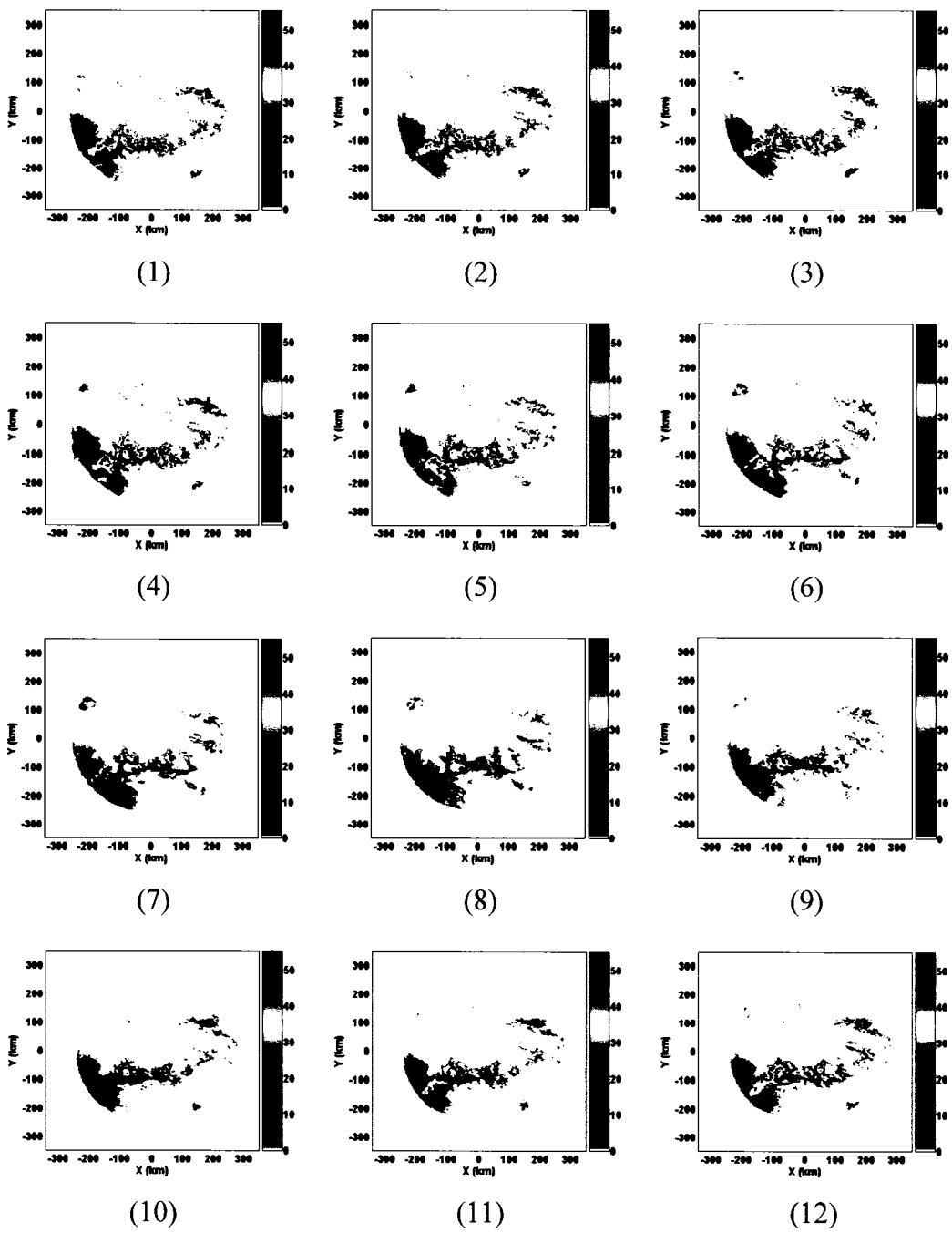

Figure 42. The simulated 60-minute sequence of reflectivity images based on the observed KOUN dataset on June 5th, 2003 (05:34 UTC – 16:33 UTC): the spatial resolution is 3 km and the step interval is 5 minutes.

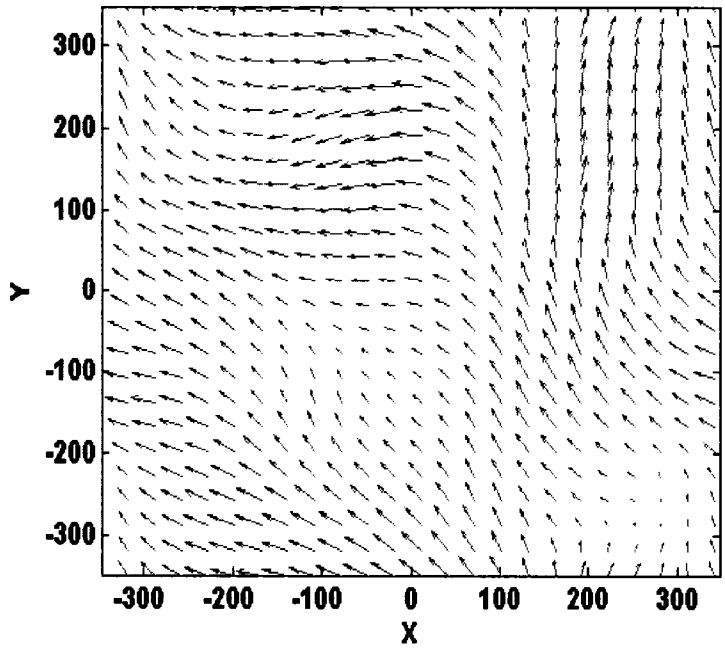

Figure 43. The simulated motion field in simulation 1.

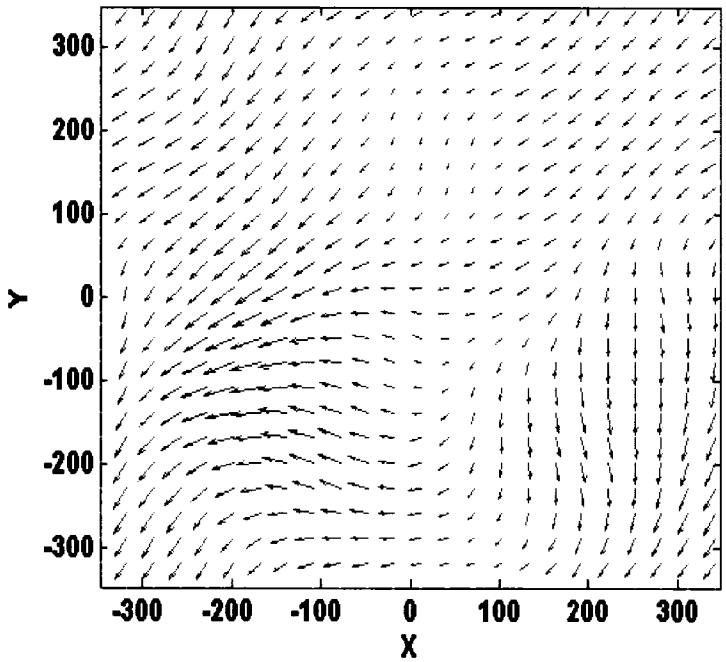

Figure 44. The simulated motion field in simulation 2.

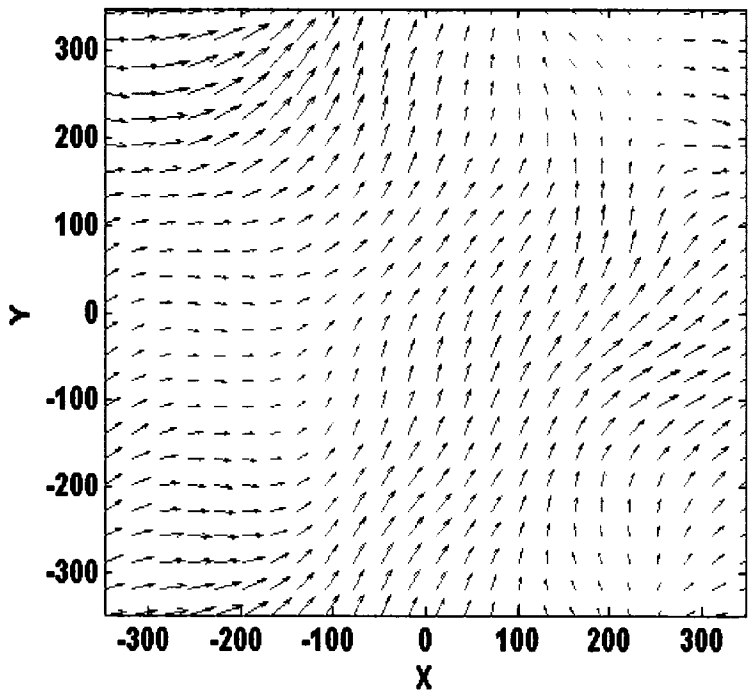

Figure 45. The simulated motion field in simulation 3.

4.4. Multiple Radar Parameters – Differential Reflectivity

The space-time dynamic model developed in this research is limited to the two-dimensional spatial domain since the evolution in the vertical direction is more complicated. Therefore the scope of current studies is restricted to the two-dimensional space, namely, only two-dimensional radar images at a fixed height are used as the input data.

Motivated by compensating the two-dimensional limit of the space-time model developed in current studies, this model is readily extended by using multiple radar parameters rather than using solely reflectivity field. Since the polarimetric Doppler radar technologies have been developed in recent years (Bringi and Chandrasekar, 2001), the dual-polarization parameters, such as the differential reflectivity (ZDR in dB), are available in the routine operation of many weather radar systems. In this section the

spatiotemporal characterization of differential reflectivity (dB) is studied by applying the space-time dynamic model.

As discussed above for reflectivity fields, the spatial model is estimated by the SVD. Eigen-images and singular values for the short sequence of differential reflectivity (dB) are computed. A typical example of eigen-images and singular values is shown in Fig 47. The 10-frame sequence of differential reflectivity images used for computing the SVD is displayed in Fig 46. The further spatiotemporal analysis is conducted on the differential reflectivity of KOUN data over three months in 2003.

In the first analysis, the 14-frame window is employed for each short sequence of differential reflectivity images. The parameters of mean feature vectors for two clusters are shown in Table 6. Table 6 shows that the characteristic time for differential reflectivity fields over three months (KOUN) ranges from few minutes to tens of minutes. It is also seen that the differential reflectivity fields of larger spatial scale possess the larger temporal scales. Comparing Table 6 and Table 5, it reveals that the differential reflectivity tends to have the smaller scales and the faster variations. This indicates that the differential reflectivity tends to characterize the localized variations compared to the reflectivity field.

In the second analysis, 14-frame short sequences of combined reflectivity and differential reflectivity images are used for model estimation. The parameters of mean feature vectors for two clusters are shown in Table 7. Singular-value ratios in Table 7 have the similar values to those in Table 5. The temporal scales of combined reflectivity and differential reflectivity fields tend to be less discriminative for two classes. Compared with Table 5, the largest characteristic time in Table 7 is no longer a dominant

discriminative parameter. These results imply that the differential reflectivity is not a suitable parameter for characterizing the larger scale dynamics and it may have limited discriminative characteristics for the larger scale storms.

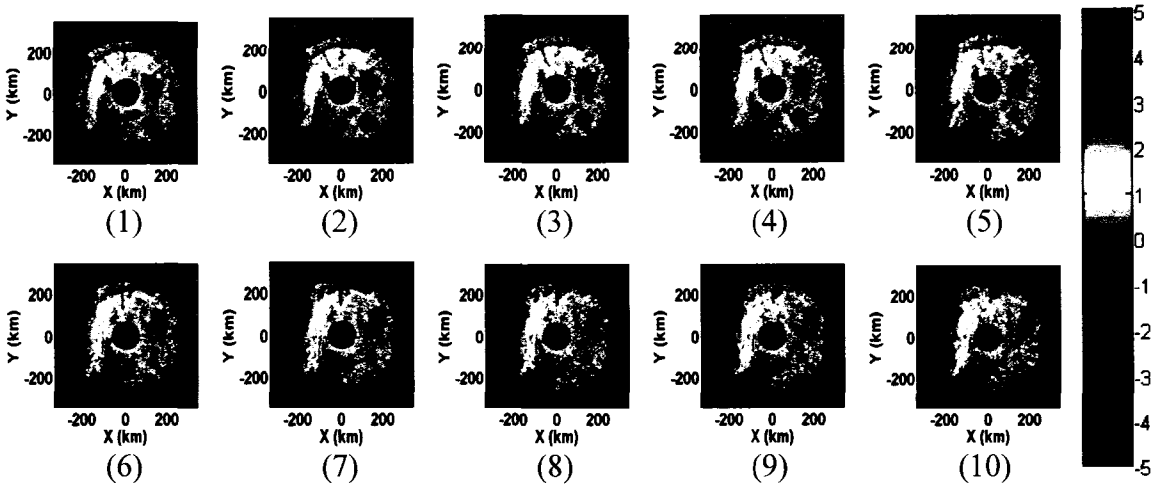

Figure 46. An observed sequence of ten differential reflectivity images (dB). The data was collected by the KOUN radar on April 19th, 2003 (08:10 UTC – 12:11 UTC). The spatial resolution is 3 km and the temporal resolution is approximately 6.5 minutes.

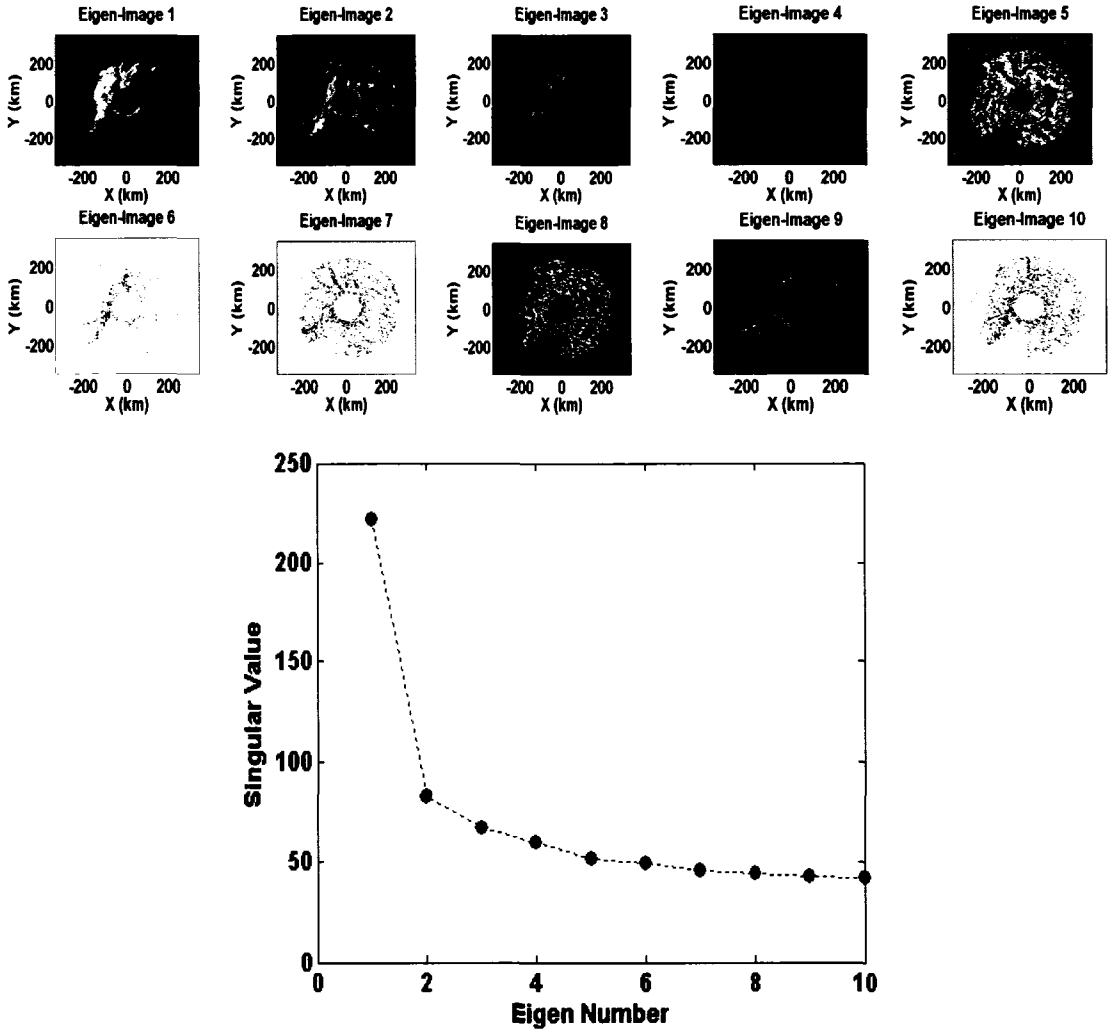

Figure 47. Eigen-images and singular values for observed differential reflectivity images in Fig 46.

Table 6. Characteristic parameters of mean feature vectors for two clusters: model parameters are estimated based on 14-frame windows of differential reflectivity (dB) over three months in 2003 (KOUN). Singular-value ratios are ratios of the maximum value to all values.

Singular-Value Ratios	
Class 1	Class 2
13.30	8.54
12.71	8.17
11.91	7.86
11.59	7.58
11.20	7.32
10.83	6.99
10.34	6.65
9.75	6.21
9.07	5.75
8.39	5.09
7.24	4.48
6.30	3.50
4.52	2.55
1.0	1.0

Characteristic Time (minute)	
Class 1	Class 2
527.5	449.6
115.1	124.7
60.8	67.5
42.8	44.2
29.5	30.8
20.5	21.7
16.1	17.2

Table 7. Characteristic parameters of mean feature vectors for two clusters: model parameters are estimated based on 14-frame windows of combined reflectivity (dBZ) and differential reflectivity (dB) over three months in 2003 (KOUN). Singular-value ratios are ratios of the maximum value to all values.

Singular-Value Ratios	
Class 1	Class 2
21.02	12.77
19.91	12.09
18.94	11.54
17.94	10.95
16.84	10.31
15.47	9.49
14.26	8.74
12.68	7.73
11.05	6.79
9.19	5.65
7.19	4.58
5.23	3.46
3.28	2.26
1.0	1.0

Characteristic Time (minute)	
Class 1	Class 2
1307.4	1353.0
109.9	111.8
54.6	54.3
38.3	38.0
26.8	25.1
20.0	19.0
15.0	14.4

4.5. Summary and Discussion

In this chapter the space-time model is evaluated in detail. Case studies are conducted for space-time analysis of observed radar fields. The procedure for stochastic simulation of reflectivity fields is also developed and described. Several categories of spatiotemporal reflectivity fields are simulated for demonstrating purpose.

The case studies demonstrate the application of the space-time dynamic model on characterizing both spatial and dynamic variability of observed reflectivity fields. The first case study quantified the characteristic temporal scales for the reflectivity data collected by the KOUN radar during April, May and June in 2003. For the KOUN dataset of three months, the second case study demonstrated that the model with mean reflectivity-field removed possesses only the smaller temporal scales, compared with the model without removing the mean reflectivity-field. These results are consistent with previous findings by other researchers (Wilson et al 1998; Germann and Zawadzki 2002). New contributions in the current research are: 1) the space-time dynamic model that provides a general framework for analyzing and quantifying the spatiotemporal characteristics of observed radar fields; 2) the estimated space-time model and parameters that may have various applications, such as the classification and the stochastic simulation, and 3) the classification based on both spatial characterization and dynamic characterization. The procedure developed in this research for stochastic simulation of reflectivity fields over space and time is also new. The simulation procedure is data-driven, simple and effective.

CHAPTER V. SPACE-TIME MODELING OF RADAR OBSERVATIONS – SHORT-TERM PREDICTION

5.1. Model Estimation and Validation

In chapter three it is shown that the storm motion is a special application of the linear state-space model for space-time radar observations. The motion can be modeled as a linear flow matrix in the sub-state-space. It has been demonstrated in both theory and experiment that the motion flow matrix is a real skew-symmetric matrix. Empirical studies in chapter three also revealed that the storm motion may be described by the interactions between neighboring eigen-components of similar scales. This is generalized as an assumption: *both storm motion and evolution processes may be modeled by the interaction between fewer neighboring empirical eigen-components.* To model both storm motion and evolution, the linear map $\mathbf{F}_t$ in Eq 3.27 is therefore assumed to have the band diagonal structure (Eq 5.1). It is found by experiments that the nearest two neighboring elements to the diagonals are sufficient for modeling space-time radar reflectivity fields.

$$\mathbf{F}_t = \begin{bmatrix} F_{11} & \ddots & 0 & 0 & 0 \\ \ddots & \ddots & \ddots & 0 & 0 \\ 0 & \ddots & \ddots & \ddots & 0 \\ 0 & 0 & \ddots & \ddots & \ddots \\ 0 & 0 & 0 & \ddots & F_{nn} \end{bmatrix} \tag{5.1}$$

In this study the observed radar reflectivity was collected by the WSR-88D radar (Melbourne, FL) during the storm event from 2102 UTC, 23 August to 0057 UTC, 24

August in 1998. This temporal sequence of radar images spans approximately four hours. The WSR-88D radar takes approximately five minutes to finish a volume scan. Each volume of PPI scans was interpolated to generate the CAPPI data in Cartesian coordinates. The interpolated 2D reflectivity images at the height of 1 km above the ground are used in this study. The re-sampled radar images are in the two-dimensional region: -50 km $\leq$ x, y $\leq$ 50 km. The spatial sampling interval is 1 km on both x-axis and y-axis and the temporal interval is approximated 5 minutes. Therefore we obtain a sequence of forty-eight radar images that are regularly sampled on time. The spectral tracking algorithm is applied to each six successive reflectivity images for motion estimation.

We test the validity of the linear dynamic model in the subspace by evolving the state vector at time "t" for the next 18 steps. Matrix $\mathbf{F}_t$ is estimated by the least-square (LS) method (Stark and Woods 1994; Ljung 1998). The SVD is computed using 10 history images and 24 future images (from "t – 10" to "t + 24"). $\mathbf{F}_t$ is estimated by using only the 10 history images (from "t – 10" to "t"). The estimated linear dynamic model is then applied to forecasting the next 18 state vectors, which are used to reconstruct reflectivity images. Nowcasting scores (CSI, POD and FAR) are evaluated by comparing forecast images with observed images at each lead step. The averaged scores compared with the tracking-based extrapolation are shown in Fig 48. The tracking-based extrapolation is obtained by the advection of the observed images using the motion field estimated by the spectral algorithm. Fig 48 reveals the relative impact of motion field and dynamic evolution on the non-stationary variation of radar reflectivity fields. It demonstrates that the dynamic model can significantly improve the modeling performance.

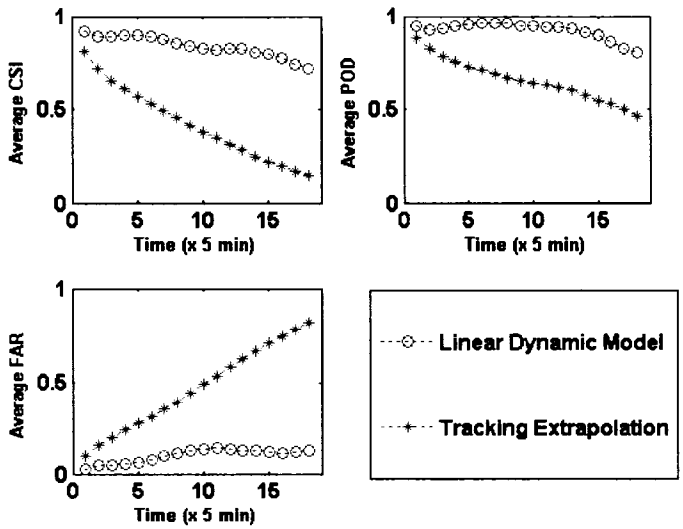

Figure 48. Comparison of nowcasting scores for linear dynamic model and tracking based extrapolation. The linear dynamic model implicitly includes both storm motion and evolution. The scores are averaged over all results at the same lead time. Definitions of nowcasting scores (CSI, POD and FAR) are given in Eq 2.10, Eq 2.11 and Eq 2.12.

5.2. Extrapolative Least-Square Vector Auto-Regression (LS-VAR) Model

Multivariable autoregressive models have been successfully applied to the idetentification and prediction of dynamic systems (Ljung 1998). In this section the procedure to estimate the Vector Auto-Regressive model for short-term radar reflectivity prediction is developed. It is applied to multiple-step extrapolative predictions via recursions.

a. *Model identification by Least Square Vector Auto-Regression (LS-VAR)*

For a fixed time "*t*", based on the spatial model using the *SINC*-kernel functions, each reflectivity image is converted to a data vector consisting of pixel values. A sequence of data vectors from radar measurements can be concatenated to construct a super-vector (Eq 3.9). A temporal sequence of super-vectors is collected for computing the SVD as described by Eq 3.20. Subsequently by applying the projection operator $\mathbf{P}_S \equiv \mathbf{S}^{-1}\mathbf{U}^T$ on

all super-vectors we can estimate a sequence of state vectors. We assume the state vector evolves according to Eq 3.25, where $\mathbf{F}_t$ is the unknown transition matrix that links two consecutive state vectors. For the sequence of estimated state vectors, $\mathbf{F}_t$ is set to be a constant matrix, which has the diagonal band structure (Eq 5.1) to respect the assumption that only the interactions between neighboring eigen-basis contribute to storm motion and evolution.

All $\{F_{ij}\}$ coefficients within the diagonal band are unknown parameters that are to be estimated using the estimated sequence of state vectors. Given an auto-regressive model as above, parameters $\{F_{ij}\}$ can be estimated by the least-square algorithm (Ljung 1998). Through the experimenting, it was found that, the best modeling results can be achieved when the neighboring number for diagonal band in $\mathbf{F}_t$ is fixed to two. As the neighboring number is increased, either we lack sufficient data for estimation, or the output of models in recursive prediction becomes noisy due to large variances for estimated parameters.

Several important details for the modeling and predicting procedure are elaborated here. To increase modeling data points and reduce discretization error, the sampling sequence is firstly interpolated on time using the *SINC*-interpolations. Due to the storm motion, signals at some future locations on radar scan may be missing. To properly extend the span of eigen-images for compensating the lost signals, the last image is extrapolated some steps forward using the estimated motion field. The extrapolated sequence is combined with the history data for computing the SVD. Furthermore, extrapolating the last image and computing the SVD are carried out for each single step in recursive predictions, and predicted images are adaptively incorporated into the history

sequence for model estimation. The detailed algorithmic procedure for the extrapolative LS-VAR nowcasting is outlined below.

Algorithmic procedure (LS-VAR modeling and extrapolative predicting):

1: Choose the most recent history sequence of radar images (reflectivity dBZ) for modeling and predicting (11 history images are used in current studies).

2: Interpolate radar images between sampling points on time using the SINC method (12 discrete steps are interpolated within each sampling interval in current studies).

3: Construct concatenated super-vector using successive 12-step images, and the sequence of super-vectors are constructed by sliding forward 12-step window one step a time. Assign this sequence to both the SVD-sequence and the model-sequence. The SVD-sequence is the sequence used for the SVD computation. The model sequence is the sequence used for the VAR-model estimation.

4: The last image is extrapolated, one step a time, using the estimated motion field, up to the time point of 12 sampling intervals forward.

5: Construct the super-vector sequence for extrapolated images using the same method as described in step 3. Combining this sequence with the above SVD-sequence gives the updated SVD-sequence.

6: Compute the SVD of the matrix formed by collecting all vectors in the SVD-sequence. Construct subspace representation as described by Eqs 3.18, 3.20 *and* 3.21.

7: Project all vectors in the model-sequence into the subspace to create the state-vector sequence. Using this state-vector sequence, estimate the linear mapping matrix, as given in Eq 5.1, by the least-square algorithm.

8: Recursively applying the estimated VAR model, starting from the last state vector in the state-vector sequence, one step a time, for 12 steps forward. At each step, the super-vector is reconstructed using the pseudo-inverse of projection matrix (Eq 3.21*) and the predicted state-vector. At the last step, the predicted image that is extracted from the predicted super-vector is added to the last image.*

9: Combining the model-sequence with the predicted super-vector sequence gives the updated model-sequence.

10: Go to step 4 and loop for 12 times, giving the forecast images up to 12 sampling intervals ahead (each sampling interval is approximately 5 minutes for the dataset in current studies).

b. *Short-term prediction and evaluation*

The modeling and predicting procedure outlined above has been applied to the observed image sequences from the WSR-88D radar (Melbourne, FL 1998). In this dataset only radar reflectivity is available and the super-vector is constructed by concatenating the delayed images as described above. In the LS-VAR extrapolative prediction, the motion extrapolation is conducted to obtain the reflectivity images in future locations. The Spectral Algorithm developed in chapter three is used for the motion estimation and extrapolation.

The whole data sequence consists of totally forty-eight images and the sampling interval is approximately five minutes. The extrapolative predictions based on LS-VAR

models are conducted for 1 – 12 sampling intervals, corresponding to 0 – 1 hour of lead time. Predicting skills are measured by CSI (critical success index), POD (probability of detection) and FAR (false alarm rate), which are defined in Eqs 2.10, 2.11 and 2.12. These scores are computed using a single threshold level (25 dBZ) with 4 km × 4 km neighboring grid size. The scores are averaged over all predictions, each of which is obtained by fixing a reflectivity image as the last image. The average is computed over the predictions by setting the last image from twenty to thirty-six. The comparisons of nowcasting scores between the LS-VAR model and the motion-based extrapolations are shown in Figs 49, 50 and 51. The results show that the extrapolative prediction based on the subspace VAR model performs well. It offers a promising model for the short-term forecast because of its capability to model both the storm motion and the dynamic evolution.

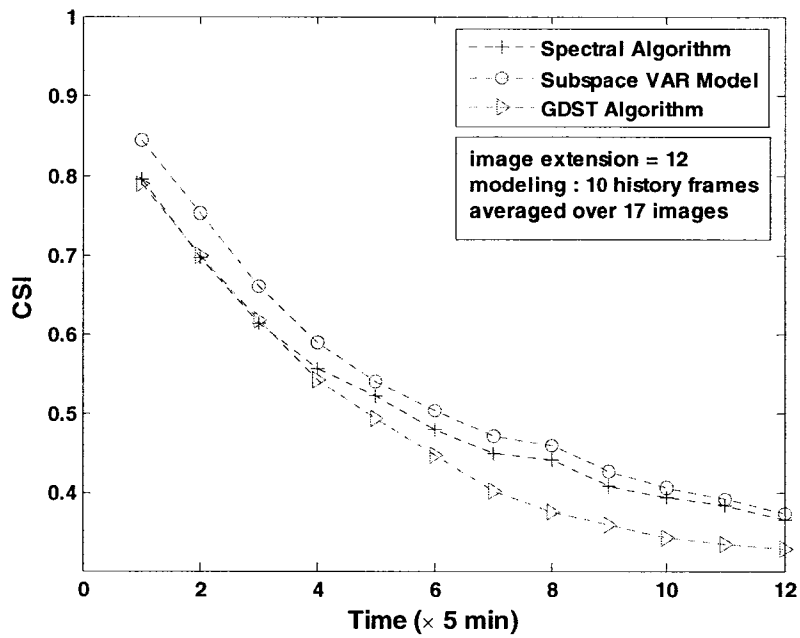

Figure 49. Comparison of CSI between the extrapolative LS-VAR model and the motion extrapolations based on 1) Spectral Algorithm and 2) Growth-Decay Storm Tracker (GDST).

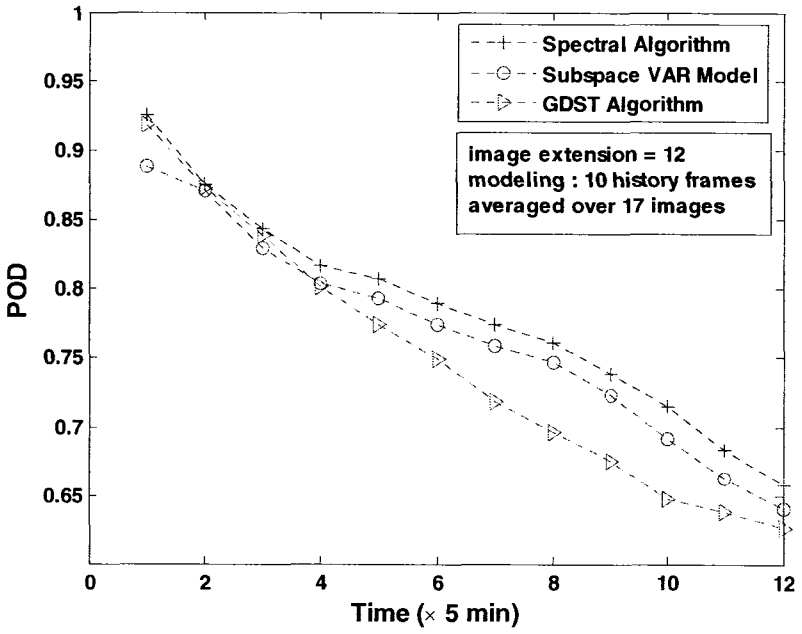

Figure 50. Comparison of POD between the extrapolative LS-VAR model and the motion extrapolations based on 1) Spectral Algorithm and 2) Growth-Decay Storm Tracker (GDST).

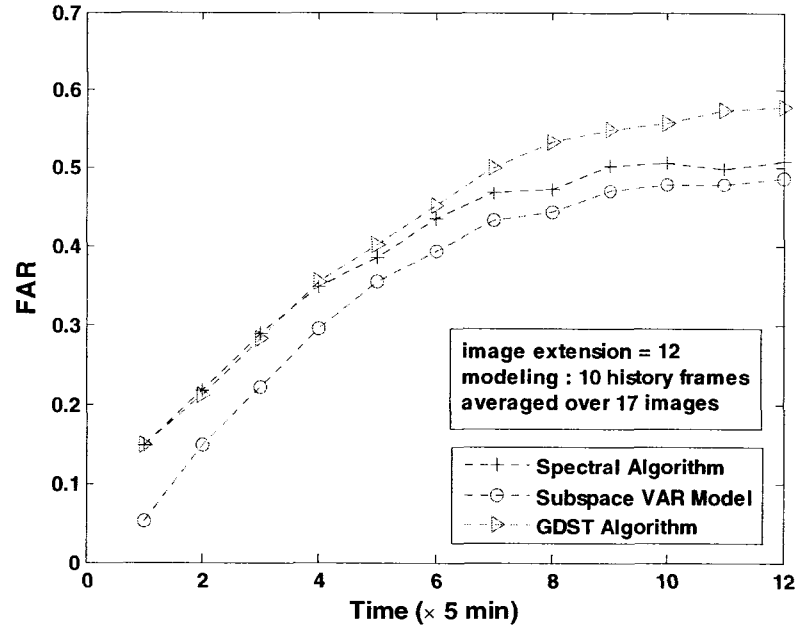

Figure 51. Comparison of FAR between the extrapolative LS-VAR model and the motion extrapolations based on 1) Spectral Algorithm and 2) Growth-Decay Storm Tracker (GDST).

c. *A metric distance based interpretation*

As discussed above a reflectivity image can be represented by a vector consisting of all pixel values. Generally the vector belongs to the high-dimensional Euclidean space. In the subspace dynamic model, the predicted reflectivity image belongs to the low-dimensional subspace. The subspace is optimal in the sense that all history images can be represented in this subspace with the least squared errors. This subspace is computed by the SVD, as discussed previously. Given a sequence of t history reflectivity images, the optimal prediction for the next image at $t+1$ can be defined as the subspace vector that minimizes the distance between the predicted image and the next observed image (Fig 52).

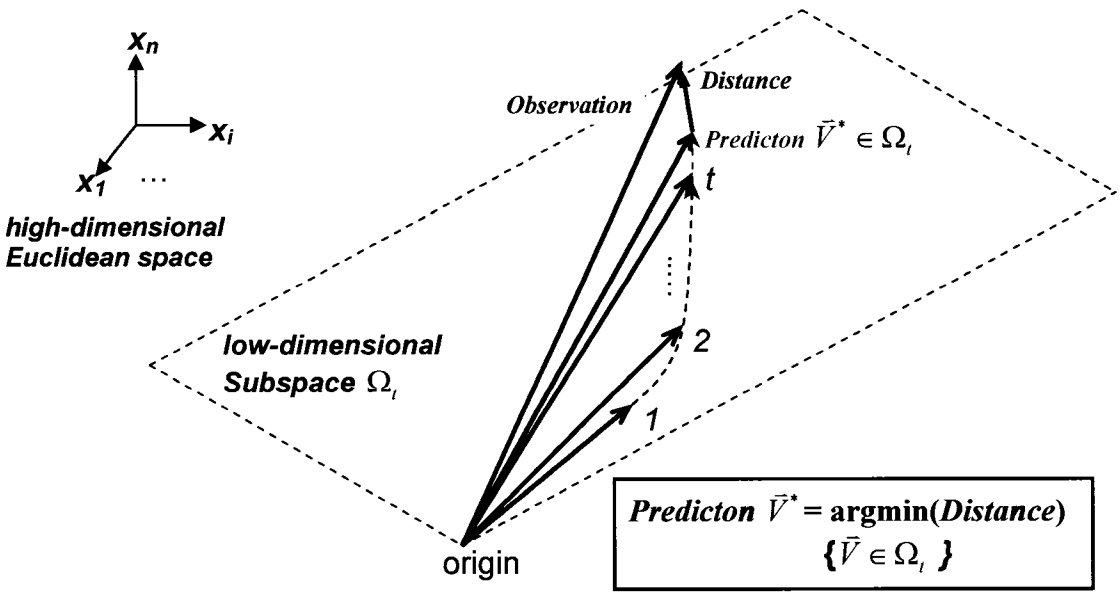

Figure 52. A metric distance interpretation of the short-term prediction for reflectivity images.

The above interpretation suggests that the distance measure in the Euclidean space can be used to quantify the predicting skills of a given algorithm. Recently Mielke and Berry (2001) have developed a non-parametric approach to measure the agreement between multiple blocks based on the generalized distance function (Mielke and Berry

2001). In current studies the multivariate randomized block permutation procedure (MRBP) (Mielke and Berry 2001) is adopted to quantitatively measure the similarity between the predicted reflectivity images and the observed reflectivity images. For our purposes the two-block permutation test is applicable here. Given a set of predicted reflectivity images (block 1) and the corresponding observed images (block 2), the MRBP statistic based on the Euclidean distance is given by

$$\delta = \frac{1}{g}\sum_{i=1}^{g}\Delta(\mathbf{v}_i, \mathbf{v}_i') \tag{5.2}$$

where g is number of prediction-observation pairs, and $\Delta(\mathbf{v}_i, \mathbf{v}_i')$ is the Euclidean distance between the predicted vector $\mathbf{v}_i$ in block 1 and the corresponding vector $\mathbf{v}_i'$ in block 2. To measure the similarity between the predictions and the observations, the *P*-value is defined as the probability that the value of δ is smaller than the observed value, δ_0, given randomized within-block permutations. Therefore the smaller the δ_0 or the *P*-value is, the better the agreement is between the predicted images and the observed images.

Table 8. An Alternative Evaluation using the Multivariate Randomized Block Permutation (MRBP).

	Extrapolative-VAR			Spectral Algorithm			GDST Algorithm		
Step	***P*-value**	δ_0	R_0	***P*-value**	δ_0	R_0	***P*-value**	δ_0	R_0
1	0.29E-12	101.73	0.76	0.30E-11	161.87	0.64	0.75E-11	163.65	0.63
2	0.72E-11	188.62	0.56	0.14E-09	232.12	0.49	0.33E-09	225.79	0.50
3	0.15E-09	243.13	0.45	0.13E-08	278.83	0.40	0.45E-08	271.63	0.40
4	0.90E-09	278.93	0.38	0.49E-08	312.28	0.34	0.33E-07	306.19	0.33
5	0.27E-08	304.68	0.33	0.95E-08	336.48	0.29	0.20E-06	335.04	0.27
6	0.33E-08	320.43	0.30	0.88E-08	354.73	0.27	0.82E-06	359.71	0.23
7	0.35E-08	333.05	0.28	0.78E-08	369.16	0.25	0.31E-05	381.20	0.19
8	0.34E-08	344.35	0.26	0.65E-08	381.56	0.23	0.12E-04	399.13	0.16
9	0.53E-08	354.76	0.24	0.10E-07	392.00	0.21	0.60E-04	414.13	0.13
10	0.28E-07	365.45	0.22	0.47E-07	401.78	0.19	0.24E-03	423.98	0.11
11	0.15E-06	374.96	0.20	0.18E-06	409.17	0.18	0.75E-03	430.84	0.10
12	0.10E-05	384.43	0.18	0.80E-06	415.61	0.16	0.22E-02	436.44	0.08

The distance based permutation test is conducted on the short-term predictions obtained in the previous section. Results are shown in Table 8. Table 8 contains the *P*-value and the obaserved measure of agreement R_0, given by

$$R_0 = 1 - \frac{\delta_0}{\mu_\delta} \tag{5.3}$$

where μ_δ is the exact mean of δ under the permutation distribution (Mielke and Berry 2001). Perfect agreement exists when $R_0 = 1$, random agreement occurs when R_0 is close to 0, and disagreement occurs when R_0 is distinctly less than 0. The results in Table 8 demonstrate that the LS-VAR model consistently outperformed the motion-tracking based algorithms.

The metric distance based interpretation and the permutation test based statistical scores, such as the *P*-value and the agreement measure R_0 that are presented in Table 8, give the conceptually simple and more rigorous assessment of the forecasting performance. The traditional nowcasting scores such as CSI, POD and FAR shown in Figs 49, 50 and 51 have the difficulties to accurately quantify the performance of three algorithms. In contrast the *P*-values in Table 8 have shown the significant differences among the three algorithms and these differences are consistently verified by the agreement measurement R_0. Therefore the statistical scores that are based on the metric distance and the permutation test provide the more accurate assessment on the forecasting performance of different algorithms.

d. *Kalman filtering and predicting*

The Kalmn filtering and predicting is a standard technique (Kalman 1960; Appendix C). To complete the evaluation of nowcasting performance, the LS-VAR model is further compared with the Kalman filtering and predicting. In current studies the random walk model with the white Gaussian noise is used for the Kalman filter. The nowcasting scores (CSI, POD and FAR) for the extrapolative LS-VAR model, the Kalman filter and the motion extrapolation based algorithms are shown in Figs 53, 54 and 55. It is seen that the Kalman filter has the higher false alarm rate and the higher detection rate. Overall the subspace LS-VAR model demonstrates the higher CSI scores than the Kalman filter.

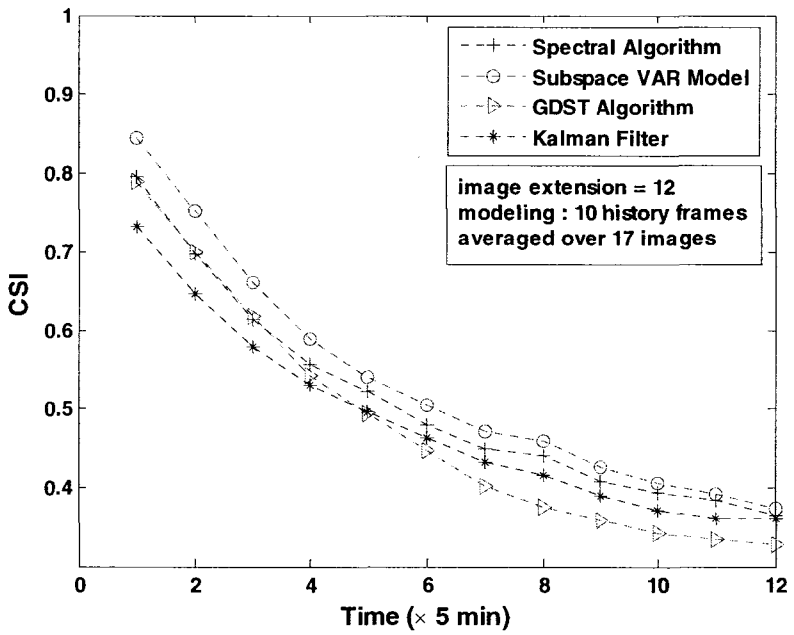

Figure 53. Comparison of CSI between the extrapolative LS-VAR model, the motion extrapolation based on Spectral Algorithm, the motion extrapolation based on Growth-Decay Storm Tracker (GDST) and the Kalman Filter using the WSR-88D radar data (Melbourne, FL 1998).

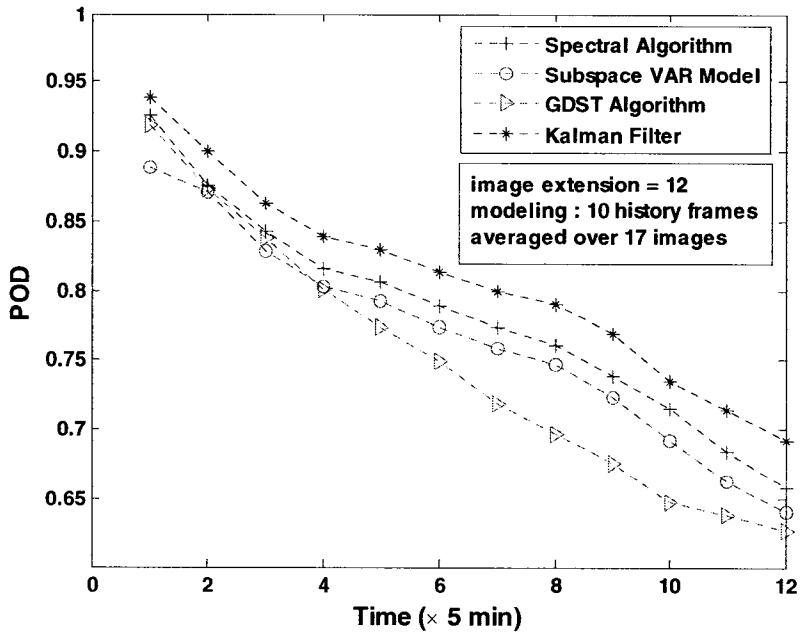

Figure 54. Comparison of POD between the extrapolative LS-VAR model, the motion extrapolation based on Spectral Algorithm, the motion extrapolation based on Growth-Decay Storm Tracker (GDST) and the Kalman Filter using the WSR-88D radar data (Melbourne, FL 1998).

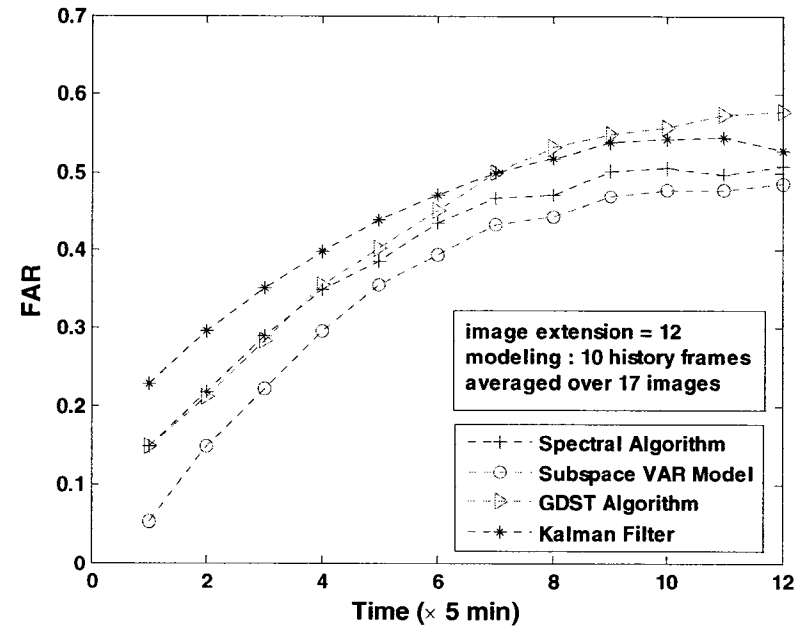

Figure 55. Comparison of FAR between the extrapolative LS-VAR model, the motion extrapolation based on Spectral Algorithm, the motion extrapolation based on Growth-Decay Storm Tracker (GDST) and the Kalman Filter using the WSR-88D radar data (Melbourne, FL 1998).

5.5. Summary and Discussion

The application of the space-time dynamic model on the short-term prediction has been developed and studied in the current research. Using the observed reflectivity data from the WSR-88D radar (Melbourne, FL 1998), it has been demonstrated that the dynamic model can significantly improve the modeling performance by including both the storm motion and evolution. For the short-term prediction, the extrapolative least-square vector auto-regression (LS-VAR) has been developed and evaluated using the same set of reflectivity data from the WSR-88D radar. To measure the similarity between the predicted images and the observed images, a metric distance based permutation test has been adopted in current studies. Both conventional nowcasting scores (CSI, POD and FAR) and the distance-based permutation test revealed that the extrapolative LS-VAR model outperformed the tracking-only based algorithms, namely, the spectral tracking algorithm and the GDST algorithm. The nowcasting scores using the LS-VAR model are further compared with the Kalman filter based predictions.

CHAPTER VI. SUMMARY AND RECOMMENDATIONS FOR FUTURE WORK

6.1. Summary and Conclusions

A general framework of the dynamic model for space-time radar observations has been developed in the current research. Three difficulties in modeling space-time radar observations have been addressed: 1) high dimensionality due to the high-resolution radar measurements over a large area, 2) non-stationarity due to the storm motion, and 3) non-stationarity due to the dynamic evolution (growth and decay).

To deal with the storm motion, a novel and efficient radar storm tracking algorithm is developed in the spectral domain. Based on this new technique, the Dynamic and Adaptive Radar Tracking of Storms (DARTS) is developed and evaluated. Using the synthesized radar reflectivity images, the observed reflectivity data from the WSR-88D radar (Melbourne, FL 1998), the observed reflectivity data from the KOUN radar (Norman, OK 2003) and the observed reflectivity data from the CASA IP1 radars (OK 2006), the performance of the spectral tracking and nowcasting has been extensively evaluated. The spectral tracking algorithm has demonstrated good and robust performance and it offers a new promising technique for radar storm tracking and extrapolating. The software has been implemented in C language for DARTS algorithms. Using dynamic simulations it is demonstrated that the DARTS system is feasible for the real-time applications in the high temporal resolution (30 seconds).

To tackle the high dimensionality and model the spatial variability of radar observations, a general modeling framework is formulated and the singular value decomposition (SVD) is used for dimension reduction. To deal with the dynamic evolution and model the temporal variability of radar observations, the motion-compensated temporal alignment (MCTA) transformation is developed. In this analysis the evolution of radar storm fields is modeled by the linear dynamic system (LDS) in the low-dimensional subspace. As a special application the storm motion can be represented by a linear flow matrix in the LDS. The theoretical results of the linear flow matrix have been obtained and been verified by empirical studies using the data from the WSR-88D radar (Melbourne, FL 1998).

Several case studies have been conducted to demonstrate the application of the dynamic model on characterizing both spatial and dynamic variability of observed radar fields. Spatial and dynamic characteristics are obtained based on the estimated model parameters using three months of observations from the KOUN radar (Norman, OK 2003). The first case study quantified the characteristic temporal scales for the reflectivity data collected by the KOUN radar during April, May and June in 2003. In general the characteristic time for the reflectivity field ranges from tens of minutes to hundreds of minutes, while the characteristic time for the differential reflectivity tends to be smaller. For the KOUN dataset of three months, the second case study demonstrated that the model with mean reflectivity-field removed possesses only the smaller temporal scales, compared with the model without removing the mean reflectivity-field. These results are consistent with the previous findings by other researchers (Wilson et al 1998; Germann and Zawadzki 2002). In general the storms of the larger spatial scales possess

the larger temporal scales. The procedure for the stochastic simulation of reflectivity fields based on the space-time dynamic model has also been developed. The simulation procedure is data-driven, simple and effective. Several types of spatiotemporal reflectivity fields are simulated for demonstration purpose. New contributions of the current research are: 1) Development of space-time dynamic model to provide a general framework for analyzing and quantifying the spatiotemporal characteristics of observed radar fields; 2) estimation of space-time model and parameters for various applications, such as the classification, the stochastic simulation, and setting up the optimal radar sampling; and 3) classification procedure based on both spatial characterization and dynamic characterization is also developed. A new procedure is developed for the stochastic simulation of reflectivity fields.

The application of the space-time dynamic model on the short-term prediction has been developed and studied. Using the observed reflectivity data from the WSR-88D radar (Melbourne, FL 1998), it has been demonstrated that the model developed here can significantly improve the prediction performance by including both the storm motion and evolution. For the short-term prediction, the extrapolative least-square vector auto-regression (LS-VAR) has been developed and evaluated using the same set of reflectivity data from the WSR-88D radar. To measure the similarity between the predicted images and the observed images, a metric distance based permutation test has been adopted in current studies. Both conventional nowcasting scores (CSI, POD and FAR) and the distance-based permutation test revealed that the extrapolative LS-VAR model outperformed two tracking-only based algorithms, namely, the spectral tracking algorithm and the GDST based algorithm.

To model the space-time variabilities of weather radar observation, comprehensive studies have been conducted in the current research. A novel spectral tracking algorithm and the DARTS nowcasting system have been developed and evaluated. A general modeling framework is formulated and the application of this framework to storm classification and stochastic simulation has been developed. The extrapolative LS-VAR model for the short-term prediction has been developed and evaluated by comparing with other algorithms, including the Kalman filtering based prediction. Evaluation of the space-time variability is particularly important in the context of adaptive scanning of storm systems. Therefore the system approaches and various techniques developed in this research can be of great use for designing the adaptive scanning systems that are used in the CASA project.

6.2. Recommendations for Future Work

The general framework of the dynamic model and the techniques developed in the current research opens many interesting topics on modeling the space-time radar observations and the applications.

In the current study it is demonstrated that the motion-flow model has led to an efficient tracking and nowcasting algorithm. In chapter two only the storm motion has been explicitly modeled by the advection terms. Storm motion field as the parameters in advection terms can be efficiently estimated in the spectral domain. Other physical mechanisms are implicitly modeled in the evolution term. The extension of motion flow model may lead to the more complete models by explicitly incorporating other physical mechanisms beyond the motion flow. This could be done by combining motion flow model with other physically based parametric models to include such mechanisms as the

turbulent diffusion or the storm growth and decay. Essentially it would be desirable to explicitly model the important mechanisms such as the storm growth and decay, whose parameters may be estimated based on the observational data.

It is demonstrated that the DARTS system based on the spectral tracking algorithm performs fairly well for the short-term nowcasting, when compared with the GDST based algorithm. All the case studies in the current research have been conducted on the rainfall or subtropical storm data. It would be favorable to further extend the current studies to other types of storms, such as the snow storms. In general the winter snow storms would show the less movement and the more uniform reflectivity field, as compared with tropical rainfall storms. It would be beneficial to use winter storm data to test the spectral tracking algorithm, and reveal its advantages as well as its limitations for radar storm tracking and nowcasting.

The linear dynamic system (LDS) has been used in current studies for modeling the subspace dynamics. This is mainly due to its simplicity and the closed-form solutions. A direct extension of this model would be to use the non-linear dynamic system (NLDS) model. The main challenge for the NLDS model is to determine the functional mapping because the form of the function is not specified. One plausible solution to this is to use the non-linear system identification techniques that are discussed in Ljung 1998.

Concerning the application of the dynamic model on the space-time characterization of radar observations, multiple radar parameters beyond the reflectivity (dBZ) and the differential reflectivity (dB) may be used. It would be beneficial to experiment on other radar parameters, such as the Doppler velocity, to study the space-time characterization. This would be conducive to understanding the spatiotemporal properties of different

radar observations. The major improvement will come by extending the model to three dimensions and including the vertical variability of storms.

REFERENCES

Adelson, E. H. and J. R. Bergen, 1985: Spatiotemporal energy models for the perception of motion. *Journal of Optical Society of America (A)*, **2**, 284-299.

Austin, G. L. and A. Bellon, 1982: Very-short-range forecasting of precipitation by the objective extrapolation of radar and satellite data. *Nowcasting*, A. K. Browning, Ed., Academic Press, 177-190.

Batail, E., 2002: Statistical Models for rainfall: characterisation and forecasting. *MSc Thesis*, Research in Pattern Analysis and Neural Networks, Aston University.

Beauchemin, S. S. and J. L. Barron, 1995: The computation of optical flow. *ACM Computing Surveys*, **27**, 433-467.

Bellon, A. and I. Zawadzki, 1994: Forecasting of hourly accumulations of precipitation by optimal extrapolation of radar maps. *Journal of Hydrology*, **157**, 211-233.

Bringi, V. N. and V. Chandrasekar, 2001: *Polarimetric Doppler Weather Radar: Principles and Applications*. Cambridge University Press, 500 pp.

Brockwell, P. J. and R. A. Davis, 1991: State-Space Models and The Kalman Recursions. *Time Series: Theory and Methods*, New York: Springer-Verlag, 463-501.

Brockwell, P. J. and R. A. Davis, 1996: State-Space Models. *Introduction to Time Series and Forecasting*, New York: Springer-Verlag, 251-303.

Browning, K. A. and C. G. Collier, 1989: Nowcasting of precipitation systems. *Reviews of Geophysics*, **27**, 345-370.

Chandrasekar, V. and V. N. Bringi, 2004: Dual polarization radar estimates of rainfall: recent advances. *Sixth International Symposium on Hydrological Applications of Weather Radar, Melbourne, Australia*. 2-4 February, 2004.

Chornoboy, E. S., A. M. Marlin and J. P. Morgan, 1994: Automated storm tracking for terminal air traffic control. *Lincoln Laboratory Journal*, **7**, 427-448.

Cover, T. M. and J. A. Thomas, 1991: *Elements of Information Theory*. Wiley-Interscience, 542 pp.

Cristianini, N. and J. Shawe-Taylor, 2000: Kernel-Induced Feature Spaces. *An Introduction to Support Vector Machines and Other Kernel-based Learning Methods*, Cambridge University Press, 26-51.

Cucker, F. and S. Smale, 2001: On the mathematical foundations of learning. *Bulletin of Mathematical Society*, **39**, 1-49.

Dennery, P. and A. Krzywicki, 1996: Trigonometrical Series. *Mathematics for Physicists*, Dover Publications, 216-223.

Dixon, M. and G. Wiener, 1993: TITAN: thunderstorm identification, tracking, analysis, and nowcasting – a radar-based methodology. *Journal of Atmosphric and Oceanic Technology*, **10**, 785-797.

Duda, R. O., P. E. Hart and D. G. Stork, 2000: *k*-Means Clustering. *Pattern Classification*, 2nd Ed., John Wiley & Sons, Inc., 526-528.

Fabry, F., C. Frush, I. Zawadzki and A. Kilambi, 1997: On the extraction of near-surface index of refraction using radar phase measurements from ground targets. *Journal of Atmosphric and Oceanic Technology*, **14**, 978-987.

Frigo, M. and Steven G. Johnson, 2005: The Design and Implementation of FFTW3. *Proceedings of the IEEE* **93**, 216–231.

Germann, U. and I. Zawadzki, 2002: Scale-dependence of the predictability of precipitation from continental radar images. Part I: description of the methodology. *Monthly Weather Review*, **130**, 2859-2873.

Haykin, S., 1999: Neural Networks: A Comprehensive Foundation. Prentice Hall, 2nd Ed, 842 pp.

Higgins, J. R., 1996: Sampling Theory in Fourier and Signal Analysis: Foundations. Oxford University Press, 222 pp.

Holton, J. R., 2004: An Introduction to Dynamic Meteorology. Academic Press, 4th edition, 535 pp.

Horn, R. A. and C. R. Johnson, 1999: The Singular Value Decomposition. *Topics in Matrix Analysis*, Cambridge University Press, 144-153.

Jain, A. K, 1989: Fundamentals of Digital Image Processing. Prentice-Hall, 569 pp.

Johnson, J. T., P. L. Mackeen, A. Witt, E. D. Mitchell, G. J. Stumpf, M. D. Eilts and K. W. Thomas, 1998: The storm cell identification and tracking algorithm: an enhanced WSR-88D algorithm. *Weather and Forecasting*, **13**, 263-276.

Kalman, R. E., 1960: A new approach to linear filtering and prediction problems. *Transactions of the ASME – Journal of Basic Engineering (Series D)*, **82**, 35-45.

Keenan, T., P. Joe, J. Wilson, C. Collier, B. Golding, D. Burgess, P. May, C. Pierce, J. Bally, A. Crook, A. Seed, D. Sills, L. Berry, R. Potts, I. Bell, N. Fox, E. Ebert, M. Eilts, K. O'Loughlin, R. Webb, R. Carbone, K. Browning, R. Roberts, AND C.

Mueller, 2003: The Sydney 2000 world weather research programme forecast demonstration project: overview and current status. *Bulletin of the American Meteorology Society*, **84**, 1041-1054.

Kitzmiller, D. H., 1996: One-hour forecasts of radar-estimated rainfall by an extrapolative-statistical method. *TDL Office Notes 96-1*, National Weather Service, NOAA, U.S. Department of Commerce, 26 pp.

Kowalski, M. A., K. A. Sikorski, and F. Stenger, 1995: *Selected Topics in Approximation and Computation*. Oxford University Press, 368 pp.

Larsen, R., K. Conradsen, B. K. Ersboll, 1998: Estimation of dense image flow fields in fluids. *IEEE Transactions on Geoscience and Remote Sensing*, **36**, 256-264.

Leese, J. A., C. S. Novak and B. B. Clark, 1971: An automated technique for obtaining cloud motion from geosynchronous satellite data using cross correlation. *Journal of Applied Meteorology*, **10**, 118-132.

Li, L., W. Schmid and J. Joss, 1995: Nowcasting of motion and growth of precipitation with radar over a complex orography. *Journal of Applied Meteorology*, **34**, 1286-1300.

Ljung, L., 1998: Linear Regressions and the Least-Squares Method. *System Identification: Theory for the User*, Prentice-Hall, 2nd Ed, 203-211.

MacKeen, P. L., H. E. Brooks and K. L. Elmore, 1999: Radar reflectivity-derived thunderstorm parameters applied to storm longevity forecasting. *Weather and Forecasting*, **14**, 289-295.

Mielke, P. W., Jr. and K. J. Berry, 2001: Permutation Methods: A Distance Function Approach. Springer-Verlag N.Y., 352 pp.

Mueller, C., T. Saxen, R. Roberts, J. Wilson, T. Betancourt, S. Dettling, N. Oien, and J. Yee, 2003: NCAR Auto-Nowcast system. *Weather and Forecasting*, **18**, 545-561.

Oppenheim, A. V. and R. W. Schafer, 1989: *Discrete-Time Signal Processing*. Prentice-Hall, 879 pp.

Poggio T. and S. Smale, 2003: The mathematics of learning: dealing with data. *Notices of the American Mathematical Society*, **50**, 537-544.

Rauch, H. E., 1963: Solutions to the linear smoothing problem. *IEEE Transactions on Automatic Control*, **8**, 371-372.

Rinehart, R. E. and E. T. Garvey, 1978: Three-dimensional storm motion detection by conventional weather radar. *Nature*, **273**, 287-289.

Rood, R. B., 1987: Numerical advection algorithms and their role in atmospheric transport and chemistry models. *Reviews of Geophysics,* **25,** 71–100.

Schertzer, D. and S. Lovejoy, 1987: Physical modeling and analysis of rain and clouds by anisotropic scaling and multiplicative processes. *Journal of Geophysical Research,* **92,** 9693–9713.

Seed, A. W., 2003: A dynamic and spatial scaling approach to advection forecasting. *Journal of Applied Meteorology,* **42,** 381–388.

Shannon, C. E., 1949: Communication in the presence of noise. *Proc. Institute of Radio Engineers*, **37**, 10-21.

Sokol, Z., D. Rezacova and P. Pesice, 2004: Nowcasting of precipitation by using radar and NWP model data. *Proceedings of ERAD,* 444–449.

Stark, H. and J. W. Woods, 1994: Linear Estimation of Vector Parameters. *Probability, Random Processes, and Estimation Theory for Engineers*, Prentice-Hall, 288-292.

Stenger, F., 1993: Numerical Methods Based on Sinc and Analytic Functions. Springer-Verlag N.Y., 565 pp.

Stroud, J. R., P. Müller and B. Sansó, 2001: Dynamic models for spatiotemporal data. *Journal of the Royal Statistical Society: Series B (Statistical Methodology),* **63,** 673–689.

Theriault, K. E., M. M.Wolfson, B. E. Forman, R. G. Hallowell, M. P. Moore, and R. J. Johnson, Jr., 2000: FAA terminal convective weather forecast algorithm assessment. *9th Conference on Aviation, Range, and Aerospace Meteorology*, Orlando, FL, 365-370.

Tsonis, A. A. and G. L. Austin, 1981: An evaluation of extrapolation techniques for the short-term prediction of rain amounts. *Atmosphere-Ocean*, **19**, 54-65.

Vapnik, V. N., 1995: The nature of statistical learning theory. New York: Springer, 188 pp.

Wahl, D. D. and J. J. Simpson, 1990: Physical processes affecting the objective determination of near-surface velocity from satellite data. *Journal of Geophysical Research*, **95**, 13,511-13,528.

West, M. and J. Harrison, 1997: The Dynamic Linear Model. *Bayesian Forecasting and Dynamic Models*, New York: Springer, 97-137.

Whittaker, E. T., 1915: On the functions which are represented by the expansions of the interpolation theory. *Proc. Royal Soc. Edinburgh, Sec. A*, **35**, 181-194.

Wilson, J. W., 1966: Movement and predictability of radar echoes. *Tech. Memo. ERTM-NSSL-28*, National Severe Storms Laboratory, 30 pp.

Wilson, J. W., 2004: Precipitation nowcasting: past, present and future. *Sixth International Symposium on Hydrological Applications of Weather Radar*, Melbourne, Australia. 2-4 February, 2004.

Wilson, J. W., N. A. Crook, C. K. Mueller, J. Sun and M. Dixon, 1998: Nowcasting thunderstorms: a status report. *Bulletin of the American Meteorological Society*, **79**, 2079-2099.

Wilson, J. W. and C. K. Mueller, 1993: Nowcasts of thunderstorm initiation and evolution. *Weather and Forecasting*, **8**, 113-131.

Wolfson, M. M., B. E. Forman, R. G. Hallowell, and M. P. Moore, 1999: The growth and decay storm tracker. *8th Conference on Aviation*, Dallas, TX, Amer. Meteor. Soc., 58–62.

APPENDIX A. SUMMARY OF THE GROWTH AND DECAY STORM TRACKER (GDST) ALGORITHM

The Growth and Decay Storm Tracker (GDST) was developed by Wolfson et al (1999) at MIT Lincoln laboratory. The GDST is a radar storm motion and tracking based algorithm that has been successfully applied to the operational nowcasting (Theriaul et al 2000). It is a "state-of-the-art" tracking and nowcasting algorithm that is based on the enhanced cross-correlation method and has a minimum of meteorological interpretation. The major enhancement in the GDST algorithm is the employment of the elliptical-shaped filter in spatial domain to extract the large-scale envelope images of storms. It has been argued that the envelope images can better account for the large-scale and systematic growth and decay of storm systems (Wolfson et al 1999). The large-scale envelope images are used to track the storm motion fields based on the cross-correlation method (Rinehart and Garvey 1978). Subsequently the obtained motion fields are applied to extrapolating and nowcasting using original radar images.

Based on Wolfson et al (1999) and Theriaul et al (2000), the GDST based tracking algorithm has been implemented in current studies and procedures are summarized below.

Step 1: *The elliptical-shaped spatial filter is applied to the two-dimensional reflectivity images that are used for tracking.* The detailed description of the elliptical filter can be found in Wolfson et al (1999). The output of this step's processing is the envelope images of reflectivity that account for the systematic propagation of storm growth and decay.

Step 2: *The conventional cross-correlation method is applied to the filtered envelope images for estimating motion fields on pixel basis.* Several details for this procedure are obtained from Theriaul et al (2000), which are listed below.

- Pixel resolutions: 1 km × 1 km
- Correlation box size: 28 km × 28 km
- The maximum motion speed limit: 120 km/hr
- Minimum correlation for valid motion vector: 0.55
- Minimum fraction of non-zero pixels in correlation boxes: 10%
- Temporal weighting on motion vectors: 25% history-estimation + 75% current-estimation

The correlation box size is the local window size for cross-correlation matching. The maximum motion speed limit determines the maximal searching area. The minimum correlation value is the thresholding correlation for computing a valid motion vector such that any correlation values smaller than 0.55 are ignored. Any correlation boxes that have fraction of non-zero pixels less than 10% are ignored. To account for the impact of both history motion fields and currently estimated motion fields, a temporal weighting is applied on motion vectors over all pixels as shown above.

Step 3: *The advection extrapolation is computed using the latest estimation of motion field that is obtained in step 2.* The nowcasting reflectivity images are obtained by repeatedly applying the adevection extrapolation.

APPENDIX B. FORMULATION FOR THE EXTRAPOLATION OF RADAR REFLECTIVITY USING *SINC*-KERNEL

In chapter two the numerical algorithm for computing the extrapolation of radar reflectivity field has been developed. In this appendix the detailed derivation of Eq 2.5 is presented.

From Eq 2.3, the *SINC*-approximation to analytic functions, and Eq 2.4, discrete samples over the spatial domain, we can calculate temporal and spatial derivatives of *F(x, y, t)* as follows (with slight exchange of indices).

$$\begin{aligned}
\frac{\partial}{\partial t}F(x,y,t)\Big|_{\substack{x=k\cdot\Delta_x\\y=l\cdot\Delta_y}} &= \sum_{m=1}^{N_x}\sum_{n=1}^{N_y}\left[\frac{\partial}{\partial t}F_{mn}(t)\right]\times SINC(\frac{x}{\Delta_x}-m)\times SINC(\frac{y}{\Delta_y}-n)\Big|_{\substack{x=k\cdot\Delta_x\\y=l\cdot\Delta_y}} \\
&= \sum_{m=1}^{N_x}\sum_{n=1}^{N_y}\left[\frac{\partial}{\partial t}F_{mn}(t)\right]\times SINC(k-m)\times SINC(l-n) \\
&= \sum_{m=1}^{N_x}\sum_{n=1}^{N_y}\left[\frac{\partial}{\partial t}F_{mn}(t)\right]\times \delta_{mk}\times\delta_{nl} \\
&= \frac{\partial}{\partial t}F_{kl}(t)
\end{aligned} \tag{C.1}$$

$$\begin{aligned}
\frac{\partial}{\partial x}F(x,y,t)\Big|_{\substack{x=k\cdot\Delta_x\\y=l\cdot\Delta_y}} &= \sum_{m=1}^{N_x}\sum_{n=1}^{N_y}F_{mn}(t)\times\left[\frac{\partial}{\partial x}SINC(\frac{x}{\Delta_x}-m)\right]\times SINC(\frac{y}{\Delta_y}-n)\Big|_{\substack{x=k\cdot\Delta_x\\y=l\cdot\Delta_y}} \\
&= \sum_{m=1}^{N_x}\sum_{n=1}^{N_y}F_{mn}(t)\times\left[\frac{1}{\Delta_x}\cdot DSINC(k-m)\right]\times SINC(l-n) \\
&= \sum_{m=1}^{N_x}\left[\sum_{n=1}^{N_y}F_{mn}(t)\times\delta_{nl}\right]\times\left[\frac{1}{\Delta_x}\cdot DSINC(k-m)\right] \\
&= \frac{1}{\Delta_x}\sum_{m=1}^{N_x}DSINC(k-m)\cdot F_{ml}(t) \\
&= \frac{1}{\Delta_x}\left[\ \mathbf{A}\,\mathbf{F}(t)\ \right]_{kl}
\end{aligned} \tag{C.2}$$

$$\left.\frac{\partial}{\partial y}F(x,y,t)\right|_{\substack{x=k\cdot\Delta_x\\y=l\cdot\Delta_y}} = \sum_{m=1}^{N_x}\sum_{n=1}^{N_y} F_{mn}(t)\times SINC(\frac{x}{\Delta_x}-m)\times\left[\left.\frac{\partial}{\partial y}SINC(\frac{y}{\Delta_y}-n)\right|_{\substack{x=k\cdot\Delta_x\\y=l\cdot\Delta_y}}\right]$$

$$= \sum_{m=1}^{N_x}\sum_{n=1}^{N_y} F_{mn}(t)\times SINC(k-m)\times\left[\frac{1}{\Delta_y}\cdot DSINC(l-n)\right]$$

$$= \sum_{n=1}^{N_y}\left[\sum_{m=1}^{N_x} F_{mn}(t)\times\delta_{km}\right]\times\left[\frac{1}{\Delta_y}\cdot DSINC(l-n)\right] \qquad \text{(C.3)}$$

$$= \frac{1}{\Delta_y}\sum_{n=1}^{N_y} F_{kn}(t)\cdot DSINC(l-n)$$

$$= \frac{1}{\Delta_y}\left[\ \mathbf{F}(t)\ \mathbf{Z}\ \right]_{kl}$$

where the elements of matrices **A**, **Z** and **F**(t) are defined in Eqs 2.7, 2.8 and 2.9.

Inserting Eqs C.1, C.2 and C.3 into the following linear passive advection equation

$$\left\{\frac{\partial}{\partial t}F(x,y,t)\right\}\Bigg|_{\substack{x=k\cdot\Delta_x\\y=l\cdot\Delta_y}} = \left\{-U(x,y)\cdot\frac{\partial}{\partial x}F(x,y,t)-V(x,y)\cdot\frac{\partial}{\partial y}F(x,y,t)\right\}\Bigg|_{\substack{x=k\cdot\Delta_x\\y=l\cdot\Delta_y}}$$

$$= -U(x,y)\Big|_{\substack{x=k\cdot\Delta_x\\y=l\cdot\Delta_y}}\cdot\frac{\partial}{\partial x}F(x,y,t)\Big|_{\substack{x=k\cdot\Delta_x\\y=l\cdot\Delta_y}} \qquad \text{(C.4)}$$

$$-V(x,y)\Big|_{\substack{x=k\cdot\Delta_x\\y=l\cdot\Delta_y}}\cdot\frac{\partial}{\partial y}F(x,y,t)\Big|_{\substack{x=k\cdot\Delta_x\\y=l\cdot\Delta_y}}$$

It leads to Eq 2.5.

In above equations *DSINC*(x) is the derivative of *SINC*-function, which is given by

$$DSINC(x)\equiv\frac{d}{dx}SINC(x)=\begin{cases}\dfrac{1}{x}\left[\cos(\pi x)-SINC(x)\right] & x\neq 0\\ \\ 0 & x=0\end{cases} \qquad \text{(C.5)}$$

APPENDIX C. SUMMARY OF THE FUNDAMENTAL RESULTS OF THE LINEAR GAUSSIAN STATE SPACE MODEL

In this appendix some fundamental consequences are reviewed in the framework of linear Gaussian state-space models. These are standard results that can be found in literatures and textbooks, so the derivations will not be given here. The state-space models (SSM), Kalman recursions and the generalized SSM are discussed in Brockwell and Davis (1991 & 1996). Linear Gaussian state-space models and generalized Bayesian treatment are given in West and Harrison (1997). Detailed derivations and mathematical analysis can also be found in Kalman (1960) and Rauch (1963).

Nomenclature, notation and assumptions

$E(\cdot)$: The expectation operator.

$\vec{\mathbf{a}} \perp \vec{\mathbf{c}}$: $\vec{\mathbf{a}}$ and $\vec{\mathbf{c}}$ are orthogonal random vectors, if $E(\vec{\mathbf{a}}\vec{\mathbf{c}}^{\mathrm{T}}) = 0$.

$\vec{\mathbf{x}}_t$: Unobserved state vector at "t".

$\vec{\mathbf{y}}_t$: Observed data vector at "t".

$X^{(t)} \equiv \{\vec{\mathbf{x}}_1, \vec{\mathbf{x}}_2, \cdots, \vec{\mathbf{x}}_t\}$: The set of state vectors up to "t".

$Y^{(t)} \equiv \{\vec{\mathbf{y}}_1, \vec{\mathbf{y}}_2, \cdots, \vec{\mathbf{y}}_t\}$: The set of data vectors up to "t".

$P(\vec{\mathbf{z}}) \sim N(\vec{\mathbf{z}}; \vec{\boldsymbol{\mu}}, \boldsymbol{\Sigma})$: The random vector $\vec{\mathbf{z}}$ has a *multivariate normal density*, with mean $\vec{\boldsymbol{\mu}}$ and covariance matrix $\boldsymbol{\Sigma}$.

$P(\vec{\mathbf{y}}_t \mid \vec{\mathbf{x}}_t) \equiv P(\vec{\mathbf{y}}_t \mid \vec{\mathbf{x}}_t, X^{(t-1)}, Y^{(t-1)})$, $t = 1, 2, \cdots$: The observation equation of Markovian, conditional independence model in generalized SSM. For linear Gaussian SSM, $P(\vec{\mathbf{y}}_t \mid \vec{\mathbf{x}}_t) \sim N(\vec{\mathbf{y}}_t; \mathbf{G}_t\vec{\mathbf{x}}_t, \mathbf{R}_t)$.

$P(\vec{\mathbf{x}}_{t+1} \mid \vec{\mathbf{x}}_t) \equiv P(\vec{\mathbf{x}}_{t+1} \mid \vec{\mathbf{x}}_t,\ X^{(t-1)},\ Y^{(t)}),\ t = 1,\ 2,\ \cdots$: The state evolution equation of Markovian, conditional independence model in generalized SSM. For linear Gaussian SSM, $P(\vec{\mathbf{x}}_{t+1} \mid \vec{\mathbf{x}}_t) \sim N(\vec{\mathbf{x}}_{t+1};\ \mathbf{F}_t\vec{\mathbf{x}}_t,\ \mathbf{Q}_t)$.

$P(\vec{\mathbf{x}}_1 \mid Y^{(0)}) \equiv P(\vec{\mathbf{x}}_1)$: The initial state condition in the probability model.

In equations (3.26) and (3.27), we have (for all t)

$$E(\vec{\varepsilon}_t) = 0,\ E(\vec{\eta}_t) = 0; \tag{D.1}$$

$$E(\vec{\varepsilon}_t \vec{\varepsilon}_t^{\mathrm{T}}) = \mathbf{R}_t,\ E(\vec{\eta}_t \vec{\eta}_t^{\mathrm{T}}) = \mathbf{Q}_t,\ E(\vec{\eta}_t \vec{\varepsilon}_t^{\mathrm{T}}) = 0. \tag{D.2}$$

Problem definitions

Definition 3.2 The *Filtering* is defined by $P(\vec{\mathbf{x}}_t \mid Y^{(t)})$, which is the statistical inference about the state at time "t", $\vec{\mathbf{x}}_t$, given observations up to current time "t".

Definition 3.3 The *Smoothing* is defined by $P(\vec{\mathbf{x}}_{t-k} \mid Y^{(t)})$ $(k > 0)$, which is the statistical inference about the state at some previous time "t-k", $\vec{\mathbf{x}}_{t-k}$, given observations up to current time "t".

Definition 3.4 The *k-step Predicting* is defined by $P(\vec{\mathbf{x}}_{t+k} \mid Y^{(t)})$ $(k > 0)$, which is statistical inference about the state at time "t+k", $\vec{\mathbf{x}}_{t+k}$, given observations up to time "t".

Definition 3.5 The *k-step Forecasting* is defined by $P(\vec{\mathbf{y}}_{t+k} \mid Y^{(t)})$ $(k > 0)$, which is the statistical inference about the observation at time "t+k", $\vec{\mathbf{y}}_{t+k}$, given observations up to time "t".

The relation between $P(\vec{\mathbf{y}}_{t+k} \mid Y^{(t)})$ and $P(\vec{\mathbf{x}}_{t+k} \mid Y^{(t)})$ is given by

$$
\begin{aligned}
& P(\vec{\mathbf{y}}_{t+k}|Y^{(t)}) \\
&= \int d\vec{\mathbf{x}}_{t+k}\, P(\vec{\mathbf{y}}_{t+k},\ \vec{\mathbf{x}}_{t+k}|Y^{(t)}) \\
&= \int d\vec{\mathbf{x}}_{t+k}\, P(\vec{\mathbf{y}}_{t+k}\,|\,\vec{\mathbf{x}}_{t+k},\ Y^{(t)}) \cdot P(\vec{\mathbf{x}}_{t+k}|Y^{(t)}) \\
&= \int d\vec{\mathbf{x}}_{t+k}\, P(\vec{\mathbf{y}}_{t+k}\,|\,\vec{\mathbf{x}}_{t+k}) \cdot P(\vec{\mathbf{x}}_{t+k}|Y^{(t)})
\end{aligned}
\tag{D.3}
$$

In the last step of above derivations, we have applied the observation equation at time "$t+k$" and the conditional independence.

Solutions to Kalman filtering, predicting and k-step forecasting

The solutions to above statistical filtering, predicting and forecasting problems are summarized below (Brockwell and Davis 1991 & 1996; West and Harrison 1997).

1) Recursive Filtering & 1-step Predicting (Kalman 1960)

In linear Gaussian SSM described by equations (3.26) and (3.27), solutions to *filtering* and *1-step predicting* are given by Gaussian distributions

$$P(\vec{\mathbf{x}}_t \,|\, Y^{(t)}) \sim N(\vec{\mathbf{x}}_t;\ \vec{\mathbf{x}}_{t|t},\ \boldsymbol{\Omega}_{t|t}) \tag{D.4}$$

$$P(\vec{\mathbf{x}}_{t+1} \,|\, Y^{(t)}) \sim N(\vec{\mathbf{x}}_{t+1};\ \hat{\mathbf{x}}_{t+1},\ \boldsymbol{\Omega}_{t+1}) \tag{D.5}$$

The recursive solutions to quadruple $\{\hat{\mathbf{x}}_{t+1},\ \boldsymbol{\Omega}_{t+1};\ \vec{\mathbf{x}}_{t|t},\ \boldsymbol{\Omega}_{t|t}\}$ are given by

$$\hat{\mathbf{x}}_{t+1} = \mathbf{F}_t \vec{\mathbf{x}}_{t|t} \tag{D.6}$$

$$\boldsymbol{\Omega}_{t+1} = \mathbf{F}_t \boldsymbol{\Omega}_{t|t} \mathbf{F}_t^{\mathrm{T}} + \mathbf{Q}_t \tag{D.7}$$

$$\vec{\mathbf{x}}_{t|t} = \hat{\mathbf{x}}_t + \mathbf{K}_t(\vec{\mathbf{y}}_t - \mathbf{G}_t \hat{\mathbf{x}}_t) \tag{D.8}$$

$$\boldsymbol{\Omega}_{t|t}^{-1} = \mathbf{G}_t^{\mathrm{T}} \mathbf{R}_t^{-1} \mathbf{G}_t + \boldsymbol{\Omega}_t^{-1} \tag{D.9}$$

where *Kalman gain* is defined by $\mathbf{K}_t \equiv \boldsymbol{\Omega}_{t|t} \mathbf{G}_t^{\mathrm{T}} \mathbf{R}_t^{-1}$. Solutions are completed by the *initial filtering solution*

$$\boldsymbol{\Omega}_{1|1}^{-1} = \mathbf{G}_1^{\mathrm{T}}\mathbf{R}_1^{-1}\mathbf{G}_1 + \boldsymbol{\Omega}_1^{-1} \tag{D.10}$$

$$\begin{aligned}\vec{\mathbf{x}}_{1|1} &= E(\vec{\mathbf{x}}_1) + \mathbf{K}_1[\vec{\mathbf{y}}_1 - \mathbf{G}_1 E(\vec{\mathbf{x}}_1)] \\ &= E(\vec{\mathbf{x}}_1) + \boldsymbol{\Omega}_{1|1}\mathbf{G}_1^{\mathrm{T}}\mathbf{R}_1^{-1}[\vec{\mathbf{y}}_1 - \mathbf{G}_1 E(\vec{\mathbf{x}}_1)]\end{aligned} \tag{D.11}$$

The initial condition is given by

$$P(\vec{\mathbf{x}}_1) \sim N(\vec{\mathbf{x}}_1;\ E(\vec{\mathbf{x}}_1),\ \boldsymbol{\Omega}_1) \tag{D.12}$$

2) Recursive Smoothing (Rauch 1963)

In linear Gaussian SSM described by equations (3.26) and (3.27), given the initial condition (D.12), for all k: $1 \le k < t$, the *smoothing* marginal distribution is Gaussian

$$P(\vec{\mathbf{x}}_{t-k} \mid Y^{(t)}) \sim N(\vec{\mathbf{x}}_{t-k};\ \vec{\mathbf{m}}_t(k),\ \mathbf{C}_t(k)) \tag{D.13}$$

where $\vec{\mathbf{m}}_t(k)$ and $\mathbf{C}_t(k)$ are given by the following recursive relation

$$\vec{\mathbf{m}}_t(k) = \vec{\mathbf{x}}_{t-k|t-k} + \mathbf{B}_{t-k}[\vec{\mathbf{m}}_t(k-1) - \hat{\mathbf{x}}_{t-k+1}] \tag{D.14}$$

$$\mathbf{C}_t(k) = \boldsymbol{\Omega}_{t-k|t-k} + \mathbf{B}_{t-k}[\mathbf{C}_t(k-1) - \boldsymbol{\Omega}_{t-k+1}]\mathbf{B}_{t-k}^{\mathrm{T}} \tag{D.15}$$

where *gain* $\mathbf{B}_t$ is defined by

$$\mathbf{B}_t \equiv \boldsymbol{\Omega}_{t|t}\mathbf{F}_t^{\mathrm{T}}\boldsymbol{\Omega}_{t+1}^{-1} \tag{D.16}$$

Initial values $\{\vec{\mathbf{m}}_t(0),\ \mathbf{C}_t(0)\}$ are given by the solution to *filtering problem* at "*t*", $P(\vec{\mathbf{x}}_t \mid Y^{(t)}) \sim N(\vec{\mathbf{x}}_t;\ \vec{\mathbf{m}}_t(0),\ \mathbf{C}_t(0))$. $\{\vec{\mathbf{x}}_{t-k|t-k},\ \boldsymbol{\Omega}_{t-k|t-k}\}$ is the solution to *filtering problem* at "*t-k*". $\{\hat{\mathbf{x}}_{t-k+1},\ \boldsymbol{\Omega}_{t-k+1}\}$ is the solution to *1-step predicting problem* at "*t-k*", $P(\vec{\mathbf{x}}_{t-k+1} \mid Y^{(t-k)}) \sim N(\vec{\mathbf{x}}_{t-k+1};\ \hat{\mathbf{x}}_{t-k+1},\ \boldsymbol{\Omega}_{t-k+1})$.

3) k-step Predicting & Forecasting

In linear Gaussian SSM described by equations (3.26) and (3.27), given the initial condition (D.12), solutions to *k-step Predicting* and *k-step Forecasting* are both Gaussian distributions ($k > 0$)

$$P(\vec{\mathbf{x}}_{t+k} \mid Y^{(t)}) \sim N(\vec{\mathbf{x}}_{t+k};\ \vec{\mathbf{m}}_k,\ \mathbf{C}_k) \tag{D.17}$$

$$P(\vec{\mathbf{y}}_{t+k} \mid Y^{(t)}) \sim N(\vec{\mathbf{y}}_{t+k};\ \vec{\boldsymbol{\mu}}_k,\ \boldsymbol{\Sigma}_k) \tag{D.18}$$

$\vec{\mathbf{m}}_k$ and $\mathbf{C}_k$ are solved by the following recursion

$$\vec{\mathbf{m}}_k = \mathbf{F}_{t+(k-1)}\vec{\mathbf{m}}_{k-1} \tag{D.19}$$

$$\mathbf{C}_k = \mathbf{F}_{t+(k-1)}\mathbf{C}_{k-1}\mathbf{F}_{t+(k-1)}^{\mathrm{T}} + \mathbf{Q}_{t+(k-1)} \tag{D.20}$$

The initial values $\{\vec{\mathbf{m}}_0,\ \mathbf{C}_0\}$ are given by the solution to *filtering* at time "t",

$P(\vec{\mathbf{x}}_t \mid Y^{(t)}) \sim N(\vec{\mathbf{x}}_t;\ \vec{\mathbf{m}}_0,\ \mathbf{C}_0)$.

$\vec{\boldsymbol{\mu}}_k$ and $\boldsymbol{\Sigma}_k$ are solved by

$$\vec{\boldsymbol{\mu}}_k = \mathbf{G}_{t+k}\vec{\mathbf{m}}_k \tag{D.21}$$

$$\boldsymbol{\Sigma}_k = \mathbf{G}_{t+k}\mathbf{C}_k\mathbf{G}_{t+k}^{\mathrm{T}} + \mathbf{R}_{t+k} \tag{D.22}$$

4) Equivalent expressions for Kalman gain

$\mathbf{K}_t$ has following equivalent expressions

$$\mathbf{K}_t = \boldsymbol{\Omega}_{t|t}\mathbf{G}_t^{\mathrm{T}}\mathbf{R}_t^{-1} \tag{D.23}$$

$$\mathbf{K}_t = \boldsymbol{\Omega}_t\mathbf{G}_t^{\mathrm{T}}[\mathbf{R}_t + \mathbf{G}_t\boldsymbol{\Omega}_t\mathbf{G}_t^{\mathrm{T}}]^{-1} \tag{D.24}$$

5) Equivalent expressions for $\boldsymbol{\Omega}_{t|t}$

$\boldsymbol{\Omega}_{t|t}$ has following equivalent expressions

$$\boldsymbol{\Omega}_{t|t}^{-1} = \boldsymbol{\Omega}_t^{-1} + \mathbf{G}_t^{\mathrm{T}}\mathbf{R}_t^{-1}\mathbf{G}_t \tag{D.25}$$

$$\Omega_{t|t} = \Omega_t - \Omega_t G_t^T [R_t + G_t \Omega_t G_t^T]^{-1} G_t \Omega_t \tag{D.26}$$

$$\Omega_{t|t} = \Omega_t - K_t [R_t + G_t \Omega_t G_t^T] K_t^T \tag{D.27}$$

$$\Omega_{t|t} = [\hat{I} - K_t G_t] \Omega_t \tag{D.28}$$

The above formulas can be used for recursive filtering, predicting and forecasting. Different formulas for K_t and $\Omega_{t|t}$ are summarized above. Mathematically these formulas are equivalent to their peers. However, in the numerical implementation certain form may be more efficient than others.